The Use of Liquid Phase Transmission Electron Microscopy for Quantifying Interactions Between Colloidal Nanoparticles and Visualizing Their Self-Assembled Structures

By

Hoduk Cho

A dissertation submitted in partial satisfaction of the

requirements for the degree of

Doctor of Philosophy

in

Chemistry

in the

Graduate Division

of the

University of California, Berkeley

Committee in charge:

Professor A. Paul Alivisatos, Chair
Professor Peidong Yang
Professor Eva Nogales

Spring 2018

The Use of Liquid Phase Transmission Electron Microscopy for Quantifying Interactions Between Colloidal Nanoparticles and Visualizing Their Self-Assembled Structures

By

Hoduk Cho

Abstract

The Use of Liquid Phase Transmission Electron Microscopy for Quantifying Interactions Between Colloidal Nanoparticles and Visualizing Their Self-Assembled Structures

By

Hoduk Cho

Doctor of Philosophy in Chemistry

University of California, Berkeley

Professor A. Paul Alivisatos, Chair

This dissertation demonstrates the application of liquid phase transmission electron microscopy for quantifying interactions between colloidal nanoparticles and visualizing their self-assembled structures in their native solution state. Over a decade ago, the first liquid cells that could successfully enclose a thin layer of liquid while maintaining compatibility with the high vacuum conditions inside an electron microscope were developed. Subsequent commercialization of this technology by several companies greatly increased its accessibility and the research field has expanded rapidly as a result. The ability to directly visualize real-time nanoscale dynamics in solution has enabled researchers in physics, chemistry, biology, and materials science to investigate previously unexplored scientific phenomena. Thus far, the vast majority of research in this field has made use of the highly perturbative effect of the electron beam to initiate the dynamic process under study. Although this approach has yielded fruitful knowledge and insights, it has not been straightforward to extrapolate the conclusions formed from these studies to experiments conducted outside of the electron microscope. The effects of electron beam irradiation are still poorly understood, and ways to counteract them are limited. A more widespread application of liquid phase transmission electron microscopy would only be realized if the influence of the electron beam were well-known and could be tuned in a predictable manner. By understanding and controlling the effects of the electron beam on the encapsulated specimen during the imaging process, it will be possible to extract information relating to the behavior of colloidal nanoparticles in solution that can be generalizable to experiments carried out in the wet lab.

Chapter 1 introduces the basic concepts of nanoparticle self-assembly, interparticle interactions at the nanoscale, DNA-mediated nanoparticle assembly, liquid phase transmission electron microscopy, and radiation-induced effects that accompany electron microscopy imaging in liquid. Chapter 2 illustrates how the individual trajectories of nanoparticles moving in solution, obtained using liquid phase transmission electron microscopy, can be utilized for quantitative analysis of their interparticle interactions. Chapter 3 describes how the damaging effects of electron beam irradiation on DNA-assembled nanoparticles can be mitigated with the use of graphene and its derivatives as biocompatible radical scavengers. Chapter 4 summarizes the seminal findings that are reported in this dissertation and provides a brief outlook for the future.

Dedicated to my parents and brother, for their love and support.

Acknowledgements

First and foremost, I must thank my advisor Paul Alivisatos for his insight and guidance throughout my graduate student career as well as for creating the optimal research environment for an ambitious scientist to thrive in. He gave me complete freedom to go after a project that sparked my interest and I never had to worry about the possibility of not being able to produce tangible short-term results or the cost of my experiments. His emphasis on how important it is for a young graduate student to be self-motivated and daring encouraged me to formulate scientific questions that would set me on my own exciting journey for unexplored knowledge. Under his stewardship, I was able to mature into an independent scientist with experience and confidence.

I would like to thank all of my mentors and collaborators who enabled me to push my research beyond my own finite set of capabilities. In particular, I would like to express my gratitude to my mentors Qian Chen and Matthew Jones who helped me realize that research can be so intellectually stimulating (and sometimes gratifying too). They were both immensely influential in shaping what kind of a scientist I would become and with their help, I was able to transition from being a consumer to a producer of scientific knowledge. I also thank Karthish Manthiram, Xingchen Ye, Son Nguyen, and Yang Xia for their generosity in sharing their expertise and ideas. Without their help, my research projects would have been much more challenging to implement.

I would like to thank our group's administrative manager Negest Williams, who has been critical in ensuring that the researchers in our group only had to concern themselves with scientific problems. I would also like to thank Jacob Olshansky and Justin Ondry for having been wonderful fellow co-supervisors of our group's transmission electron microscope which was so instrumental to my research. I am grateful to many of the past, current, and honorary members of the Alivisatos Group for creating such a welcoming atmosphere and in particular, I would like to thank David Litt, Erin O'Brien, Matthew Koc, and Tamara Sparks for their friendship and all the memories of authentic American experiences that I will cherish for the rest of my life.

There are a number of Korean friends that I would like to recognize for enriching my life at Berkeley. My fellow chemistry graduate students, Keunhong Jeong, Sumin Lee, Taegyo Lee, Seungkyu Lee, Suhong Kim, and Ilhyung Lee helped me handle the stress that inevitably accompanies failed experiments. My tennis partners, Taehyung Cho and Kunwoo Lee, enabled me to take my mind off from work during the sunny weekends. I also greatly enjoyed participating in Korean Graduate Student Association Tennis Club sessions on Friday evenings. I would also like to thank all other Korean graduate students and postdocs who I had the pleasure of making acquaintance with.

I would like to take this opportunity to thank all those who have contributed to my intellectual development before I started my PhD. James Durrant, my undergraduate research advisor at Imperial College London, allowed me to join his research group and introduced me to the art of identifying and tackling scientific problems. Benjamin Chen, my chemistry classmate at Imperial, was a source of inspiration throughout my undergraduate years. Before I attended university, John Cullerne and Chas McCaw, who were my physics and chemistry teachers respectively, successfully persuaded me to contemplate a career in science. Their idealistic depiction of research as being a streamlined process of imaginative and strategic planning that yields intended results,

with little emphasis on grueling optimization and the possibility of having to compromise when unforeseen challenges arise, was more than enough to mesmerize a naïve and intellectually curious teenager. Tomáš Zeman, Colin Hui, and Peter Harrison, my academically gifted schoolmates at secondary school, left a strong impression on my younger self and I derived a considerable amount of motivation from them.

Last but certainly not the least, I thank my family members for all of their unquestionable love and support. My parents always made my well-being their highest priority and not only did they grant me complete freedom to choose my own career path, but they also went further by actively helping me pursue my dreams. They were eager to provide me with education of the highest quality, allowing me to be instructed at the most prestigious boarding schools in the United Kingdom from elementary school onward. If only I had been born with even half the intellect of my father, Dr. Cho, then my graduate student career would have been so much more productive and impactful. My mother has always respected my decisions and I never had to look elsewhere for emotional support. My older brother has been a great friend who I often looked toward for life advice and I have often been thankful that I had an older sibling to rely on. I consider myself undeservedly fortunate to have such loving family members and I am indebted to them forever. My doctoral dissertation is dedicated to them.

This work was supported by the Defense Threat Reduction Agency under Award HDTRA1-13-1-0035, by a grant from King Abdulaziz City for Science and Technology, Kingdom of Saudi Arabia, and by the Nanomachines Program, KC1203, Office of Basic Energy Sciences of the United States Department of Energy under Contract Number DE-AC02-05CH11231.

Table of Contents

List of Figures

Chapter 1

Introduction

1.1 Nanoparticle self-assembly

Self-assembly is a parallel bottom-up process where building blocks order themselves into the final structure. The ability to rationally design the self-assembly of nanoscale building blocks to create complex nanostructures is crucial for realizing the full potential of colloidal nanoparticles in future technological applications. Nanoparticles hold great promise for their electronic, optical, catalytic, and mechanical properties, which are easily tunable through colloidal synthesis. In addition, the use of nanoparticles as building blocks opens up an enormous number of possible permutations because of the extensive library of available chemical compositions and shapes of nanoparticles that can be obtained with excellent size uniformity and shape purity. If we had absolute control over the position of each nanoparticle building block, we would be able to tailor the emergent functional properties of the final structure for a particular application. Beyond technological implications, self-assembly is a fascinating phenomenon in its own right since the evolution of order from a disordered initial state is a common theme in living systems, with examples including cells, DNA, proteins, and lipid vesicles.[1,2]

The balance of thermodynamics and kinetics must be carefully optimized for self-assembly to succeed.[3] Designing the final structure to be the thermodynamically favored state is not sufficient as the presence of kinetic traps will slow down the process to the extent that the desired state will not be accessible at the experimental timescale. Kinetic trapping gives rise to metastable structures when the attractive interactions are too strong, meaning that attachments are no longer reversible. As a consequence, the structural relaxation of defects in such structures, resulting from random collisions of particles moving under the influence of thermal fluctuations, is inhibited. At the other end of the spectrum, when the attractive interactions are too weak, the entropic effects of random mixing starts to compete and the target structure is not obtained.[4] Additionally, assembly of multicomponent systems requires the interactions to be specific so that the desired configuration will outcompete all the other possible configurations. The balance of specific and nonspecific interactions is also required since when the interactions are too specific, then the assembly would take too long as there are too many configurations that must be sampled.[5] Unfortunately, the presence of nonspecific interactions means that defects are also more likely to form. For successful self-assembly, the attractive interactions must be strong enough to provide the driving force for assembly into the desired configuration but be weak enough to allow reversible sampling of all the different local configurations before the thermodynamically favored state is reached. Long-range correlation between the relevant components could expedite the kinetics of self-assembly.[6]

The ultimate goal of self-assembly is to make structures of arbitrary complexity where the position of each component has been predetermined. To construct such structures from nanoparticles through self-assembly, the nanoparticles themselves must be encoded with the information that dictates how they will selectively interact with each other.[6] This could be accomplished through several ways, such as particle shape, size,

composition, and surface functionality. The use of anisotropic or patchy particles allow interactions with directionality. Anisotropic particles introduce directionality when interactions between two neighboring particles scale with their contact area. Patchy particles, which possess heterogeneous surface functionalities, allow interactions to be confined to certain orientations of the particle. But most importantly, we need the ability to tune the interparticle interactions. To be able to achieve a high level of control at the nanoscale, we need a better understanding of the forces that determine how individual colloidal nanoparticles interact with each other in solution.

1.2 The nature of interactions between colloidal nanoparticles

The types of interparticle interactions that will be discussed in detail here will be van der Waals, electrostatic, steric, and depletion interactions which commonly appear in colloidal systems. Van der Waals interaction, ubiquitous in all systems, includes permanent dipole-permanent dipole (Keesom force), permanent dipole-induced dipole (Debye force), and induced dipole-induced dipole interactions (dispersion force).[7,8] Its net interaction is attractive for identical materials but may be repulsive for dissimilar materials.[9] For nanoparticles, the maximum range of this interaction is typically around 10 nm.[7] Electrostatic (Coulombic) interaction is the interaction between charged species and for colloidal particles, surface charge is introduced by coating them with ligands that ionize in solution. In the presence of electrolytes, there is a screening effect which is often approximated using a model where the charged species are uncorrelated point charges and the surrounding environment is a homogeneous dielectric medium.[10] The range of screened electrostatic interaction is determined by the choice of solvent and the ionic strength, while the proportion of surface capping ligands that ionize may be highly pH sensitive. When solvated, charged particles are surrounded by electrical double layers, consisting of counterions, and repulsion results when these double layers overlap. Steric interaction originates from Pauli repulsion, which occurs when electronic wavefunctions are being confined to the same space, and thus is a short-range repulsion that sharply rises at very small separations.[8] Models that are derived from first principles to describe this interaction do not yet exist and so it is usually approximated by empirical functions, including step, linear, inverse power law, and exponential functions.[8,9] Steric interaction has been widely used to impart colloidal stability to particles by densely coating their surfaces with polymer chains that prevent aggregation. Depletion interaction is an attractive interaction that arises from entropic effects.[7] This is observed when particles of interest are in the presence of much smaller particles, where the latter are referred to as depletants. When the larger particles attach, this liberates more space for the depletants and the net entropy of the system increases. The magnitude and range can be tuned independently by varying the depletant concentration and size, respectively.[7,11] Other interactions that may be present in colloidal nanoparticle systems include hydrogen bonding, magnetic, hydrophilic, and hydrophobic interactions. Since all interparticle interactions are electromagnetic in essence, these classifications are done mostly for convenience and so the definitions that differentiate between them may not be clear cut.[11]

For describing the interactions between microparticles, the Derjaguin–Landau–Verwey–Overbeek (DLVO) theory has enjoyed considerable success.[7,12] In its original form, the overall interaction was given by the superposition of short-range van der Waals

attraction and long-range screened electrostatic repulsion. It has been used to quantitatively explain the colloidal stability of charged particles in different environments. Although modifications to the original model have been made to include other interparticle interactions with the purpose of making it more accurate and widely applicable,[12] the key feature has remained in that it simply expresses the overall interaction as the linear sum of different interactions that are present, which are assumed to be decoupled. Although the DLVO theory has often been invoked to describe colloidal nanoparticle interactions, the validity of this approach has increasingly been called into question as experimental findings that provide counter examples to the theory continue to accumulate.[12]

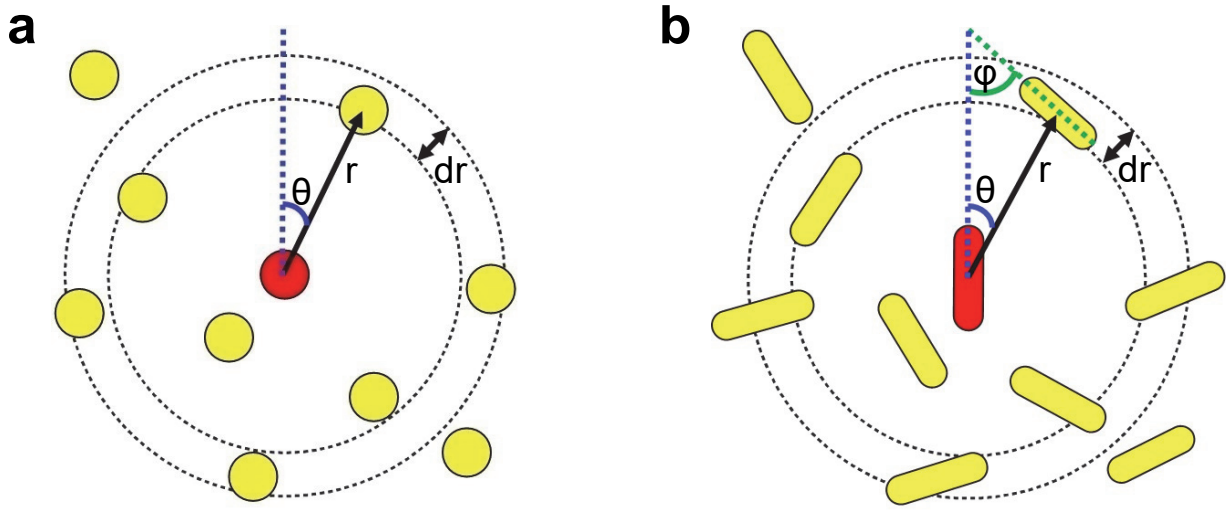

Figure 1.1 Illustration of the radial distribution function analysis. (a) Spherical particles confined in 2D. (b) Rod shaped particles confined in 2D.

One experimental method of extracting quantitative information relating to interparticle interactions involves analysis using the radial distribution function (or pair correlation function), g(r):

$$g(r) = \frac{\rho(r)}{\rho_{avg}} \tag{1}$$

where ρ(r) is the areal density of particles within the circular ring confined by r and r + δr and ρ_{avg} is the average areal density of particles as illustrated in Figure 1.1a for spherical particles confined in 2D. For simple spherical particles, the isotropic shape of individual particles means that there is no orientational dependence, so g(r) does not depend on θ although θ is necessary to locate the particle position. The effective pairwise interaction potential between the particles, u(r), can then be obtained through the following relation:

$$g(r) = \mathrm{e}^{-\frac{u(r)}{k_B T}} \tag{2}$$

where k_B is the Boltzmann constant and T is the temperature. For spherical microparticles, which are typically made from poly(methyl methacrylate) (PMMA), polystyrene (PS), or

silica with surface functionalization, this technique has been widely used due to the ease of tracking particles in solution using optical microscopy. Direct visualization of microparticle dynamics in real time, using optical microscopy combined with charge-coupled device (CCD) cameras, has allowed researchers to probe their interactions in solution.[13–15] In addition, optical tweezers have been recently employed to predefine the initial spatial configuration of colloidal microparticles and equipped with these capabilities, steric interaction and screened electrostatic repulsion have been experimentally measured and compared with existing models and simulation studies.[15–17]

For anisotropic particles, the analysis becomes more involved. As shown in Figure 1.1b, there are now two orientational parameters, θ and φ, which are necessary to define the relative rod configurations for a system of rods confined in 2D. Since the radial symmetry is no longer present, it is not possible to neglect the orientational dependence and so g(r) must be replaced with g(r,θ,φ). Likewise, u(r) also takes on angular dependence. Considering that rods are the simplest anisotropic particles, it can be easily perceived that the analysis quickly becomes more challenging as particles become less symmetric. Because of the increased complexity of the analysis and the restricted range of accessible microparticle shapes, investigations into the effect of particle anisotropy on interparticle interactions have been limited.[18,19]

Our current understanding of how nanoparticles interact with each other is far from complete. Although the types of interactions that are present in a system of nanoparticles are the same as that for microparticles, the length scale at which the effects of these interactions are being considered has shifted. Theoretical models that can describe interactions of microparticles fail at the nanoscale as the underlying assumptions and approximations become invalid. Continuum approximations break down when solvated ions, solvent molecules, and colloidal particles are comparable in size, so treating ions and solvent molecules as a homogeneous background is not justifiable. For an accurate modeling of nanoscale interactions, the structural discreteness of all the species present and their instantaneous fluctuations must be explicitly accounted for. This implies that when the interparticle separation is reduced to several nanometers, the nonadditivity of the different interactions manifests itself.[7,10,12] The overall interactions can no longer be assumed to be the linear sum of separate interactions due to the coupling effects resulting from each interaction influencing the nearby species.

Despite the inherent inaccuracy associated with the use of classical colloidal models, which had been developed to interpret interactions of microparticles, to describe nanoparticle interactions, there is yet no better alternative. This gap in our knowledge is mainly due to the difficulty of experimentally obtaining quantitative information concerning how nanoparticles interact with each other. The lack of experimental data also makes it challenging for computational chemists to simulate such systems as accurate models to describe their effective interactions are not available.[20] If a method could be developed to map out the trajectories of nanoparticles that are interacting with each other in real time, it would be possible to apply the same analysis that has already been done for microparticles using optical microscopy. This will allow quantitative analysis of nanoparticle interactions, thus fostering a synergistic outcome where experimental results and computer simulations can complement each other to attain the ultimate goal of being able to predict the behavior of a given system of nanoparticles.

1.3 DNA-mediated self-assembly of nanoparticles

Of all the nanoparticle self-assembly techniques developed thus far, the DNA-mediated approach is perhaps the most advanced. Although DNA has been studied mostly for its biological functions, especially for its role as the carrier of genetic information, the ability of oligonucleotides to self-assemble into a higher order structure as dictated by their sequence has been exploited by researchers to create complex nanostructures.[21] The programmability of DNA binding, made possible through the highly predictable nature of selective Watson-Crick base-pairing interactions where adenine binds with thymine and guanine binds with cytosine, enables self-assembly of structures with designed spatial configurations. Through permutation of oligonucleotide sequences, we can define how DNA hybridization will take place in 3D with subnanometer resolution (at a single base level). Control over assembly of matter with such a high level of precision has not been emulated yet by other synthetic methods, hence the reason why researchers continue to take advantage of nature's building blocks. Oligonucleotides with a desired sequence can be made synthetically using automated DNA synthesizers or purchased from companies such as Integrated DNA Technologies. This has allowed researchers to extensively explore the potential of DNA as nanoscale building blocks. Although several distinct strategies exist for DNA-based self-assembly, such as DNA tiles,[22] DNA origami,[23] DNA bricks,[24] DNA-Au nanoconjugates,[25] we focus on the approach pioneered by Mirkin *et al* where inorganic nanoparticles act as rigid templates for directional DNA binding.[26]

DNA-NP superlattices are DNA hybridization-mediated assemblies of DNA functionalized nanoparticles (DNA-NPs) that adopt a crystalline arrangement defined by the programmable DNA base-pairing interactions.[27,28] DNA-NPs are nanoparticles that have been densely functionalized at the surface with oligonucleotides that adopt conformations dictated by the local geometric shape of the firm nanoparticle core. These DNA-NPs then act as building blocks which can be assembled together through DNA hybridization. By designing the DNA sequences of the sticky ends, which are short single-stranded regions at the termini of the oligonucleotides that undergo hybridization, and choosing the appropriate overall hydrodynamic size and shape of the DNA-NPs, these can be assembled into predetermined crystal structures with varying complexity.[27,29,30] The fundamental guiding principle underlying how DNA-NPs organize is that the final structure maximizes the total DNA hybridization interaction. Using spherical DNA-NPs as building blocks, an exhaustive library of crystal structures, ranging from standard body-centered cubic (BCC) and face-centered cubic (FCC) structures to exotic ternary crystals and crystal structures with no atomic analogues, have been conceived and experimentally obtained.[29,31] Although Au nanoparticles have been the material of choice in most of these studies, due to the ease of functionalizing gold surfaces with DNA, other materials including CdSe/Zn core-shell quantum dots, Fe_3O_4 nanoparticles, and Pt nanoparticles have also been used and it may be possible in the future to expand the set of materials to organic and bioorganic nanoparticles.[32]

The use of anisotropic DNA-NP building blocks has allowed a rich variety of new structures to be devised. Rods, triangular prisms, circular disks, cubes, octahedra, and rhombic dodecahedra have all been exploited for construction of novel structures.[33–35] Anisotropic DNA-NPs have made previously inaccessible structures obtainable because they imbue the building blocks with directionality. Since the attached oligonucleotides are

aligned perpendicular to the nanoparticle surface, the DNA interactions are isotropic for spherical DNA-NPs. However, when the nanoparticle itself possesses geometric anisotropy, then the oligonucleotide layer adopts the anisotropic shape of the nanoparticle. Because the final assembled structure is the one that maximizes the DNA hybridization interaction, the anisotropic shape of the oligonucleotide layer means that even for single-component systems, certain orientations that maximize the contact area between DNA-NPs are favored. For rods, side-to-side assembly is favored and so 2D hexagonal sheets are formed.[33] For triangular prisms, face-to-face stacking occurs and so 1D columnar structures are seen.[33] For cubes, face-to-face configurations are again favored and they assemble into a simple cubic structure.[34] Moreover, the availability of different building block shapes has allowed co-crystal structures to be generated from their binary combinations as they undergo assembly with directional specificity that can be predicted based on their shape complementarity. Alternate face-to-face stacking of prisms and circular disks, simple cubic packing of cubes with interpenetrating circular disks, and BCC packed octahedra with interpenetrating circular disks have all been observed.[35,36]

Using DNA-NPs as atomic analogues, DNA-NP superlattices can act as a model system for studying thermal annealing of defects as well as crystal nucleation and growth. Compared with atoms, colloidal nanoparticles are larger in size and so exhibit slower dynamics, making experimental observation easier. When DNA-NP superlattices are assembled at room temperature, amorphous structures form initially, due to kinetic trapping, but long-range crystallinity evolves after thermal annealing.[37] When the temperature is raised close to the DNA melting point, DNA-NPs become mobile enough that they can undergo rearrangement to reach a configuration that is thermodynamically favored. This annealing process is analogous to that for atomic crystals, where structural defects can be annealed out to give single-crystalline domains. Recently, there has been a shift in focus from creating new static crystal structures to exploiting the tunable nature of DNA linkages that will lead to functional stimuli-responsive systems where structural reconfigurability is achieved using DNA strand replacement.[38,39] If DNA-NP superlattices could be imaged directly in their native hydrated state with single particle resolution in real time, it would open up many possibilities for studying the dynamics of such processes.

1.4 Liquid phase transmission electron microscopy

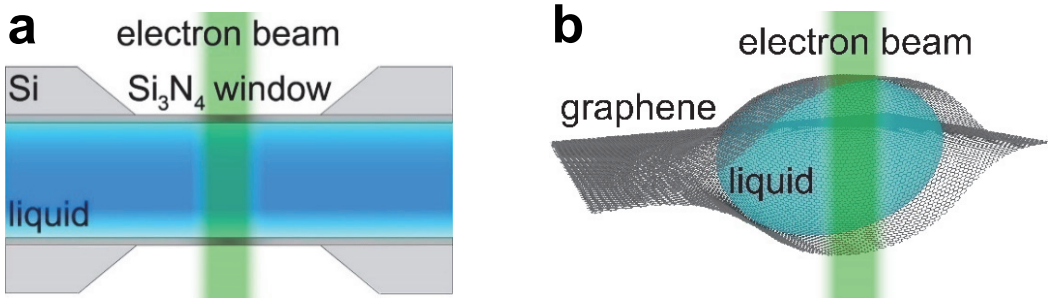

Figure 1.2 Schematic of different liquid cell configurations. (a) Silicon nitride liquid cell. (b) Graphene liquid cell.

Electron microscopy has been indispensable to the nanoscience community since the development of the first electron microscope by Ruska in 1932.[40] It has been critical

for the rapid growth in the field of nanoscience, allowing material characterization at the length scale that is far beyond the capability of optical microscopy. As described by the de Broglie relation, electrons that have been accelerated at high voltage possess a much smaller wavelength than visible light. Hence, by using these high energy electrons for image formation, the limit on the spatial resolution is no longer determined by the diffraction limit for visible light (around 200 nm). Image formation using transmission electron microscopy (TEM) relies on passing a beam of electrons, which are guided by electromagnetic lenses, through a thin specimen (typically a few hundreds of nanometers at most) and detecting the transmitted electrons. Electron scattering depends on factors such as the atomic number of nuclei and the specimen thickness, and variations in the extent of electron scattering across the specimen give rise to contrast in the final image. The recorded digital image is a 2D projection of the actual 3D structure and in bright field mode, areas containing atoms with high atomic numbers appear dark. Because electrons are easily deflected by molecules, electron microscopes require high vacuum to operate. Thus for conventional TEM, only solid specimens could be imaged. Atomic resolution TEM imaging of nanomaterials is now routinely accessible and the aberration-corrected electron microscopes that are available today offer spatial resolutions of 50 pm or better.

Liquid phase TEM is a technique that allows direct real-time imaging of dynamic nanoscale processes occurring in solution. Recent advances in microfabrication led to the development of the first liquid cells by Ross *et al* that made use of very thin but robust silicon nitride membranes as electron transparent imaging windows (Figure 1.2a).[41] In these silicon nitride liquid cells, a submicrometer layer of liquid is encapsulated between a pair of microchips to ensure compatibility with the high vacuum conditions inside the electron microscope. This technique has subsequently been commercialized by several companies (including Protochips and Hummingbird Scientific), greatly increasing its accessibility to researchers who don't possess the microfabrication expertise required for making custom-built liquid cells. The current state of the art silicon nitride liquid cell technology makes use of dedicated TEM holders with functionalities for liquid flow as well as *in situ* heating and electrical biasing.[42] Liquid flow enables a new chemical species to be introduced into the liquid cell to initiate the process being investigated. Similarly, capabilities for controlled heating (with the maximum temperature currently limited to 100 °C) and electrical biasing, made possible by having electrodes embedded on the microchips, allow these stimuli to influence the system under study in the desired way. The abilities to flow in chemicals and apply heat would allow a wide variety of chemical processes to be visualized, such as colloidal synthesis of nanocrystals, while control over electrical bias would be most useful for battery-related research. A recent study has also demonstrated the concept of laser-coupled liquid phase TEM, where the specimen is excited by a laser and the resulting dynamics can be monitored at ultrafast timescales.[43] We anticipate that more correlative studies that combine liquid phase TEM with spectroscopic techniques such as electron energy loss spectroscopy, energy dispersive X-ray spectroscopy, fluorescence spectroscopy, and Raman spectroscopy, will follow in the near future to exploit its unique advantages. Because the electron beam has to pass through silicon nitride windows (with a typical thickness of 50 nm each) and the encapsulated liquid layer, which can be hundreds of nanometers in thickness, the image quality is often much worse than what is normally possible using conventional TEM of dry samples suspended on an ultrathin membrane. Future improvements in the fabrication of

thinner windows and methods to minimize their bulging, which arises due to the pressure differential between the liquid cell and the column inside an electron microscope, will be necessary for conducting studies that require better contrast and spatial resolution. Window bulging is a significant problem since this leads to the thickness of the liquid layer being much greater near the middle of the windows. This has meant that sample imaging has been limited to the regions near the window edges, where the bulging is minimal, thus greatly restricting the area that can be studied for a given liquid cell sample.

Graphene liquid cells present an alternative to silicon nitride liquid cells where liquid encapsulation is carried out using impermeable graphene sheets (Figure 1.2b).[44] They provide superior spatial resolution and contrast due to minimal electron scattering by the atomically thin graphene windows and the small size of the liquid pockets that can form, which can be only a few nanometers in height.[44] Nevertheless, there are significant inherent drawbacks to graphene liquid cells. The liquid pockets are not stable against prolonged exposure to the electron beam and they have been observed to dry out during extended imaging. Moreover, due to the hermetic configuration of the liquid pockets and the uncontrolled nature of their formation, technical advances in microfluidics for silicon nitride liquid cells have not been easily transferable. The success rate of liquid encapsulation has also been found to depend heavily on the solvent parameters, such as salt concentration for aqueous systems. These factors have inhibited the widespread use of graphene liquid cells despite their ease of fabrication.

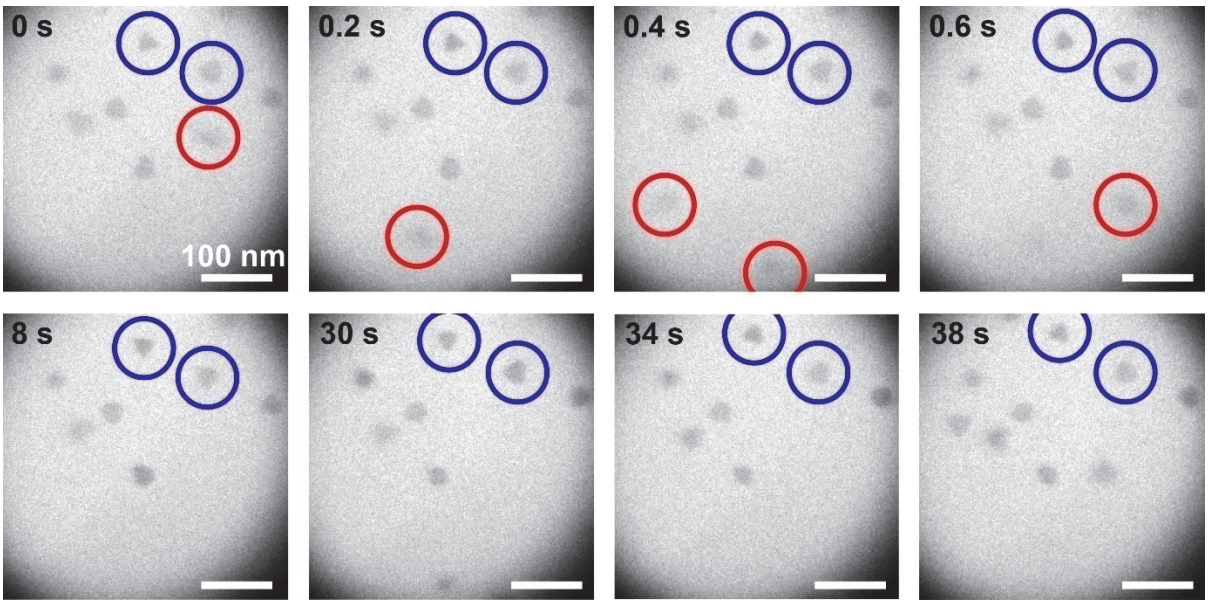

Figure 1.3 Particles slowed down by their interaction with the imaging window. Gold triangular nanoprisms that are attached to the window (highlighted in blue) exhibit slow and localized motion. Fast moving nanoparticles that are not attached to the window are highlighted in red.

A notable feature of liquid phase TEM is the specimen-window interaction. When imaged using liquid phase TEM, nanoparticles exhibit quasi-2D motion that is confined to a small volume of space near the window and they move via a stick-slip mechanism.[45] The particles that exhibit motion at the window are significantly slowed down when

compared to free particles moving in bulk solution, as indicated by diffusivities that typically differ by 7 to 9 orders of magnitude from the values predicted using the Stokes-Einstein relation,[42] suggesting that the overall interaction is short-range and attractive. When anisotropic nanoparticles dispersed in solution are imaged, they attach to the window in an orientation that maximizes their contact area, corroborating the speculation that the nature of the specimen-window interaction is attractive. Thus, nanorods are observed with their longitudinal axes aligned parallel to the plane of the window and triangular nanoprisms are seen with their faces lying down. However, it must be acknowledged that the imaged nanoparticles are only those that attach to the window in the first place. In other words, nanoparticles that don't attach to the window are moving too fast to be imaged and so usually evade detection despite being present in the solution. So our dataset of observations is intrinsically selective. This is illustrated in Figure 1.3 where a fraction of gold triangular nanoprisms are attached to the window while other unattached nanoparticles can still be observed in the same viewing region. The nanoparticles that are attached only exhibit slow translational and rotational motions, which are easily discernible with the temporal resolution of our CCD camera. In contrast, the nanoparticles that are not attached to the window move too fast, such that their shapes are not distinguishable and their trajectories are not identifiable with our camera. It is unclear whether the particles are attaching to the window because of an attractive interaction or the particles that attach only do so because they have lost their colloidal stability as a result of electron beam-induced damage.

It has been speculated that this specimen-window interaction is some combination of van der Waals and electrostatic interactions, but its exact nature has not been elucidated yet and conflicting reports have added to the confusion.[46–48] A systematic study that unambiguously characterizes the interactions involved and offers insights into ways to control them would greatly aid in the design of future liquid phase TEM experiments and interpretation of their results. One possible approach could look at functionalizing the windows with different ligands to tune the type or magnitude of the interactions, or alternatively to study how differently functionalized nanoparticles interact with the window. Even though the observed slow quasi-2D particle motion near the window is evidently an artifact of liquid phase TEM, it has actually been convenient for researchers. It allows nanoparticle dynamics to be studied without the need for a high speed detector and simplifies the analysis since particle configurations don't have to be reconstructed from their 2D projections, which may be nontrivial for anisotropic particles. Furthermore, when the dynamic process of interest is happening at a single particle level, it is often desirable for the particles to be strongly attached to the window so that motion blur is minimized.

Liquid phase TEM is an exciting new technique that expands the application of high resolution imaging capability of TEM so that it can be used to study the dynamics of nanoscale systems in liquid. Although electron beam-induced dynamic processes have been observed using conventional TEM of dry samples, including defect dynamics in graphene[49,50] and gold nanoparticle coalescence,[51] the types of processes that can be investigated are limited and thus TEM has been applied mostly for characterization of static nanostructures. Liquid phase TEM allows direct real-time visualization of motions and structural transformations of nanoparticles that take place in a liquid environment, and we expect this technique to benefit greatly from the upcoming developments in detector technology that would enable low dose imaging and faster image acquisition.

1.5 Electron beam-induced effects

For conventional TEM of dry specimens, well-documented damage mechanisms that take place during imaging include heating, electrostatic charging, ionization, atomic displacement (knock-on damage), and sputtering.[52,53] Heating is caused by the transfer of energy from incident electrons to the specimen as a result of inelastic scattering. Electrostatic charging results from ejection of secondary and Auger electrons, produced by both elastic and inelastic scattering, which is not compensated by the surrounding environment. Ionization is the excitation of the specimen from the energy provided by the incident electrons, leading to changes in the electronic configuration. This can result in breakage of chemical bonds, decomposition, or polymerization. Knock-on damage is the displacement of atoms into interstitial sites or vacancies as a result of momentum transfer from incident electrons during elastic scattering. Sputtering is when surface atoms undergo elastic scattering with incident electrons and are ejected from the specimen.

For liquid phase TEM studies, the nature of the electron beam perturbation on the specimen is drastically modified due to the presence of liquid. For our purposes, we will only consider the effect of electron beam irradiation on aqueous solutions. Mechanism of the electron beam interaction with aqueous solutions has been investigated intensively because of its relevance in nuclear industry and medical applications, whereas the chemical processes that result from irradiation are less well characterized for organic solvents. Electron beam irradiation induces radiolysis of water, ultimately resulting in the formation of hydrated electrons, hydroxyl radicals, hydroxide ions, hydrogen radicals, protons, hydroperoxyl radicals, hydrogen peroxide, and hydrogen via dozens of elementary reactions.[54–56] Both strongly reducing and oxidizing species, with relative yields that are dependent on the dose rate, are created in the irradiated area to form a complex chemical environment. Nanoparticle nucleation and growth processes are observed when a metallic precursor solution is irradiated, due to the reducing power of hydrated electrons. Etching of nanoparticles is seen when they are imaged in solution, due to their oxidative dissolution by hydroxyl radicals. Because of the delicate balance of so many coupled reactions involved, predicting which imaging conditions should be used presents a formidable challenge and so parameters are typically adjusted empirically. At high dose rates, bubbling due to hydrogen evolution is observed when the concentration of radiolytically generated hydrogen gas exceeds its solubility limit in solution.[57] Although this causes unwanted particle motion and contrast fluctuations, some researchers have taken advantage of this phenomenon by deliberately creating a large bubble inside the liquid cell, with the intention of improving the image contrast and resolution by reducing the thickness of the liquid layer that the electrons have to pass through.[58] Electrostatic charging of nanoparticles has been reported when they have been exposed to prolonged imaging, resulting in their sudden motion that is directed away from the center of the beam.[59] Thus, when studying nanoparticle dynamics in solution, the dose must be kept minimal to ensure that the particle motion is not being influenced by the electron beam. Aggregation of initially well-dispersed nanoparticles upon electron beam illumination has also been reported in numerous studies.[60–62] Even nanoparticles which are stable in acidic media are affected, suggesting that the electron beam-induced aggregation is not simply a result of the lowering of pH from the radiolytic generation of protons.[56] A more plausible explanation is that the organic ligands at nanoparticle surfaces are being

damaged, through either direct interaction with the electron beam or reactions with the radical species in solution. When the ligands are damaged, the nanoparticles lose their colloidal stability and aggregate. The local increase in the ionic strength due to the formation of ionic species during water radiolysis could also be responsible for the decrease in colloidal stability for charged nanoparticles.

The most obvious way to minimize electron beam-induced effects is to minimize the total dose and dose rate. In practice, implementing this is not trivial; the electron beam is being used for image formation, meaning that the dose can't be arbitrarily lowered without deteriorating the contrast and spatial resolution. In spite of this inherent limitation, the recent development of direct electron detectors that possess much higher sensitivities than CCD detectors may allow liquid phase TEM studies to be carried out at low dose. It has also been suggested that the use of liquid flow to replenish the solution may prevent the build-up of reactive radical species in the imaging region.[63] However, the effectiveness of this method is questionable since it takes approximately 1 millisecond for the products of water radiolysis to reach steady state concentrations in the irradiated region.[56] Even without flowing in a fresh solution, the solution in the imaging region is already being replaced by the surroundings via diffusion since the volume of liquid being irradiated only comprises a tiny fraction of the liquid cell. A more effective approach would be to intentionally introduce radical scavengers into the solution to selectively remove the undesired products of water radiolysis. Radical scavengers will react preferentially with the target radicals to form more benign species, thus acting as sacrificial protecting agents.

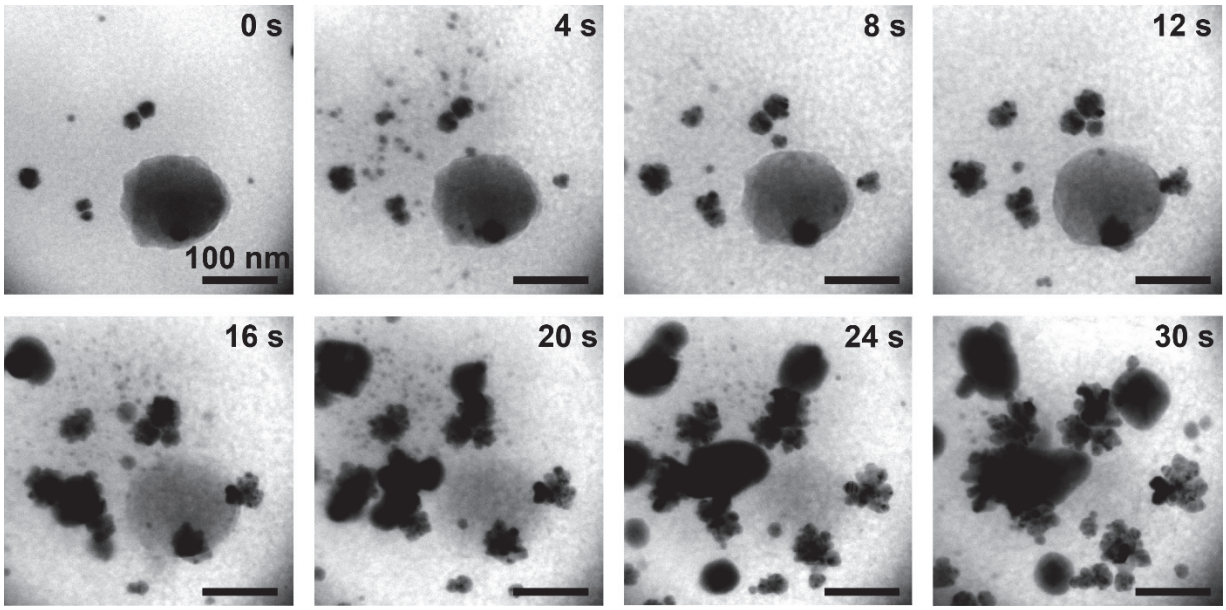

Figure 1.4 Electron beam-induced nanoparticle nucleation and growth. Gold nanoparticle nucleation and growth from the precursor solution under electron beam irradiation.

Electron beam-induced nucleation and growth of gold nanoparticles from $HAuCl_4$ solution is shown in Figure 1.4. It has been proposed that hydrated electrons from water radiolysis reduce the metallic precursor; in this case the Au(III) precursor has been reduced to Au(0). When electron dose and dose rate are high, the Au(III) precursor is

rapidly reduced upon electron beam irradiation and nanoparticle growth is determined solely by the monomer diffusion rate. Diffusion-limited growth leads to the formation of highly branched dendritic structures where the exact fractal dimension presumably depends on the concentration of the *in situ* generated hydrated electrons.[64,65] The dual role of the electron beam, both as the imaging probe and the external stimulus to initiate the metal precursor reduction, has been widely exploited by researchers to investigate the nucleation and growth processes of nanoparticles with varying chemical compositions and shapes.[44,66–71] Unprecedented atomic resolution imaging of nanoparticle nucleation and growth dynamics in real time has already been reported,[44,69] fully displaying the unique advantages of liquid phase TEM. Nevertheless, the challenge of correlating these results to benchtop experiments still remains. Thus far, it has not been possible to observe the nucleation and growth of nanoparticles that exhibit size and shape uniformities using liquid phase TEM,[69,70] an indication that a high level of control over the liquid cell environment has not yet been attained. Furthermore, the extent to which the non-classical growth mechanisms that have been reported were influenced by the electron beam is also unclear.[44,66] With the latest advent of direct electron detectors that allow imaging at low dose rates, it may be feasible that the kinetics of nucleation and growth can be controlled in future studies. It is expected that if mild reducing conditions can be maintained during electron beam illumination, reaction-limited rather than diffusion-limited growth should occur, leading to *in situ* liquid phase TEM studies that more closely resemble conventional colloidal synthesis of nanoparticles.

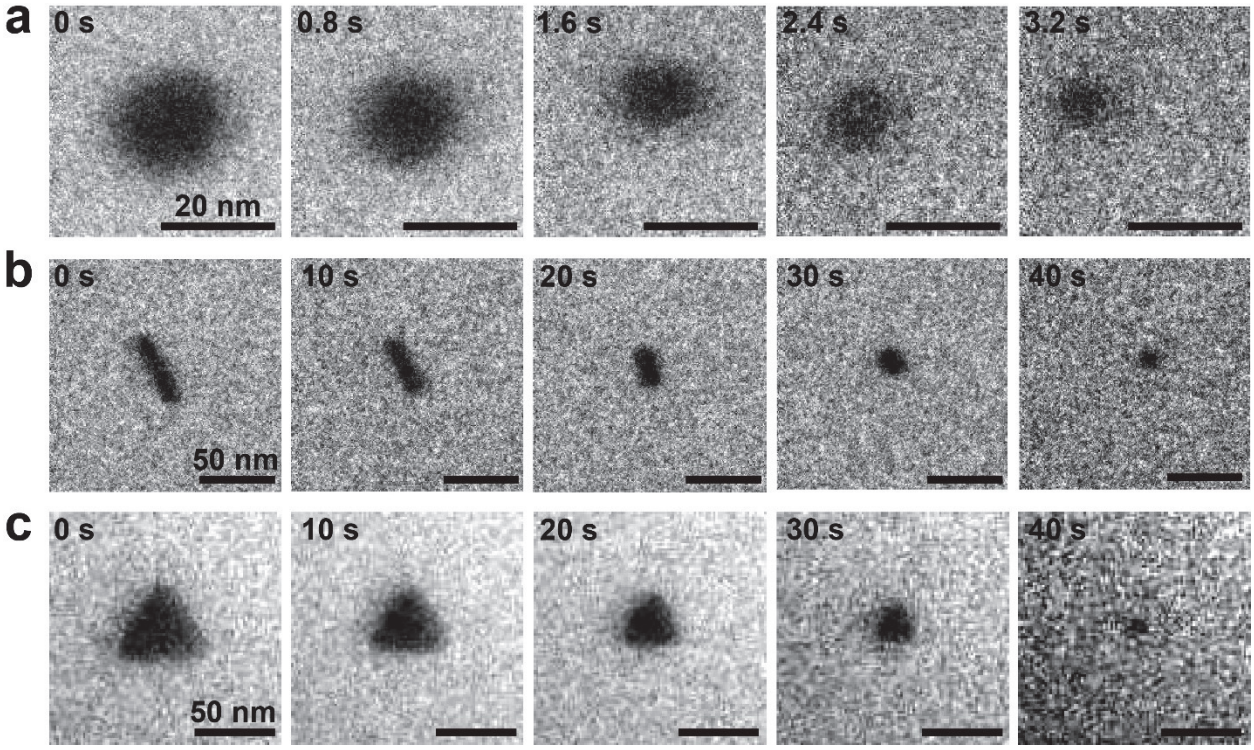

Figure 1.5 Electron beam-induced nanoparticle etching. Time series of TEM images showing oxidative dissolution of gold nanoparticles during liquid phase TEM imaging. (a) Nanospheres. (b) Nanorods. (c) Triangular nanoprisms.

Oxidative dissolution of nanoparticles by hydroxyl radicals is often observed when metallic nanoparticles are imaged in aqueous environments. As shown in Figure 1.5, ligand-capped gold nanoparticles that possess high colloidal stabilities undergo oxidative dissolution upon electron beam illumination. It has been suggested that the presence of halides in the solution may aggravate etching, as halides can react with metallic ions to form stable metal complexes.[72] Since gold nanoparticles are typically synthesized with ligands that have halides as counterions, it should be possible to increase their stability against oxidative dissolution by performing a postsynthetic ligand exchange to remove the halides from the solution. We can also counteract oxidative dissolution by purposefully introducing radical scavengers to selectively quench the hydroxyl radicals. The use of isopropanol to this effect has been demonstrated already,[72] and isopropanol is certainly not unique in its ability to act as a hydroxyl radical scavenger. Other simple alcohols, such as methanol and ethanol, as well as numerous other molecules including DMSO, formamide, acetonitrile, and dioxane can also act as hydroxyl radical scavengers.[73,74] Ascorbic acid, or more commonly known as vitamin C, is a natural antioxidant found in the body and so is a particularly attractive choice if biocompatibility needs to be taken into account. Dopamine, which is a neurotransmitter agent, is another naturally occurring molecule with antioxidant properties.[75] Since it is possible to coat colloidal nanoparticles with a polydopamine shell,[76] perhaps a viable method for creating nanoparticles that are highly resistant to oxidative dissolution would be to coat them with a surface layer of polydopamine while having other hydroxyl radical scavengers in solution.

For the purposes of studying interactions and assembly of nanoparticles, oxidative dissolution is an electron beam-induced artifact that must be eliminated. Nevertheless, this phenomenon can be exploited for carrying out *in situ* nanoparticle etching studies that analyze the kinetic pathways of shape transformations at a single particle level in real time. As seen from Figure 1.5, oxidative dissolution of anisotropic nanoparticles initially proceeds at different rates for different crystal facets, with the result that their shape anisotropies are gradually reduced over time to yield quasi-spherical particles. Although a direct comparison of how the stabilities of anisotropic gold nanoparticles toward oxidative dissolution depend on their individual shapes is not possible from Figure 1.5 as these images were taken at different electron dose rates, a thorough future study that examines etching rates of a variety of anisotropic nanoparticles at a controlled dose rate may yield quantitative data concerning the relative energetic stabilities of different crystal facets. This would necessitate the use of near-atomic resolution TEM and would require accurate control over the liquid thickness and electron dose rate, as well as the ability to minimize the extent of particle etching that may take place before data collection can begin under desired conditions. A recent study has also shown that controlled *in situ* etching of anisotropic nanoparticles in a liquid cell can shed light on the nature of unexpected transitory species that appear during shape transformations, which are very difficult to isolate and characterize using other techniques.[77]

It is no secret that research using liquid phase TEM is currently restricted by the lack of control we can exercise over the influence of the electron beam. In the liquid phase, the complex interplay of chemical reactions that take place as a result of water radiolysis makes it demanding for researchers to systematically decouple and selectively counteract its effects. Notwithstanding these complications, researchers have so far been successful in identifying the interesting scientific questions that exploits the known effects of the

electron beam, leading to discoveries of how nanoparticles nucleate and grow,[44,66,69] how nanoparticles undergo shape transformations during oxidative dissolution,[77] and so on. As a matter of fact, almost every technique available today that aims to characterize nanoparticles at a single particle level suffers from its own set of perturbations on the system under study. Nevertheless, we must invest more effort into enhancing our present level of understanding about how the electron beam is affecting the specimen and the dynamic process that takes place, with the ultimate goal of being able to control it in a predetermined way.

Chapter 2

Quantifying Interactions of Charged Colloidal Gold Nanorods from Their Dynamics

Adapted with permission from: Q. Chen*, H. Cho*, K. Manthiram, M. Yoshida, X. Ye, and A. P. Alivisatos, “Interaction Potentials of Anisotropic Nanocrystals from the Trajectory Sampling of Particle Motion using in Situ Liquid Phase Transmission Electron Microscopy” *ACS Central Science* **2015**, *1*, 33–39. DOI: 10.1021/acscentsci.5b00001. (* denotes equal contribution)

2.1 Background

Understanding how nanoscale objects interact and communicate in the solution phase is a critical underlying issue for both biological[78–81] and artificial systems.[1,7,9,11] Inside a living cell, small biomolecules often self-assemble into super-complexes with essential functions, such as channel formation[79,80] and protein cooperativity,[78,81] via various forms of noncovalent interactions. Similarly, colloidal nanocrystals have been spatially arranged into larger assemblies, in order to take advantage of their collective properties in optics,[82–87] electronics,[88–90] and catalysis.[91,92] For both classes of systems, computational efforts[93–99] have taken the lead to model and understand the interactions essential to solution phase assembly processes at nanometer or subnanometer resolution. One commonly adopted strategy to measure the interaction potential between micrometer-sized colloidal particles is to directly image the colloidal dynamics in solution using optical microscopy.[13–15] This strategy, however, has not been extended to the study of nanoscale interactions due to the nanometer resolution required for direct imaging. For nanoscale objects, the relevant interactions are usually effective within the range of a few to hundreds of nanometers at most. For any technique of this type to be broadly useful, it should be able to correlate interaction potentials with the shape or surface chemistry of nanoscale building blocks. Until recently, conventional electron microscopy techniques that offer nanometer scale resolution required high vacuum and thus were considered to be incompatible with solution phase dynamics. The multiple recent demonstrations of *in situ* observations of a wide range of nanoscale dynamic processes using liquid phase TEM[44,58,60,61,69,100–104] opens up the possibility of determining full anisotropic pairwise and higher order interparticle potentials for nanoscale objects at high spatial resolution by trajectory tracking. Here we demonstrate such an approach for the case of gold nanorods.

Gold nanorods are an important system for which the determination of the anisotropic interaction potentials will be of great use.[105,106] Gold nanoparticles exhibit strong plasmon resonances and for nanorods, the resonance frequency is tunable through the control over their aspect ratio, making them a useful probe for biological imaging with dark field microscopy and a strong candidate for photothermal cancer therapies.[107,108] When two gold nanorods are placed in close proximity, their plasmon resonances couple to each other strongly. This results in a broader class of plasmonic molecules with spectra that can be designed with precision, leading to 3D plasmon rulers, electromagnetic induced transparency and many other collective phenomena.[82,109,110]

The ability to understand and control the assembly of these nanocrystals hinges on knowing their interaction potential, and this in turn depends very strongly on the liquid environment. The ability to visualize elementary assembly processes under different solution parameters, such as salt concentration, will be of immediate use in the creation and testing of models and theories for nanocrystal assembly.

We used gold nanorods as our model system to study the more generic particle shape effect on interaction profiles, which can be readily applicable to other anisotropic colloidal nanocrystals and nanoscale objects. Gold nanorods can be synthesized with high shape purity and size uniformity,[111,112] which facilitates the collection of a statistically significant dataset for quantitative analysis. Their high electron density enables the acquisition of high contrast TEM images for image processing.

2.2 Preparation of charged colloidal gold nanorods

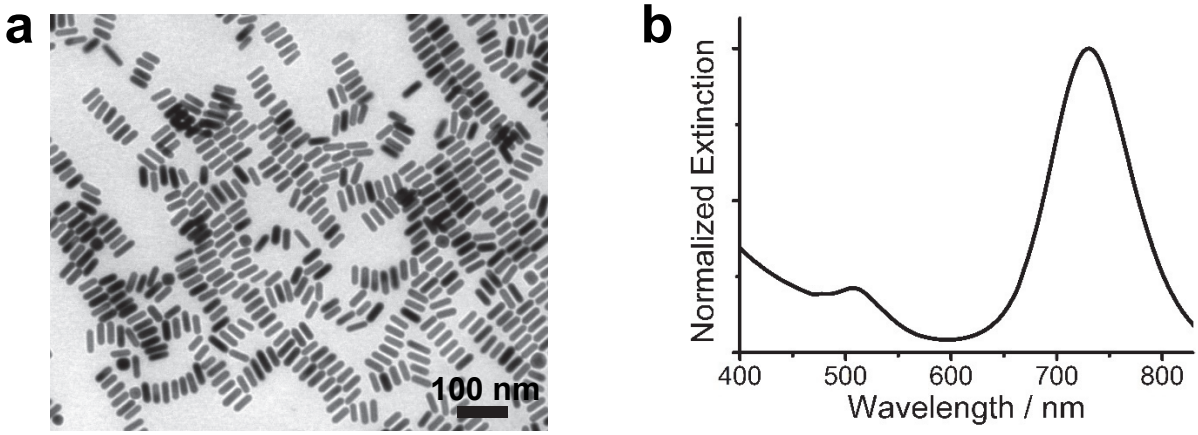

Figure 2.1 Synthesis and characterization of gold nanorods. (a) TEM image of synthesized gold nanorods. (b) UV-Vis spectrum of gold nanorods in solution.

Gold nanorods that are capped with a bilayer of cetyltrimethylammonium ions (CTA^+) were obtained using the published method of silver-assisted seed-mediated synthesis where a seed solution is injected into a growth solution that contains a binary surfactant mixture.[112] The seed solution was prepared as follows: 5 mL of 0.5 mM $HAuCl_4$ was mixed with 5 mL of 0.2 M cetyltrimethylammonium bromide (CTAB) in a 20 mL scintillation vial. 1 mL of freshly prepared 6 mM $NaBH_4$ was injected quickly into the Au(III)-CTAB complex solution under vigorous stirring (1200 rpm) for 2 min. The stirring was stopped after 2 min and the seed solution was aged for 30 min at 30 °C. The growth solution was obtained by first co-dissolving 6.15 g of cetyltrimethylammonium chloride (CTAC) and 1.543 g of sodium oleate in 250 mL of water at 45 °C. After allowing the binary surfactant mixture to cool to 30 °C, 12 mL of 4 mM $AgNO_3$ and 250 mL of 1 mM $HAuCl_4$ were added followed by the addition of 2.1 mL of 12.1 M HCl. The growth solution was kept at 30 °C, as monitored by an IR thermometer, under gentle stirring (200 rpm) until the solution became colorless. To initiate rod growth, 1.25 mL of 64 mM ascorbic acid was first added to the growth solution and stirred for 1 min. Then 0.8 mL of the seed solution was diluted with 0.2 mL of water and the resulting diluted seed solution was injected into the growth solution. Stirring was stopped immediately after the injection and

the rods were left to grow for 12 h at 30 °C. Rods were purified by centrifugation at 7000 rpm for 30 min and concentrated to give the 15 mL stock solution.

The synthesized gold nanorods were 47.4 ± 2.3 nm in length and 13.8 ± 1.0 nm in diameter as analyzed from TEM images of 50 rods (Figure 2.1a). The aspect ratio of the rods obtained was 3.43 ± 0.30 and the transverse and longitudinal peaks in the UV-Vis spectrum were measured to be 507 nm and 730 nm respectively (Figure 2.1b). Our rod sample contained a small fraction of spherical impurities that could not be removed by centrifugation.

2.3 Tip-to-tip assembly of gold nanorods

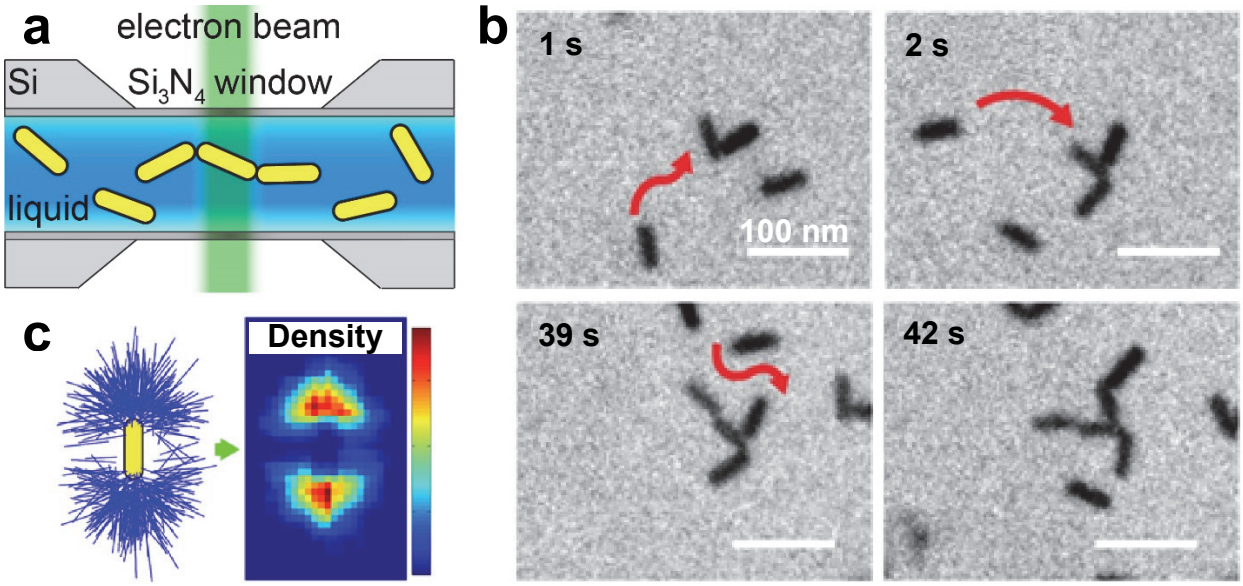

Figure 2.2 Direct real-time imaging of tip-selective gold nanorod assembly. (a) Experimental setup for TEM imaging of gold nanorod dynamics in solution using a silicon nitride liquid cell. Gold nanorods, which are colloidally stable outside of the electron microscope, assemble under electron beam illumination. (b) Time series of TEM images showing how gold nanorods approach and attach to each other. Red arrows highlight the trajectories of nanorods before they attach to the cluster of growing rod assemblies. (c) Rod position plot from approximately 300 rod-rod attachments. Blue lines are the observed positions of other rods relative to the reference rod drawn in the center. This plot is then converted into a density map of attached rods relative to the reference rod. The rods exhibit a preference to attach at the tips (note the positions of dark red pixels).

For liquid phase TEM imaging of collective dynamics of charged gold nanorods, we used commercially available Poseidon 200 *in situ* liquid cell TEM flow holder and E-chips (Protochips) as shown in Figure 2.2a. The microchips with 50 nm thick silicon nitride viewing windows were cleaned with acetone and methanol before undergoing plasma treatment to increase the hydrophilicity of the window surface. A miniscule droplet (1 μL) of water was then pipetted onto the bottom microchip (150 nm flow spacer) followed by loading of the top microchip. Crossed-window configuration of the E-chips gave a viewing

window of dimensions 20 μm × 20 μm. Sealing of the liquid cell against high vacuum conditions was accomplished using screws that tightly secured the microchips and o-rings in place. Gold nanorod solution was flowed in and allowed to stabilize rather than being loaded directly as direct loading often led to a fraction of the rods becoming immobilized on the window. Sample was flowed in for approximately 1 h to ensure that the solution inside the liquid cell was homogeneous. The flow was then stopped and the system was left to equilibrate for at least 15 min to preclude any effects of residual flow.

Upon electron beam illumination, individual gold nanorods that were initially dispersed in solution started to attach to the silicon nitride window and became visible within the field of view. They then appeared to move in a quasi-2D plane close to the window and started to assemble irreversibly (Figure 2.2b). The *in situ* self-assembly region was highly localized within the imaging area, indicating that it was initiated by electron beam perturbation. When the electron beam was shifted to a new region, we saw individual and well-separated nanorods at the beginning as before but then they too were triggered to assemble after only seconds of electron beam illumination. This electron beam induced self-assembly appeared to be relatively robust toward imaging conditions, occurring within a dose rate range of 17.3 to 67.1 electrons/($Å^2$·s) under an accelerating voltage of 200 kV.

We saw an interesting long-range effect when we looked closely into the detailed steps of self-assembly. A pair of approaching gold nanorods first appear to become aligned in their relative orientations from a distance before they physically touch, suggesting the presence of long-range interactions that favor certain orientations. This reorientation process is distinct from the conventional diffusion-limited or reaction-limited aggregation mechanisms[61,113], which involve solely short-range attractive interactions. After nanorods reorient, they attach, at most times irreversibly, in a tip-to-tip fashion (Figure A1 in the Appendix). The time series of TEM images in Figure 2.2b highlights the free nanorods being added to the growing cluster of nanorods, stepwise with their orientations not perfectly aligned at the beginning but fine-tuned later with the protruding nanorods within the cluster to achieve tip-to-tip attachments.

In Figure 2.2c, the plot of the positions and orientations of all the nanorods for approximately 300 attachment events is shown. The density plot (right side of Figure 2.2c) of these attached nanorods shows a clear preference for nanorods to attach at the tips. Such a strong preference for tip-to-tip attachment was remarkable considering that the CTA^+-capped gold nanorods did not have known tip-specific chemical functionalities and the same nanorods typically pack densely in a side-by-side fashion when they undergo drying-mediated assembly (Figure 2.1a). Packing densities of CTA^+ are lower at the nanorod tips than at the sides due to constraints imposed by the geometric curvature, and this knowledge has been exploited for selective tip-functionalization as the ligands at the tips are replaced more easily.[114] However, it would be too premature to conclude without further analysis that the nanorods exhibit tip-selective assembly due to the tips suffering from electron beam-induced ligand damage to a greater extent than the sides. To elucidate the attachment mechanism, we must attempt to understand the interactions that are present in our system in a quantitative way. From the trajectories of the nanorods that we have obtained, we can extract the interaction potential profile through the radial distribution function analysis. Before we proceed to apply this method that is based on statistical mechanics, we must first show that the gold nanorods exhibit Brownian motion.

2.4 2D Brownian motion of gold nanorods

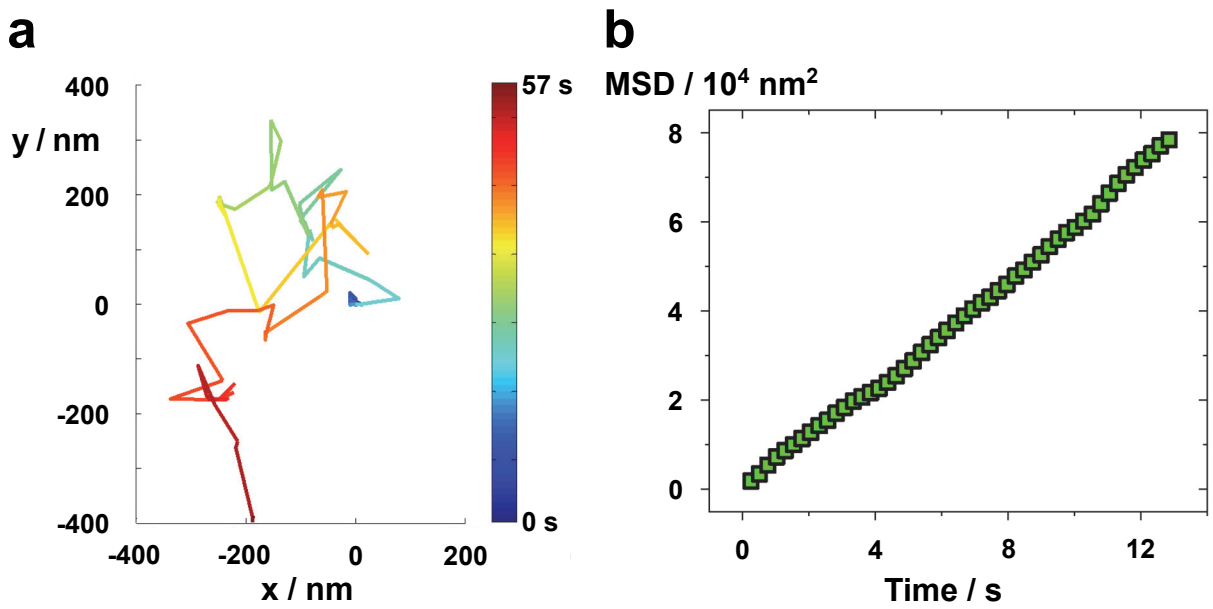

Figure 2.3 2D Brownian motion of individual gold nanorods. (a) A typical single nanorod trajectory showing the changes in its centroid position with respect to time, color-coded according to the elapsed time. (b) Mean squared displacement (MSD) versus time plot for the nanorod trajectory shown one in (a).

Empirically, we observed that the gold nanorods move in a quasi-2D plane close to the silicon nitride window to which they are attracted to. It was found that at the particle concentrations that we used, the rods usually attach to only one of the two windows, although tip-to-tip assemblies were observed to grow at both windows in some cases as inferred from the presence of out-of-focus particle assemblies seen during TEM imaging. Presumably, this nanorod-window attraction is relatively weak since we still observe the dynamic adsorption and desorption of nanorods coming to and leaving the focal plane at the window. When the concentration of gold nanorods was too low for them to interact with each other, they appear to move randomly within the field of view as shown in Figure 2.3a. The Brownian nature of their motion was confirmed by plotting their mean squared displacement with respect to time, which showed a linear dependence (Figure 2.3b).

Perhaps Brownian motion of gold nanorods was somewhat expected since we were careful to exclude any external forces that could bias their direction of motion in the liquid cell. Nevertheless, it was important to confirm this since we must ensure that individual nanorods exhibit Brownian motion and thus sample all available configurations before we can apply statistical analysis for our system. Although the nanorod-window interaction means that the rods exhibit 2D rather than 3D motion in solution, this is somewhat fortunate since it makes analysis simpler in terms of identifying the locations and orientations of the nanorods. In addition, since this interaction acts in the direction that is normal to the 2D plane where motion is confined to, we can neglect the contribution of nanorod-window interaction to the energetics of nanorod dynamics except that the observed motion is much slower than it would be for free particles moving in 2D.

2.5 Quantifying interactions via trajectory mapping

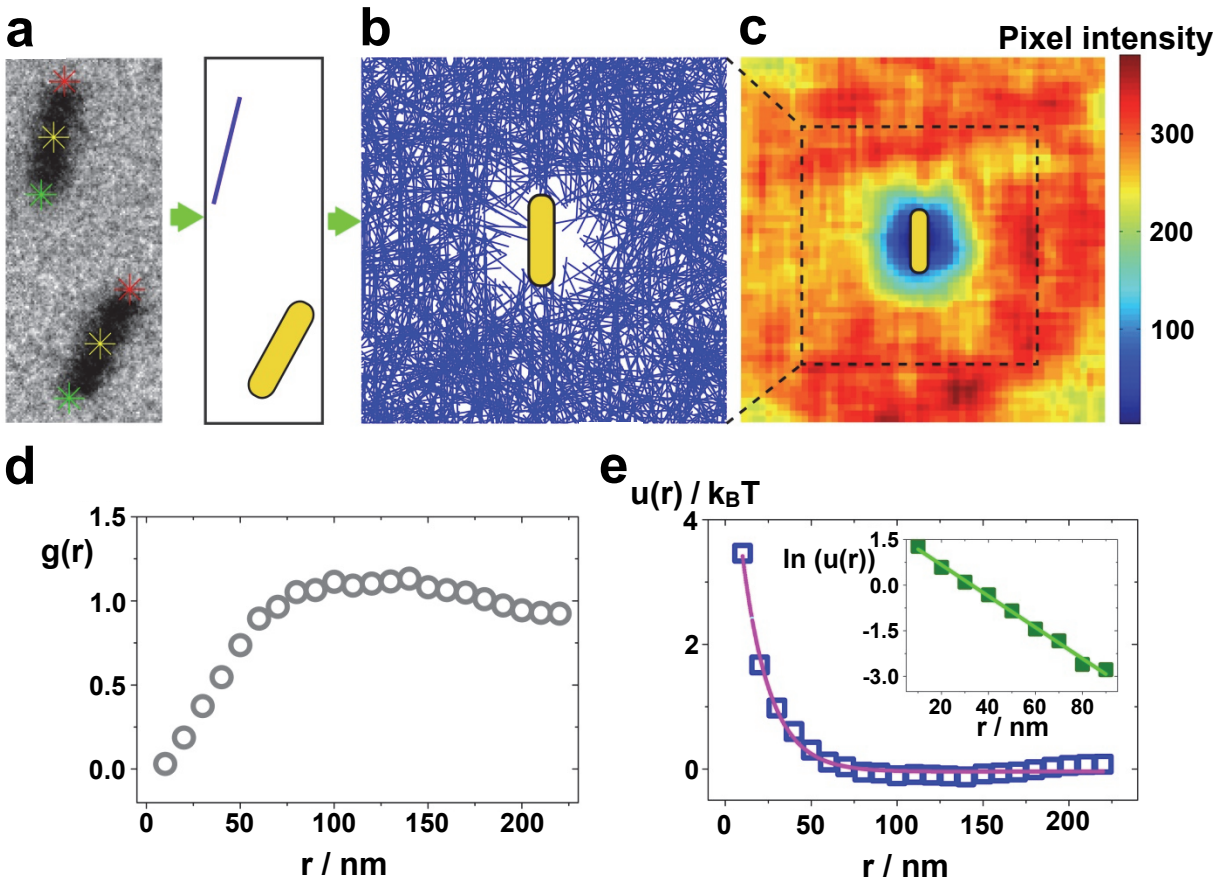

Figure 2.4 Extracting the pairwise interaction potential from nanocrystal dynamics. (a) TEM image highlighted with tracked positions of gold nanorods at their tips (red and green stars), and their centroids (yellow stars). In this pair, the bottom rod was chosen to be the reference rod, and the top rod was simplified as a blue line. (b) Rod density plot, where the blue lines are the observed positions of other rods relative to the vertical reference rod (drawn to scale in the center). The data was obtained from around 10000 pairs of rods, but for clarity only randomly chosen 1/8 of the data was plotted in this figure. (c) The color-coded counts of total number of rods in the 2D plane composed of 5 nm × 5 nm pixels. Color bar shows the corresponding counts. (d) g(r) vs r plot. (e) u(r) vs r plot with its exponential fitting (purple line). The inset shows the exponential decay relation of u(r) by illustrating the resultant linear relation of ln (u(r)) vs r.

Our first quantitative analysis was to map out the many different ways one rod approaches the other, which shows a depleted zone overlaid with the reference rod shape. The underlying statistical mechanical argument of this analysis is simple: rods follow the more probable path, i.e. instantaneous relative positions, toward each other that corresponds to the lower free energy. In practice, we first tracked the tip positions for a pair of nanorods in the same TEM image (see Figure 2.4a). We chose one rod as the reference rod and place it vertically centered at the origin, and then repositioned the other

accordingly such that their relative configurations remain unchanged. This repositioned second rod was simplified as a blue line as shown in Figure 2.4a. For image analysis, we used the Matlab imaging processing toolbox to track the tips of gold nanorods before they assembled. We first read every TEM image in a given movie and generate its complement with reverse intensity scale, with the originally dark gold nanorods now appearing bright in the complement image. Then we used an optimized threshold to generate a binary image from the intensity-inverted image. Based upon the binary image, we used the built-in functions of bwboundaries.m and regionprops.m to find the outlines of the desired bright clusters, i.e. the gold nanorods in the image, and to extract their centroids and orientations, which are needed to compute the tip positions of the rods. For a given image being analyzed, each rod is selected as a reference rod in turn. We had to discard movies where the contrast and spatial resolution were not high enough for accurate identification of particles. Spherical particles (i.e. impurities) were filtered and disregarded by imposing an aspect ratio threshold.

This automatic pairwise position sampling allowed us to accumulate approximately 10,000 pairs of nanorod interactions, and to construct a map of all the observed rod positions and orientations relative to the vertically oriented reference rod at the origin (Figure 2.4b). There is a zone at the origin where other rods are repelled from the reference rod. We determined the shape of this depleted zone by calculating and plotting the total number of rods falling in each 5 nm × 5 nm pixel around the reference rod (Figure 2.4c). The zone periphery has a circular symmetry and so touches the tips of the central reference rod, but extends away from its sides; this is consistent with the observation that approaching rods become reoriented with respect to each other before they attach tip-to-tip, while they do not attach side-by-side. Despite the overall isotropic shape of the resulting depletion zone, the anisotropy of the rod shape means that the underlying interactions are anisotropic and depend on the relative rod orientations.

In addition to the qualitative matching of the shape of the depleted zone to the observed tip-to-tip assembly, we quantitatively determined the radial distribution function to extract the mathematical form of the interactions responsible for how rods approach each other. The radial distribution function, g(r), can relate our experimentally measured rod densities to inter-rod pairwise interactions. We only use one spatial parameter, r, the radial distance of a given pixel to the origin, to describe g(r) since the experimentally obtained rod density plots (Figures 2.4b and 2.4c) are both radially symmetric to a good approximation. But the same analysis can also be applied even if the density plot is radially dependent as long as additional orientation parameters are included. We plotted g(r) vs r as shown in Figure 2.4d using the definition for g(r) stated previously in Figure 1.1 and Equation 1. The average areal density of rods was calculated within the circular area of radius 250 nm. In this particular experiment, the nanorod concentration was considered to be low enough to assume that the nanorods only interact in a pairwise manner; g(r) is thus directly related to the pairwise interaction u(r) via the relation given before in Equation 2. When the nanorod concentration is too high, this assumption no longer holds and a nanorod situated at r experiences not only the interaction with the reference rod at the origin but also with other neighbors. These multibody interactions become more significant at higher particle concentrations since there are more neighbors to interact with. In such cases, g(r) will then be related to the interparticle potential via the following equation:

$$g(r) = \mathrm{e}^{-\frac{u(r)}{k_B T}}\ y(r) \tag{3}$$

where y(r) is the cavity distribution function given by:

$$y(r) = 1 + \sum_{n=1}^{\infty} \rho_{avg}^{n}\ y_n(r) \tag{4}$$

In other words, one can still extract u(r) from iterative fitting of g(r) considering higher order contributions from pairwise interactions as long as such multibody interactions remain equivalent to the summations of many pairwise interactions.

As shown in Figure 2.4e, when r is small, u(r) assumes large positive values which correspond to strong repulsive interactions. This is consistent with the existence of the central depleted zone. Then u(r) decays to zero at larger r, which confirms that our data set is indeed statistically significant since we expect rods to not interact when they are far away from each other. Fitting of the u(r) vs r curve shows that u(r) decays exponentially with r, the decay constant being 16.0 ± 0.7 nm (see Figure 2.4e). This exponential decay profile, obtained for the first time from *in situ* observation of nanoscale dynamics, is reminiscent of screened electrostatic repulsion between cylindrical surfaces coated with small charges, where the decay length is effectively the Debye length.[8] Indeed, the gold nanorods used here derive their colloidal stability from a bilayer of CTA^+ at their surfaces, resulting in positively charged surfaces that provide them with electrostatic stabilization against aggregation.[115–117] The electrostatic nature of interparticle repulsion can explain why the otherwise well-dispersed gold nanorods self-assembled only upon electron beam illumination: radiolysis of water under the electron beam generates additional reactive species, including hydrated electrons, that increase the local ionic strength of the solution and shorten the screening length.[56] The resulting decrease in the Debye length allows the rods to come into closer proximity where shorter range attractive interactions can take over and bring the rods fully into contact. This is consistent with a previously reported study, where the zeta potential of a charged gold nanosphere solution was found to decrease upon electron beam irradiation using a van der Graff generator, with this effect being attributed to the increased ionic strength from water radiolysis.[61]

It must be acknowledged that the extracted interaction potential profile shown in Figure 2.4e is incomplete. Since we observe irreversible assembly of the gold nanorods, there must be an attractive component in the interaction which dominates at small separations. So the potential curve in Figure 2.4e is only showing the long-range repulsive portion of the total interaction potential. The fact that we were not able to experimentally discern the features of this short-ranged attractive component in the interaction potential can be attributed to the limit imposed by our CCD camera. We did not have enough temporal resolution to accumulate significant statistics for very small inter-rod distances (less than 10 nm). In the movies we obtained, it appears as though the rods snap together at the last instant because our temporal resolution was too low. Although the origin of this short-range attractive interaction can't be elucidated from the analysis of our trajectory data alone, we assign this as the van der Waals interaction based on the DLVO model for charged colloidal particles. Although other attractive interactions may be present, such as depletion forces due to CTAC micelles in solution acting as depletants or possible dipolar interactions of rods due to the polarizable nature of gold nanoparticles, their contributions are expected to be relatively minor in comparison to van der Waals forces.

2.6 Modeling the gold nanorod interactions

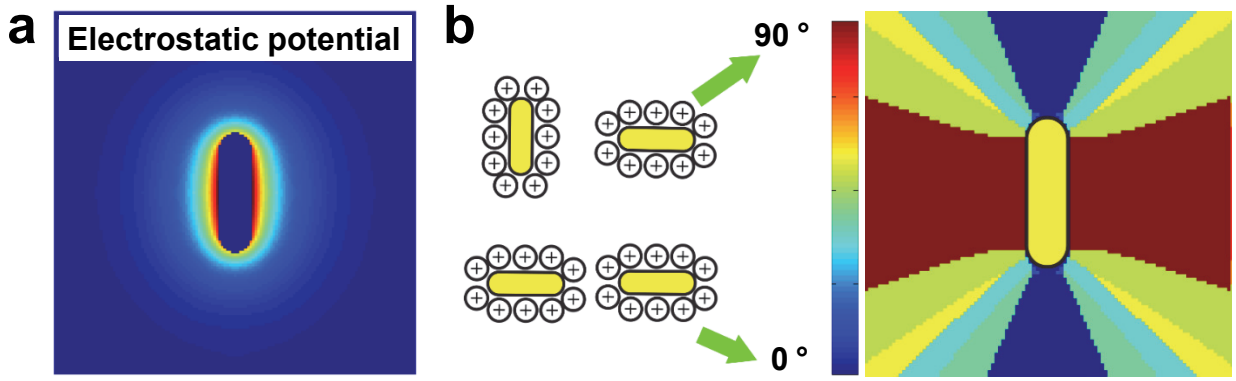

Figure 2.5 Modeling of pairwise electrostatic interactions. (a) Energy contour plot showing the calculated lowest potential surface for a pair of nanorods, where one rod stays vertically at the center and the other samples all the possible rod orientations at each pixel. The potential at each pixel is color-coded; red for strong electrostatic repulsion and blue for weak electrostatic repulsion. At the rod side positions, the potential energy is approximately 2 times higher than at the rod tips. (b) Calculated orientation of rods for the lowest energy at each pixel, with blue and red colors for parallel and perpendicular orientations, respectively, as shown schematically on the left.

We used theoretical modeling to corroborate our experimental findings. We model our charged gold nanorods as 2D rod shapes (2D spherocylinders or stadiums) coated at the boundary with a large number of point charges. We then obtain the electrostatic repulsion of two rods at any given relative configuration by summing all screened pairwise interactions between the point charges. This simplified model is based on the 2D projection of rods where the charges only exist at the 2D boundaries of the rods. Still, due to the rotational symmetry of nanorods along their long axis, their 2D projection is essentially a rescaling of their 3D shape. While the values of calculated electrostatic interactions would be different for 3D modeling, the qualitative trend that tip-to-tip assembly is more energetically favorable than side-by-side assembly will not change.

Each gold nanorod is modeled numerically with a 47 × 14 shape matrix, with each surface element coated with a point charge. While the magnitude of this point charge is arbitrary, the shape of the calculated electrostatic interaction shape is expected to stay independent of the exact charge density. The electrostatic potential between two gold nanorods at fixed positions is calculated by summing the pairwise interactions of the point charges, with the assumption that neither interferences nor correlations influence the potential between neighboring point charges. The point charges on interacting colloids interact via a screened Coulomb potential (Yukawa potential), $V_E(i,j,I)$:

$$V_E(i,j,I) = \frac{1}{4\pi\varepsilon_o\varepsilon_r D_{ij}} \exp\left(-\frac{D_{ij}}{\lambda_D(I)}\right) \quad (5)$$

where D_{ij} is the distance between the two point charges being considered and $\lambda_D(I)$ is the Debye length for a given ionic strength, I. For our calculations, we set $\lambda_D(I)$ to be equal to the experimentally obtained value of 16 nm.

Figure 2.5a shows the energy contour plot corresponding to rod configurations that minimize the electrostatic repulsion for a given pixel position. The electrostatic repulsion around the reference rod is much weaker at the tips than at the sides, which is consistent with the observed tip-selectivity. The equipotential lines around the reference rod is ellipsoidal at very small distances (less than 10 nm) from the rod surface. However, this anisotropy in the potential only manifests itself at distances shorter than what we can resolve from our experimental data obtained using liquid phase TEM. The shape becomes more circular further away from the reference rod surface, just like the shape of the experimentally observed depleted zone periphery. Figure 2.5b, on the other hand, maps out the rod orientations with the lowest energy. Rods are more likely to point parallel toward each other at the rod tip, consistent with our experimental observations, which further corroborates the electrostatic nature of repulsion. Our simple theoretical model appears to be sufficient for illustrating the role of long-range electrostatic repulsion to explain the selective tip-to-tip assembly that we experimentally observed.

Our analysis so far allows us to propose a mechanism by which charged gold nanorods assemble tip-to-tip: individual gold nanorods first randomly move, enveloped by a repulsive cloud with dimensions that depend on the ionic strength of the solution. They can only come close to each other when their repulsive clouds experience the least overlap, i.e. the smallest repulsion, which occurs specifically when they approach tip-to-tip. When their separation is sufficiently small, short-ranged attractions, originating from van der Waals interactions, take over and permanently lock the rods into tip-to-tip oriented assemblies.[118] The fact that we were not actually able to distinguish the short-ranged attractive component in the interaction profile, together with the inherently complicated orientational dependence of rod-rod electrostatic interactions, is the reason why we chose not to fit our experimental data with DLVO theory, but instead use the theoretical modeling that accounts for the shape details of nanorods for a direct comparison.

2.7 Non-assembly due to long-range repulsion at a lower ionic strength

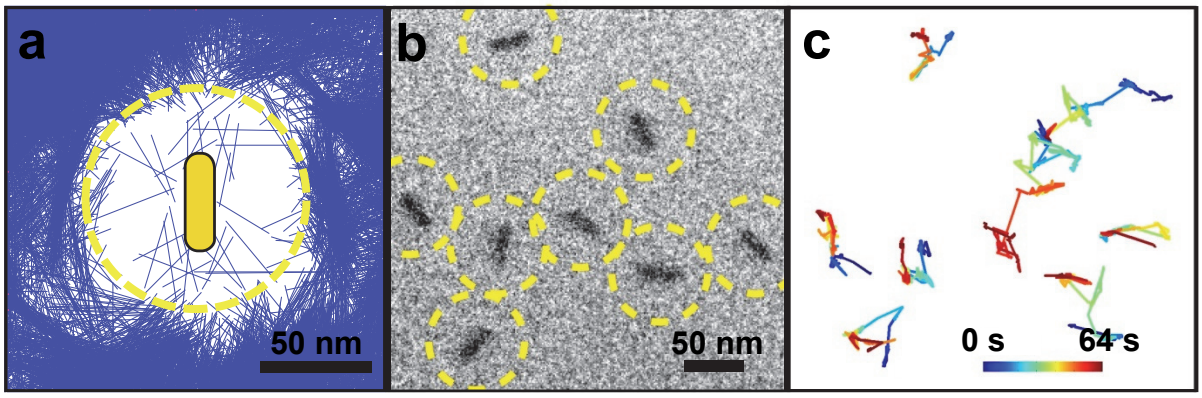

Figure 2.6 Charged gold nanorods repel each other at low ionic strength. (a) Plot of different rod configurations (each rod plotted as a blue line) relative to the central reference rod. The yellow dotted line circle indicates the depleted zone. (b) TEM image of electrostatically stabilized gold nanorods overlaid with yellow dotted depleted zones. (c) Trajectories of all the eight nanorods in (b).

As we now understand the interactions governing assembly, we are able to counteract the electron beam effects and correlate our *in situ* observations with benchtop experiments. We decreased the ionic strength of the gold nanorod solution and investigated the nanocrystal dynamics with liquid phase TEM. We lowered the ionic strength by centrifuging the stock solution (7000 rpm for 30 min), thus removing the supernatant that contained excess residual electrolytes from the synthesis, and then re-dispersing the gold nanorods in a solution that only contains CTAC (38 mM). Centrifugation and redispersion were repeated two more times. The final volume was kept to be the same as the original volume of stock solution to ensure that the rod concentration remained constant. We redispersed the gold nanorods in a solution containing excess ligands to prolong their colloidal stability under electron beam illumination. Even if a fraction of the ligands at the nanorod surface gets damaged during imaging, there will always be pristine ligands in solution nearby to replace them. As before, this solution was then diluted by a factor of four with Milli-Q water before being flowed into the liquid cell.

This time, gold nanorods stayed apart and did not assemble when exposed to the electron beam, just as one would expect from a less screened electrostatic repulsion. The plot of experimentally measured rod positions in Figure 2.6a shows that the size of the depleted zone increased significantly – gold nanorods are surrounded by large repulsive clouds, as indicated by yellow dotted circles in Figure 2.6b, preventing them from encountering each other at the close distances needed for assembly. Although the attractive interaction is still present, the energetic barrier for rods to approach within the range where it is dominant, around 10 nm based on our results shown in Figure 2.4, is too high even when the rods approach tip-to-tip. Their trajectories shown in Figure 2.6c illustrate that even when a pair of rods closely approach each other by the result of Brownian motion, they then simply repel each other so that their separation is increased. This observation provides further proof of the dominant role of electrostatic repulsion in determining the behavior of charged gold nanorods in our system.

Determining the structure of the electrical double layer and monitoring its conformational changes during an electrochemical process has been a long-standing challenge. To our knowledge, this result is the first direct experimental observation of electrical double layers surrounding charged colloidal nanoparticles in an aqueous environment. For pure water at pH 7, the Debye length is 960 nm but in practice this value is much smaller due to the presence of electrolytes. Thus, for charged microparticles in aqueous solution, the range of experimentally observed electrostatic repulsion is usually negligible compared to their particle size, making the analysis challenging. By utilizing liquid phase TEM to study nanoparticle dynamics, we have opened up possibilities for investigating the nature of fundamental nanoscale interactions that exist between colloidal particles which have not been realizable using conventional optical microscopy studies of charged microparticles in aqueous environments.

The vast majority of liquid phase TEM studies have relied on the perturbation of the electron beam to initiate the desired process. Nevertheless, the nature of the perturbation on the system under study is poorly understood and hard to generalize for other systems. The interactions of the electron beam with the specimen have mostly been regarded as being undesirably complicated and difficult to control. Because of this, it is often challenging to predict the outcome of liquid phase TEM experiments. We show that

by understanding the nature of nanoscale interactions involved, we are able to circumvent the electron beam effects to retrieve the condition of colloidally stable gold nanorods under *in situ* electron beam irradiation. By going to extremely low ionic strengths, we were able to reproduce the behavior of electrostatically stabilized gold nanorods that is observed outside of the electron microscope. In other words, through our highly quantitative measurement and interpretation, the knowledge gained from *in situ* liquid phase TEM observations can be transferred to understand experiments in the wet lab, which, for this specific case, is correlated via adjustment of the ionic strength to increase the long-range electrostatic repulsion. Our observation of charged gold nanorods in solution that are mobile but yet stable toward aggregation is one of the few examples where the electron beam hasn't fundamentally changed the system under study.

2.8 Side-to-side assembly at a higher ionic strength

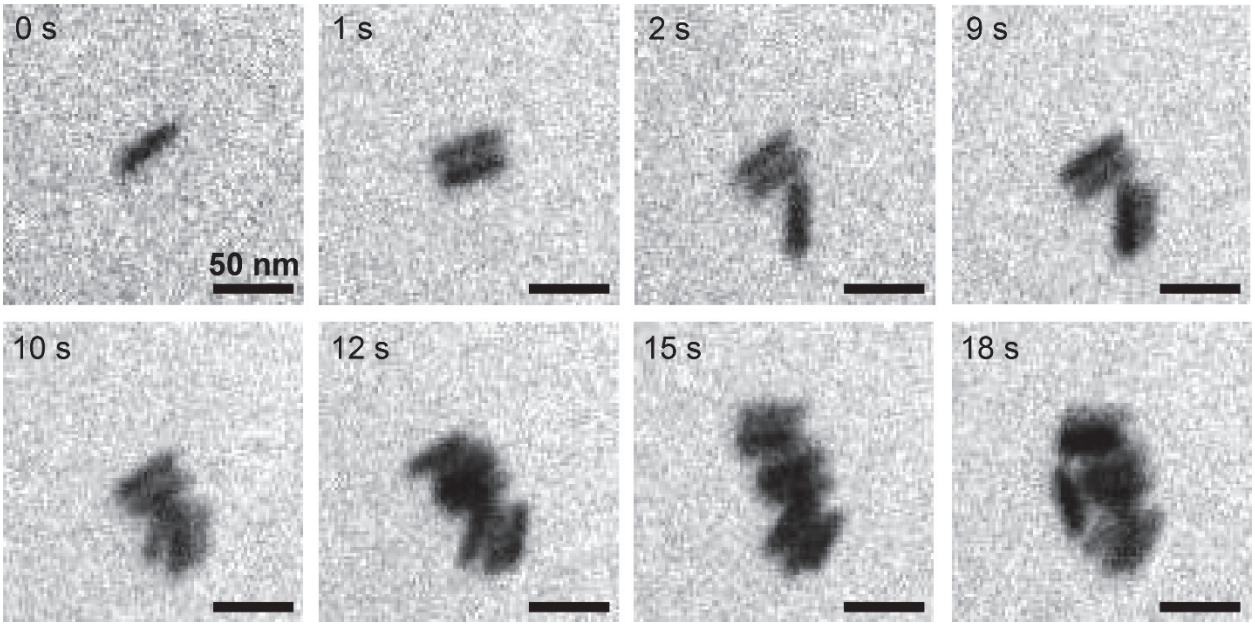

Figure 2.7 Tip-selectivity for rod attachment lost at high ionic strength. Time series of TEM images showing gold nanorod assembly at a higher ionic strength.

As a final test to confirm that long-range electrostatic repulsion and short-range attractive interaction are responsible for the behavior of gold nanorod assembly, we decided to observe how rods interact at high ionic strength. Sodium phosphate was added such that its concentration was 0.2 M in the final solution. When imaged under these conditions, the rods undergo electron beam-induced assembly with no tip-selectivity and actually appear to exhibit side-selectivity (Figure 2.7). The assembled structures are much denser than the tip-assembled chain-like structures shown in Figure 2.2b. This is still consistent with our proposed mechanism. Because of the increased ionic strength of the solution, electrostatic repulsion between the charged nanorods are effectively screened for all orientations. The difference in the energetic barrier that must be overcome, before rods can approach close enough for attachment, between tip-to-tip

approach and tip-to-side or side-to-side approaches is no longer significant. Thus the energetically favorable route for rod assembly is no longer determined by electrostatic repulsion, which was previously responsible for reorientation of the approaching rod, and so the tip-selectivity is lost. Tendency to form dense structures rather than more open fractal networks could be due to alignment of approaching rods at very short distances as a result of the strong short-range van der Waals attractive forces.

We have demonstrated our control over ionic strength as the experimental parameter that we can manipulate in a predictable manner to observe different behaviors of charged gold nanorods. After observing tip-selective assembly of charged gold nanorods at an intermediate ionic strength, we were able to identify the presence of long-range electrostatic repulsion that led to this selectivity by analyzing the rod trajectories and extracting their interaction potential profile. We then proceeded to corroborate our proposed mechanism by demonstrating that when we lowered the ionic strength, we created the condition for non-assembly due to stronger long-range electrostatic repulsion. When we increased the ionic strength, we observed side-selective assembly due to the effective screening of electrostatic repulsion. Such a high level control that enabled us to observe a wide range of behaviors in a predictable way for a given system by changing the ionic strength makes us optimistic about the future prospects of liquid phase TEM. Currently, the biggest criticism of liquid phase TEM is that the dynamics of the observed processes are heavily influenced by the electron beam and so the results of such studies are not directly relevant to experiments that are carried out under standard conditions in the wet lab. However, we have shown that by varying a single experimental parameter that is not total electron dose or electron dose rate, we can reproduce a range of behavior that can be correlated with observations made in the wet lab.

2.9 Conclusions

We demonstrated a generalizable strategy to use the relative trajectories of pairs and groups of nanocrystals, and potentially other nanoscale objects, moving in solution which can now be obtained by *in situ* liquid phase TEM to determine the interaction potentials between nanocrystals. Such nanoscale interactions are crucial for collective behaviors and applications of synthetic nanocrystals and natural biomolecules, but have been very challenging to measure *in situ* at nanometer or subnanometer resolution. Here, we used liquid phase TEM to extract the mathematical form of the interaction potential between nanocrystals from their sampled trajectories. We showed the power of this approach to reveal unanticipated features of nanocrystal-nanocrystal interactions by examining the anisotropic interaction potential between charged gold nanorods; they assembled in a tip-to-tip fashion in the liquid phase, in contrast to the well-known side-by-side packing arrangements commonly observed for drying-mediated assembly. These observations were explained by a long-range and highly anisotropic electrostatic repulsion that leads to the tip-selective attachment. This was corroborated by the fact that charged gold nanorods stayed unassembled at a lower ionic strength, since the electrostatic repulsion was even longer-ranged and the energetic barrier was too high for attachment. Our study not only provides a mechanistic understanding of the process by which metallic nanocrystals assemble, but also demonstrates a method that can

potentially quantify and elucidate a broad range of nanoscale interactions relevant to nanotechnology and biophysics.

Liquid phase TEM can be used to quantitatively examine the fundamental forces that govern how anisotropic colloidal nanocrystals interact with each other in their native liquid environment without *a priori* knowledge. From our study, we have learned that the ionic strength is a key parameter that will determine whether charged nanorods assemble tip-to-tip or side-by-side. This arises because at certain ionic strengths the electrostatic repulsion is minimized when the rods are oriented tip-to-tip, whereas at a higher ionic strength it is sufficiently screened and so the nanorods are effectively uncharged, meaning that they only experience short-ranged attractions and thus form into random aggregates without any selectivity. We note that while the observation of ionic strength dependence and screening length is consistent with simple models, studies of the assembly process at high ionic strength are still valuable for testing models of concentrated electrolytes which are still computationally very challenging. We see the real power of the *in situ* pairwise and higher order trajectory sampling method being its generalizable ability to correlate spatially the interaction potential profile with the shape/surface chemistry of other nanoscale systems involving more intricate yet crucial nanoscale interactions.

We anticipate that the versatile method we have demonstrated for quantifying interactions between charged gold nanorods to be readily extended to other systems. The most obvious follow-up study would be to repeat the analysis for other charged anisotropic gold nanoparticles including triangular nanoprisms and nanocubes. This would still be worthwhile for investigating the effect of anisotropic shapes on interparticle interactions. For microparticles, the number of available anisotropic shapes is very limited and so it has been difficult to carry out a systematic study of the effect of particle shape. Perhaps a creative combination of different building blocks may give rise to surprising assemblies through tip-selective attachment alone. An interesting future work would be to study the behavior of these anisotropic nanoparticles at a much higher particle concentration. Because of the anisotropy of building blocks, liquid crystalline behavior should emerge if a critical concentration can be reached.[119–121] Although electrostatic interactions were studied here, other interparticle interactions such as magnetic and depletion forces may also be probed in the future. The behavior of ferromagnetic nanoparticles near the Curie temperature could be investigated with *in situ* heating in liquid. If future developments allow application of a magnetic field during liquid phase TEM imaging, study of how superparamagnetic nanoparticles behave in solution would be possible. Study of depletion interactions could be investigated with sterically stabilized nanoparticles that can be assembled reversibly. This could be done via controlling the magnitude of the depletion interaction by changing the depletant concentration by liquid flow or by varying the temperature with *in situ* heating. Anisotropic interactions that result from heterogeneous surface functionalization, rather than particle shape, may also be studied using patchy nanoparticles. With the recent revolutionary advances in fast detector technology for TEM,[122] it should be feasible in the near future to carry out a thorough investigation, starting with simple spherical nanoparticles, to accurately plot how the profile of pairwise interaction potential depends on experimental parameters. Extension of our work with better spatial and temporal resolutions may provide insight into the range and magnitude of van der Waals forces for nanoparticles which were beyond the

capabilities of our instrumentation. This would provide valuable experimental data that is currently lacking for theoretical modeling of nanoscale interactions. Advances in this direction is critical if we are to move on from relying on the models developed for microparticles to formulating new theories to accurately describe nanoparticle interactions.

2.10 Materials and methods

Materials

Sodium oleate (> 97 %), CTAB (> 98 %), and CTAC (> 95 %) were purchased from TCI America. Hydrogen tetrachloroaurate trihydrate ($HAuCl_4 \cdot 3H_2O$, > 95 %) was purchased from Acros Organics. Silver nitrate ($AgNO_3$, > 99 %), sodium borohydride ($NaBH_4$, 99.99 %) were purchased from Sigma Aldrich. L-ascorbic acid (> 99 %) and hydrochloric acid (HCl, ≥ 36.5 %, 12.1 M) were purchased from Alfa Aesar. All chemicals were used as received. Milli-Q water (18.2 MΩ·cm) was used in all the experiments. All glassware was cleaned using freshly prepared aqua regia (HCl and HNO_3 mixed in a 3:1 volume ratio) followed by rinsing with copious amount of Milli-Q water.

TEM imaging

All TEM images and movies were obtained on Tecnai G2 20 S-TWIN TEM equipped with a Gatan Orius SC200 CCD camera. The acceleration voltage was 200 kV and the beam current density used for video collection was 61.7 and 17.3 electrons/($Å^2 \cdot s$) for assembly and non-assembly conditions, respectively. The electron dosage was calculated from the total pixel intensity using the conversion ratio of 10 counts in the CCD camera being equivalent to 1 electron. Lower beam intensities were used to minimize etching for gold nanorod solutions with lower ionic strengths where there are no reducing agents present to counteract the electron beam induced etching. Frame rates used for video collection were 3.25 and 4.89 fps.

Chapter 3

Investigating the Role of Graphene in Mitigating Radiation-Induced Damage

Adapted with permission from: H. Cho, M. R. Jones, S. C. Nguyen, M. R. Hauwiller, A. Zettl, and A. P. Alivisatos, “The Use of Graphene and Its Derivatives for Liquid Phase Transmission Electron Microscopy of Radiation-Sensitive Specimens” *Nano Letters* **2017**, *17*, 414–420. DOI: 10.1021/acs.nanolett.6b04383.

3.1 Background

At first sight, the ability of liquid phase TEM to directly visualize nanoscale matter in an aqueous environment should make it ideal for studying single particle dynamics of biological specimens, as long as the specimen in question is labeled with nanoparticles for improved contrast. Direct imaging may also become feasible in the future if phase contrast enhancement approaches for electron microscopy advance significantly. Although silicon nitride liquid cells have been used to image biological samples in hydrated environments,[63,123–125] their application to study biomolecules that are highly sensitive to radiation damage has been limited.[58,126–128] The key bottleneck has been the damaging effects of electron beam irradiation. In addition to the direct ionization damage resulting from interactions between the energetic electrons and the specimen itself,[52] the electron beam also induces radiolysis of surrounding water molecules which in turn produces highly reactive species, including hydroxyl radicals, which are damaging to biological matter.[129–135]

Previous studies with bacteria,[136] small DNA-AuNP conjugates,[104,137] proteins,[138] viruses,[139] and cells[139] using graphene liquid cells have shown that it is possible to image graphene-encapsulated hydrated biological samples for several minutes without visible structural damage. It has been speculated that graphene’s outstanding electrical and thermal conductivities may be responsible for reducing radiation damage to the encapsulated specimen, based on previous studies involving dry samples where local electrostatic charging and heating play important roles.[140–142] However, extrapolation of such conclusions to explain the phenomena in liquid phase TEM is not fully justified as they do not account for the considerable damaging effects that reactive radical species are known to cause. Furthermore, there has not yet been a comparative study of the specimen stability in both graphene and silicon nitride liquid cells to examine the degree of protection. If we can elucidate the origin of the observed protective ability of graphene liquid cells, it is conceivable that we may be able to apply this mechanism to the silicon nitride liquid cell studies where radiation damage has been more problematic.

Here, we utilize DNA-AuNP superlattices in aqueous solution as a model system to compare the stability of DNA, which is known to be highly susceptible to radiation damage,[129–135] during liquid phase TEM imaging in different liquid cell configurations. Lattice parameters and crystal symmetry of DNA-AuNP superlattices are dictated by the sequence-programmable DNA hybridization interactions occurring between neighboring

particles.[27,28,30] The direct observation and preservation of DNA-mediated long-range ordering of AuNPs, used here as high contrast markers, would demonstrate the structural stability of interparticle oligonucleotide linkages. Aside from the loss of global long-range order, structural damage could also manifest itself more locally in the form of DNA strand breaks,[129,131,134] which would result in dissociation of assembled AuNPs. Hence it is possible that the use of DNA-AuNP superlattices as a probe could provide more information about the liquid cell environment under irradiation than small DNA-AuNP conjugate systems. The fact that DNA-AuNP superlattices are composed of DNA-AuNPs uniformly coated at their surfaces, with approximately a hundred DNA strands per particle,[143] should mean that they should be much more stable than small DNA-AuNP conjugate systems where AuNPs are connected to each other via single duplex strands. This stability is important considering that DNA is highly sensitive to radiation damage.

3.2 Preparation of DNA-AuNP superlattices and their SAXS characterization

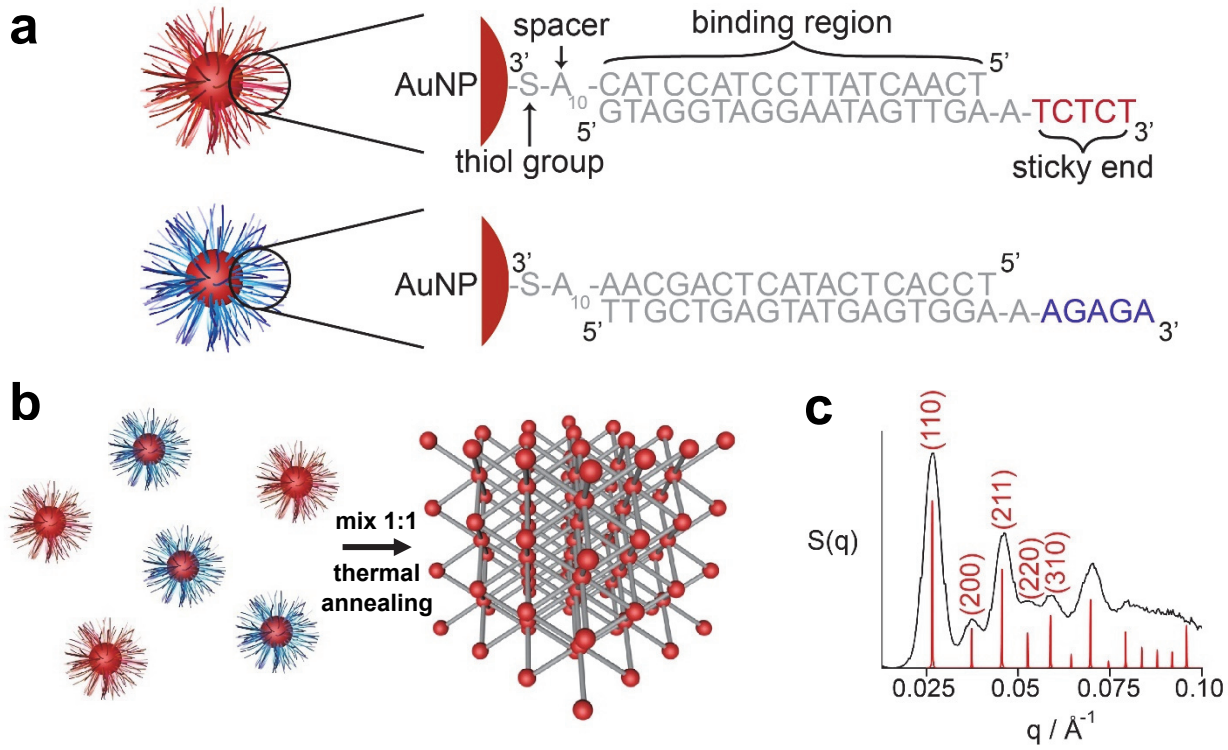

Figure 3.1 Synthesis and characterization of BCC DNA-AuNP superlattices. (a) Schematic showing the DNA sequences of the DNA-AuNPs used in this study. Note the complementarity of red and blue sticky ends. (b) Self-assembly of DNA-AuNPs into a BCC DNA-AuNP superlattice. (c) SAXS characterization of BCC DNA-AuNP superlattices in solution. The black trace is the experimentally obtained scattering pattern and the red peaks represent the theoretical scattering pattern for a BCC crystal lattice.

We chose to work with DNA-AuNP superlattices with BCC crystal symmetry. While cubic and hexagonal close-packed arrangements represent the densest packing of

spheres of identical size and nanoparticles are known to form these structures in the presence of isotropic and nonspecific interparticle forces,[7,144] a BCC arrangement is in general not observed under thermodynamic conditions. Therefore, observation of BCC DNA-AuNP superlattices using liquid phase TEM would be indicative of intact DNA hybridization-mediated assembly whereas close-packed structures may have resulted from unintentional particle aggregation or drying-mediated assembly. The BCC structure was selected above other non-close-packed structures because it is simple to synthesize while its relatively low packing fraction of 68 % (cf. 74 % for FCC) should allow for easier imaging in the transmission mode.

DNA linker sequences used in this work followed a design which has previously been shown to favor the assembly of particles into a BCC crystal structure; two sets of DNA functionalized AuNPs were separately prepared with linkers that contain complementary (but not self-complementary) sticky ends as shown in Figure 3.1a.[27] Red sticky ends can only bind to their blue counterparts, meaning that a DNA-AuNP with red sticky ends will only be surrounded by DNA-AuNPs with blue sticky ends and vice versa. The BCC arrangement is thermodynamically favored as this maximizes the number of nearest neighbors with complementary sticky ends.[27] The design concept behind the rest of the oligonucleotide sequence have been developed through careful optimization by Mirkin *et al*. The binding region, or flexor, is a DNA duplex that imparts rigidity which has been proven to be necessary for preserving the overall spherical shape of DNA-AuNPs while localizing interparticle binding to the peripheral region for better control of sticky end interactions.[145] The spacer region imbues partial conformational flexibility to the linker which has been shown to be important for achieving a high degree of crystallinity.[146] The non-binding adenosine located between the binding region and the sticky end also provides the necessary flexibility for crystallization.[27] The use of thiol groups to attach DNA to the AuNP surface exploits the strong Au-S bond for ease of functionalization.

To prepare BCC DNA-AuNP superlattices, we followed experimental procedures reported in the literature.[27,29,147] Briefly, thiolated oligonucleotides were treated with 100 mM dithiothreitol followed by purification using size exclusion chromatography. They were then added to a solution of citrate-capped 10 nm spherical AuNPs in the ratio of 3 nmol oligonucleotides per mL of AuNPs and incubated for 30 min. Then, 1 % sodium dodecyl sulfate (SDS) and 1M phosphate buffer at pH 8 (made using NaH_2PO_4 and Na_2HPO_4) were added followed by a slow stepwise addition of 2 M NaCl to give final concentrations of 0.5 M NaCl, 0.01 % SDS, and 10 mM phosphate buffer, after which the solution was allowed to sit overnight at 40 °C to maximize the DNA loading density. DNA functionalized AuNPs were then purified by three rounds of centrifugation and resuspension in 0.01 % SDS, with the final resuspension being carried out in a solution containing 0.5 M NaCl, 10 mM phosphate buffer, and 0.01 % SDS. Appropriate DNA linkers were then added and solutions were annealed at 50 °C for 30 min and then allowed to cool slowly to encourage hybridization of linkers to AuNPs. Amorphous DNA-AuNP superlattices are initially formed when these solutions are mixed in a 1:1 particle ratio at room temperature, accompanied by a color change of the solution from red to blue/black, but crystallinity is obtained after annealing at 42-44 °C for several hours (Figure 3.1b). Small-angle X-ray scattering (SAXS) was used to characterize the structure of prepared DNA-AuNP superlattices in solution and the obtained scattering pattern shown in Figure 3.1c confirmed that ordering is BCC with the separation of 28.7 nm between the centers of two nearest neighboring AuNPs.

3.3 Observation of stable DNA-AuNP superlattices using graphene liquid cells

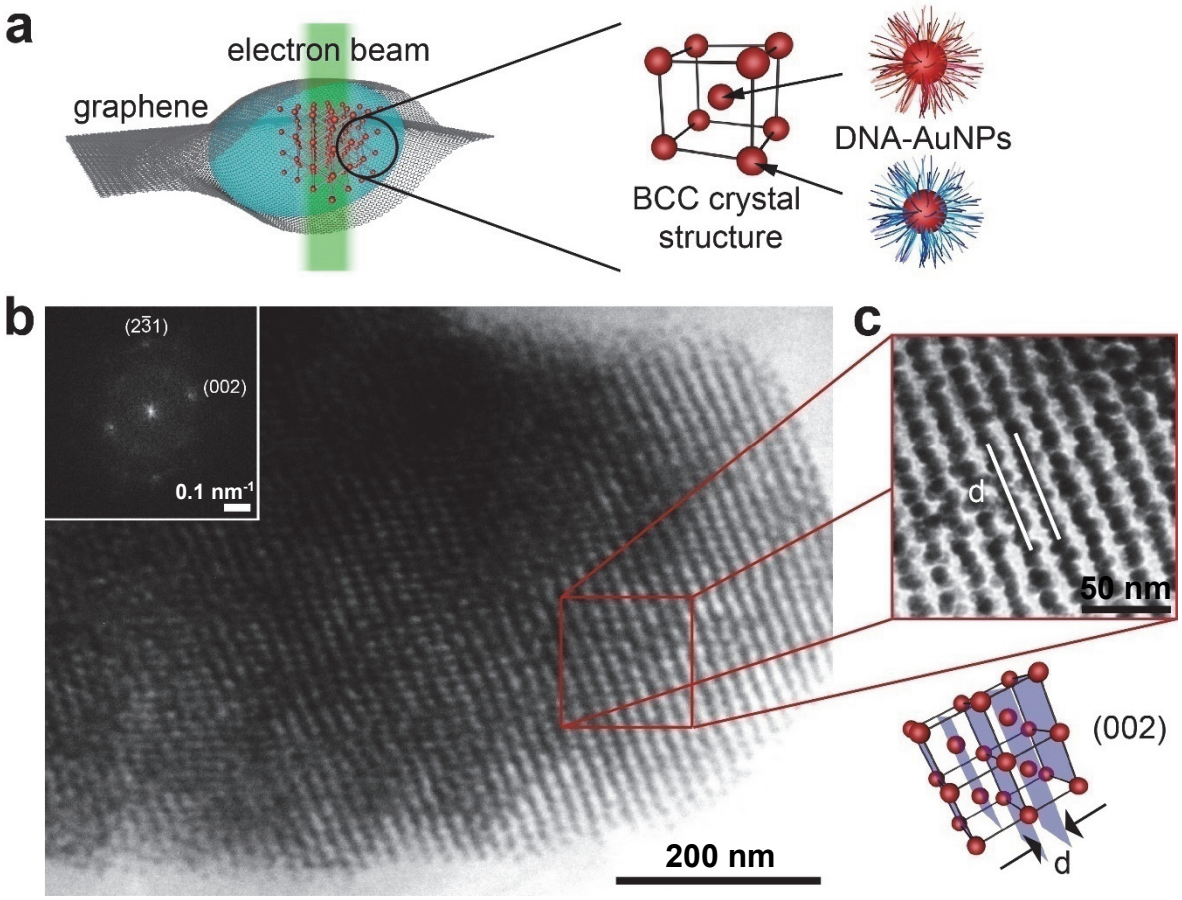

Figure 3.2 Stable DNA-AuNP superlattices imaged in their native aqueous environment using graphene liquid cells. (a) Schematic illustration showing encapsulation of BCC DNA-AuNP superlattices in aqueous solution using a graphene liquid cell. (b) A representative TEM image of DNA-AuNP superlattices taken using graphene liquid cell TEM. The inset shows the corresponding FFT image which matches the diffraction pattern of a BCC crystal with the [320] zone axis. (c) Higher magnification TEM image showing the ordered arrangement of AuNP cores. The lattice spacing corresponds to (002) planes in a BCC crystal structure, depicted schematically below.

We first used graphene liquid cells to image DNA-AuNP superlattices in their native aqueous solution containing NaCl and phosphate buffer (Figure 3.2a). Graphene liquid cells were prepared by trapping aliquots of the sample between pairs of graphene-coated gold TEM grids based on the method reported in the literature.[44] Gold TEM grids were coated with graphene by first placing the TEM grids on top of single/double layer graphene on copper foil, such that the Quantifoil film was in direct contact with the graphene surface. A few drops of isopropanol were then added until the gold TEM grids were completely immersed and allowed to evaporate in air, resulting in adhesion of graphene to the gold TEM grids. The copper foil was then floated on 50 mg mL^{-1} sodium persulfate solution and left overnight to ensure that all the copper had been etched away.

Thus prepared graphene-coated gold TEM grids were washed with fresh Milli-Q water three times and left to dry in air. A graphene liquid cell was made by sandwiching 0.5 μL of the DNA-AuNP superlattice solution between two graphene-coated gold TEM grids. The DNA-AuNP superlattice solution used had been redispersed such that the final NaCl concentration was 0.15 M (to minimize salt precipitation inside a liquid pocket) and vortexed just prior to encapsulation as the superlattices sedimented over time. When single/double layer graphene was replaced with multilayer (3-5 layers) graphene, it was possible to encapsulate larger amounts of liquid, probably due to decreased liquid leakage through defects in the graphene structure when several layers of graphene are stacked together.[139] However, trapping of larger amounts of liquid also resulted in more vigorous bubble formation. Comparable results were obtained when graphene liquid cells were prepared with commercially available graphene-coated copper TEM grids, which simply replaced graphene-coated gold TEM grids in the procedure outlined above.

Using graphene liquid cell TEM, we were able to image DNA-AuNP superlattices that exhibited long-range periodic ordering of AuNPs with clearly visible lattice spacings (Figure 3.2b). Analysis of the corresponding fast Fourier transform (FFT) image (the inset in Figure 3.2b) shows that the diffraction pattern belongs to that of a BCC crystal with the [320] zone axis. The lattice spacing between (002) planes is 16.5 nm, which is consistent with the value of 16.6 nm predicted from the SAXS data. Figure 3.2c shows a higher magnification image where individual AuNPs in the ordered arrays can be distinguished. Under typical imaging conditions, with electron dose rates ranging from 10 to 250 $e^-/(Å^2 \cdot s)$ depending on the magnification, DNA-AuNP superlattices did not undergo significant structural rearrangements for several minutes and appeared to be stable inside the liquid pockets. Because BCC ordering of AuNPs is only possible through programmed DNA hybridization interactions, we can deduce that most of the oligonucleotide linkages present in DNA-AuNP superlattices retain their structural stability during imaging.

Assignment of the diffraction pattern was done in the following way. The lattice spacing in Figures 3.2b and 3.2c was measured to be 16.5 nm. Since the unit cell length was 28.7 nm from our previous SAXS experiment, this confirmed that we are looking at {200} planes (for a BCC crystal, allowed Bragg reflections correspond to {110}, {200}, {211}, {220}, etc.). Thus one of the two vectors that are responsible for the elongated hexagonal arrangement of diffraction spots (the inset in Figure 3.2b) corresponds to {200}. Measuring the ratio of the lengths of the two vectors and the angle between them narrowed down the possibilities. As a starting point, the shorter of the two was assigned to be (200) which meant that the other vector must satisfy the conditions of $h^2+k^2+l^2 \sim 12$ and $\theta \sim 75$ °. Because the diffraction spots were not very sharp, we had to allow for the error in our measurements of vector lengths and angle. Thus, we found several combinations of h, k, and l that satisfied these conditions, namely {130}, {131}, and {123}. We then proceeded to eliminate the number of options by reproducing our BCC structure using VESTA software and generating views of the lattice planes with the zone axis set to be normal to the plane of the two vectors (Figure A2). After this comparison, we only had to decide between {131} and {123}. We then generated their corresponding FFT images. Since {131} gave a regular hexagonal diffraction pattern, it could be ruled out. We then confirmed that the generated diffraction pattern for vectors (200) and (123) viewed along [320] matched our experimentally observed elongated hexagonal pattern (Figure A3). By looking up the table for indexing diffraction patterns, we were able to

conclude that our diffraction pattern belongs to that of a BCC crystal with the [320] zone axis and diffraction peaks corresponding to vectors (002) and (2-31).[148] This procedure for identifying the diffraction pattern was repeated for other FFT images in this work.

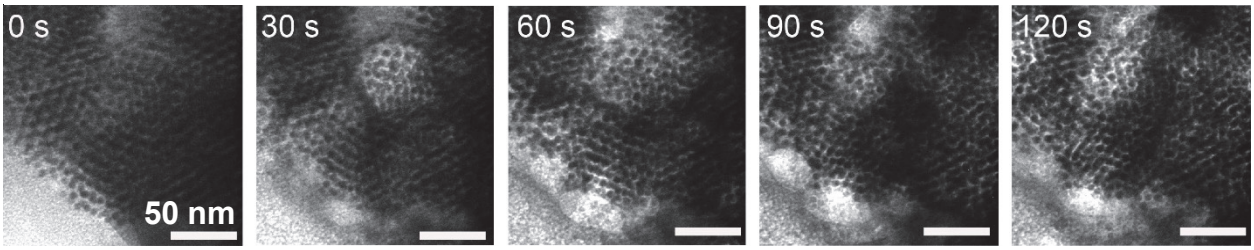

Figure 3.3 Electron beam-induced disordering of DNA-AuNP superlattices. Time series of TEM images after a focused electron beam caused bubble generation that resulted in the destruction of long-range order in DNA-AuNP superlattices.

When the electron beam was focused, such that the electron dose rate was increased by approximately one order of magnitude, the periodic arrangement of AuNPs became disordered by convection due to vigorous bubble formation in the liquid pockets before drying out completely (Figure 3.3). For the observed disordering of AuNPs at high electron beam intensities, it is difficult to decouple the effects of DNA damage from bubble-induced convection. This prevented efforts to quantitatively analyze the kinetics of DNA damage by tracking the intensity of spots in the FFT image that reflect the extent of long-range BCC ordering.

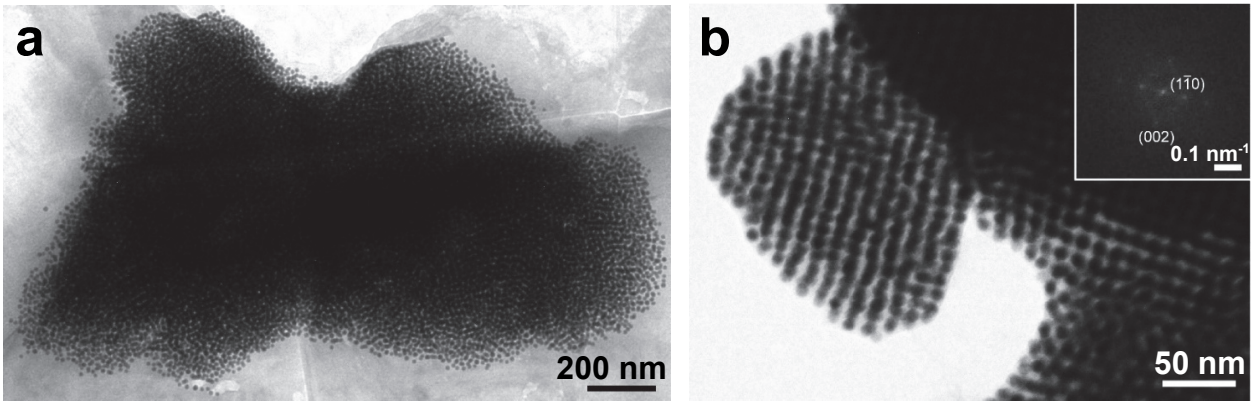

Figure 3.4 Dehydrated DNA-AuNP superlattices that were not successfully encapsulated in liquid. (a) A representative TEM image of dry and disordered DNA-AuNP superlattices. (b) A representative TEM image of dehydrated but BCC ordered DNA-AuNP superlattices. The inset shows the corresponding FFT image which matches the diffraction pattern of a BCC crystal with the [110] zone axis.

In dry regions of graphene liquid cell samples where liquid was not successfully trapped, we only observed collapsed DNA-AuNP superlattices with neither long-range

order nor the expected interparticle spacing. In Figure 3.4a, the original BCC structure has collapsed and there is no visible long-range order. Disordered superlattices were observed in nearly all of the dry regions of a graphene liquid cell. Figure 3.4b shows dehydrated but still ordered DNA-AuNP superlattices that exhibit smaller than expected interparticle spacing, with a contracted lattice constant of 17.5 nm instead of 33.1 nm, as a result of DNA collapse upon drying. The corresponding FFT image (the inset in Figure 3.4b) matches the diffraction pattern of a BCC crystal with the [110] zone axis. Dehydrated but crystalline DNA-AuNP superlattices were only observed in a small minority of samples prepared, presumably because the drying conditions need to be carefully controlled to reproducibly maintain the crystalline order. Preservation of solution phase lattice symmetry of DNA-AuNP superlattices after dehydration has been reported in the literature.[149] The lack of liquid was confirmed by the absence of any bubble generation and AuNP motion when the intensity of the beam was increased.

Our demonstration of imaging DNA-AuNP superlattices represents the first time that these large and ordered DNA-assembled structures have been directly visualized in their native saline solution. Until now, structural analysis of these structures using TEM have been carried out by first transferring them to the solid state. Typically, they are embedded in polymer resin or silica before being ultramicrotomed into thin samples.[150] More recently, cryo-electron microscopy (cryo-EM) has been used to image these structures by embedding them in vitreous ice.[151] Although these methods allow structural characterization in their static state with single particle resolution, one of the advantages of using DNA to assemble nanoparticles is that the resulting structure can be altered in a predictable way. Liquid phase TEM allows these structures to be imaged in solution state and so opens up opportunities for visualizing the dynamics of these reconfigurable structures as they respond to a controlled stimulus.

Our observation of graphene-encapsulated DNA-AuNP superlattices that are structurally stable during imaging is consistent with previous graphene liquid cell TEM studies of DNA-AuNP dimers, trimers, and pyramids where AuNPs were connected to each other via single DNA duplexes.[104,137] Even so, this result is still surprising since the high vulnerability of hydrated DNA toward ionizing radiation is well established.[129–135] Besides the direct ionization damage, electron beam-induced water radiolysis reactions give rise to the formation of highly reactive species, including hydrogen radicals, hydroxyl radicals, and hydrated electrons, that together create an extremely hostile environment for biological systems.[129–135] In particular, hydroxyl radicals are responsible for most of the radiation damage to DNA molecules in solution as they can readily undergo hydrogen atom abstraction from deoxyribose or electrophilic addition to C=C and C=N π-bonds in nucleobases.[129–131,135] Chemical modification of nucleobases weakens the hydrogen bonding interaction[131] while hydrogen abstraction from the sugar ring leads to cleavage of the sugar-phosphate backbone, resulting in DNA single-strand and double-strand breaks.[129,131,134] Although DNA crosslinking is also a known side effect of ionizing radiation, this is typically limited to intrastrand crosslinking and thus it is unlikely that DNA-AuNP superlattices are held together during imaging via interstrand crosslinked DNA.[152,153] In fact, the dissociation of AuNPs in small DNA-AuNP conjugates after prolonged exposure or at increased beam intensities was reported in the previous studies.[104,137] Without any *in situ* protection mechanisms, it is expected that DNA-AuNP superlattices would disintegrate into individual AuNPs.

3.4 Destabilization of DNA-AuNP superlattices in silicon nitride liquid cells

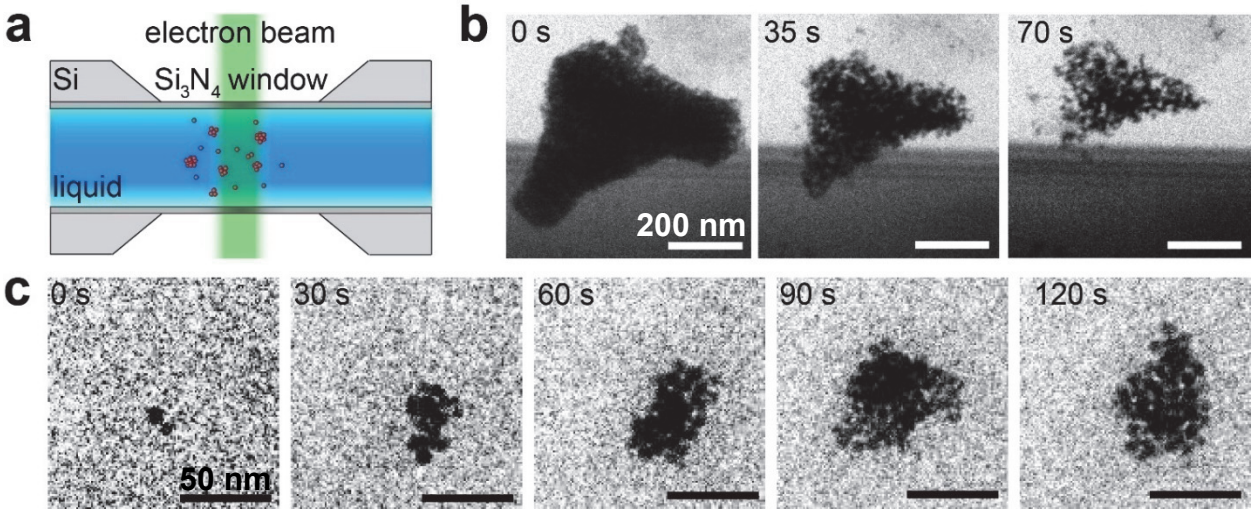

Figure 3.5 Destabilization of DNA-AuNP superlattices when imaged using silicon nitride liquid cell TEM. (a) Experimental setup for TEM imaging of DNA-AuNP superlattices using a silicon nitride liquid cell. (b) Time series of TEM images showing destabilization of oligonucleotide linkages in DNA-AuNP superlattices resulting in their dissociation into individual AuNPs upon electron beam illumination. (c) Time series of TEM images after electron beam-induced destabilization of DNA-AuNP superlattices showing subsequent aggregation of individual AuNPs into close-packed structures without the expected interparticle spacing or long-range order.

We next imaged DNA-AuNP superlattices using silicon nitride liquid cells under similar electron dose rates in order to directly compare the extent of radiation damage (Figure 3.5a). Silicon nitride liquid cells were prepared using a Poseidon 200 *in situ* liquid cell TEM flow holder and E-chips (Protochips) following a procedure reported in the literature.[154] Top (EPT-52W) and bottom (EPB-52DF) microchips, each with a 50 nm thick silicon nitride viewing window, were immersed in acetone to remove the protective resist coating and cleaned with methanol. They were then plasma-treated for further cleaning and to improve their surface hydrophilicity. The microchips were then assembled in a Poseidon 200 holder with 1 μL of the DNA-AuNP superlattices from the same stock solution. A crossed-window configuration of microchips resulted in a viewing window with dimensions of 20 μm × 20 μm.

Most strikingly, only an extremely small number of DNA-AuNP superlattices could be found in the viewing area compared to what was observed with graphene liquid cells. It has been reported that the silicon nitride surfaces can be negatively charged at pH values above 6 due to the deprotonation of silanol and silylamine groups.[48] We speculate that the highly negatively charged nature of DNA-AuNPs, which are in phosphate-buffered saline solution at pH 8, may be preventing their attachment to the silicon nitride windows, leading to infrequent detection. Of those that were found, we observed dissociation almost immediately upon electron beam illumination (Figure 3.5b). AuNPs were then seen to aggregate randomly at the silicon nitride window and etch over time

(Figure 3.5c). From these observations, we conclude that the DNA linkages are rapidly damaged, most likely as a result of hydroxyl radical attack, thereby causing the AuNPs to dissociate from the assembled structure and diffuse into the surrounding solution. The motion of individual AuNPs as they diffuse away is presumably too fast to be tracked with the temporal resolution of our camera as they are not slowed down by strong attachment to the silicon nitride windows. Random aggregation of AuNPs can be explained by the loss of electrostatic stabilization, previously imparted by the dense packing of negatively charged oligonucleotides, leading to decreased colloidal stability. The formation of densely packed aggregates lacking both long-range order and the expected interparticle spacing indicates that oligonucleotides are either no longer present at the surfaces of these AuNPs or severely damaged. There is no evidence to suggest that the aggregation of AuNPs is due to even partially DNA-mediated assembly. Etching of aggregated AuNPs is attributed to oxidative dissolution caused by the hydroxyl radicals.[56]

Even when the DNA-AuNP superlattices were not observed nearby, AuNPs were seen to attach to the window, followed by aggregation and etching. This is consistent with our assumption that pristine DNA-AuNPs do not strongly attach to the silicon nitride window and so DNA-AuNP superlattices, which are freely moving in the solution, are dissociating at some distance away from the window. Previous studies from the literature that looked at aggregation of charged AuNPs that were destabilized under irradiation reported formation of chain-like or low-dimensional fractal-like aggregates.[60,61] This discrepancy can be explained by considering the balance of long-range electrostatic repulsion and short- range van der Waals attraction for charged spherical particles.[155] When the former is dominant, particles would prefer to attach to the ends of a growing aggregate to minimize repulsive interactions. In our case, we expect the electrostatic repulsion to be relatively weak in comparison to the van der Waals attraction because of the charge screening effect in high ionic strength conditions. Thus, we see the formation of compact aggregates that maximize the van der Waals attractive interactions.

Our results from the silicon nitride liquid cell experiments are consistent with what would have been expected for DNA-AuNPs under electron beam irradiation in solution. Thus far, a study that investigates the stability of a specimen during TEM imaging in both graphene and silicon nitride liquid cells has been lacking and so it has not been possible to conclude with confidence that one technique offers better protection against radiation damage than the other. However, the fact that our comparative study of graphene and silicon nitride liquid cells yielded such different results for the same specimen exposed to similar TEM imaging conditions suggests that graphene windows indeed provide better protection for the specimen compared to their silicon nitride counterparts, as previously speculated in earlier reports of graphene liquid cell experiments with biological specimens.[104,136–139] Since our results with silicon nitride liquid cells are consistent with what would have been expected for DNA-AuNPs under electron beam irradiation in solution, we can reason that graphene provides protection rather than the alternative explanation that silicon nitride is damaging for the specimen. A thorough analysis of the mechanism behind graphene's ability to protect the specimen is very challenging using graphene liquid cells alone due to the lack of control over the liquid pocket positions, large variation in liquid pocket sizes, and the limited stability of the liquid pocket under electron beam irradiation. For further investigation, we must proceed by introducing a graphene surface into a silicon nitride liquid cell which acts as a well-defined platform.

3.5 Modification of the silicon nitride liquid cell interface with graphene

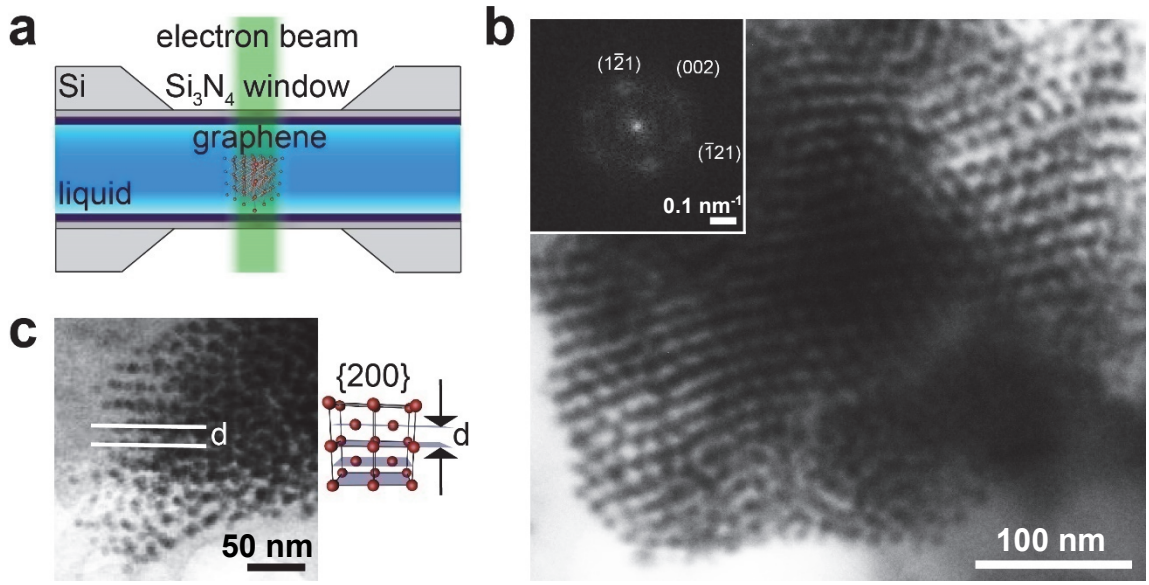

Figure 3.6 Stable DNA-AuNP superlattices imaged using graphene-coated silicon nitride liquid cells. (a) Experimental setup of graphene-coated silicon nitride liquid cell TEM. (b) TEM snapshot of DNA-AuNP superlattices at a lower magnification. The inset shows the corresponding FFT image which matches the diffraction pattern of a BCC crystal with the [210] zone axis. (c) TEM snapshot of DNA-AuNP superlattices. The lattice spacing indicated corresponds to the {200} planes in a BCC crystal structure as depicted schematically on the right.

To confirm the importance of graphene in providing protection against radiation damage in DNA-AuNP superlattices, a graphene surface was integrated with the silicon nitride liquid cell design (Figure 3.6a). Graphene-coated silicon nitride liquid cells were prepared using the PMMA-mediated transfer method reported in the literature.[156–159] PMMA solution was spin-coated onto multilayer graphene on copper foil at 2500 rpm for 1.5 min followed by annealing at 80 °C for 15 min. After being cut into small pieces (approximately 3 mm × 3 mm), the copper foil was etched overnight with 50 mg mL^{-1} sodium persulfate solution. PMMA-coated multilayer graphene was washed by transferring to fresh Milli-Q water three times using a glass slide that had been cleaned with methanol and treated with plasma. It was then transferred onto the microchips that had been cleaned using acetone, methanol, and plasma. Graphene-coated silicon nitride microchips were left to dry in air before undergoing a two-step annealing process (80 °C for 5 min followed by 130 °C for 20 min). They were then immersed in fresh acetone twice (each step lasting 30 min) to remove the PMMA and washed with methanol before being dried for use. Quality of graphene transfer was assessed from its Raman signature using a WITec alpha300 confocal Raman microscope equipped with a 488 nm excitation laser and an 1800 lines/mm grating while operating in 180 ° backscattering geometry. Incident power of less than 2 mW was used to avoid damage to the graphene via local heating.[160] A pair of graphene-coated microchips were assembled inside the Poseidon 200 holder.

Similar to the silicon nitride liquid cell setup, DNA-AuNP superlattices are encapsulated between two microchips, but now with graphene surfaces in contact with the solution. Employing graphene-coated silicon nitride liquid cells, we were able to observe DNA-AuNP superlattices with long-range order (Figures 3.6b and 3.6c), indicating that DNA linkages are structurally stable during imaging in the timescale of several minutes. The FFT image shown in the inset of Figure 3.6b corresponds to the diffraction pattern of a BCC crystal with the [210] zone axis. The lattice spacing indicated in Figure 3.6c is 16.3 nm, which is close to the expected value of 16.6 nm for the {200} planes. DNA-AuNP superlattices appeared to be strongly attached to the windows, which could be due to the binding of DNA to graphene driven by hydrophobic and π-π stacking interactions.[161] Dissociation, aggregation, and etching of DNA-AuNP superlattices that were seen in silicon nitride liquid cells were not observed despite the use of similar imaging conditions. These results point toward specific properties of graphene as being responsible for the observed differences in the DNA stability under irradiation.

It must be mentioned that the PMMA-mediated transfer of graphene leaves a very thin layer (subnanometer) of PMMA on the surface of graphene, among other possible contaminants from the Cu etching process, which can't be easily washed away.[162,163] Although polymer-free graphene transfer methods have been developed,[162–164] they are not yet as robust as the PMMA-mediated method. The presence of PMMA at the graphene surface would mean that the graphene-liquid interface depicted in Figure 3.6a may have been too idealized. On the other hand, PMMA residue is actually also present in silicon nitride liquid cells because the microchips are coated with PMMA for surface protection and so have to be washed before use. Thus we do not think it is likely that the presence of PMMA residue rather than graphene would be responsible for the qualitative differences we observed after coating the silicon nitride windows with graphene.

We also experienced difficulties with sealing when silicon nitride windows coated with graphene were used to encapsulate DNA-AuNP superlattices. Often, the sealing appeared to be poor, as indicated by salt precipitation that was visible by eye at the holder tip and by the large fluctuations in liquid thickness indicated by contrast variations in the same region over time. This was attributed to a small amount of liquid at the o-ring and microchip interface that dry out under vacuum to leave behind a salt precipitate which then lowers the quality of sealing. In such cases, the liquid cell was either reassembled with a different sample or the salt precipitate that formed on the outside was dissolved with a small amount of water. We tried to minimize this problem by reducing the NaCl concentration from 0.5 M to 0.15 M but this was not enough to solve the problem effectively. Further lowering of the NaCl concentration was not possible since DNA-AuNP superlattices are only stable at high salt concentrations where electrostatic repulsion between negatively charged phosphate backbone of DNA strands are screened. If the ionic strength were to be further lowered, then DNA-AuNP superlattices would dissociate into individual DNA-AuNPs. The hydrophobic nature of graphene surface after it has been exposed to air meant that the microchips were often not fully wetted and this may have been responsible for the poor sealing. To improve the wetting, the graphene-coated microchips were exposed to a very short period of plasma cleaning (a few seconds) to increase their surface hydrophilicity. The plasma cleaning step had to be kept as short as possible because it damages the graphene. Sealing problems meant that imaging a sample with good contrast and spatial resolution was challenging.

3.6 Role of graphene studied using correlative Raman spectroscopy and TEM

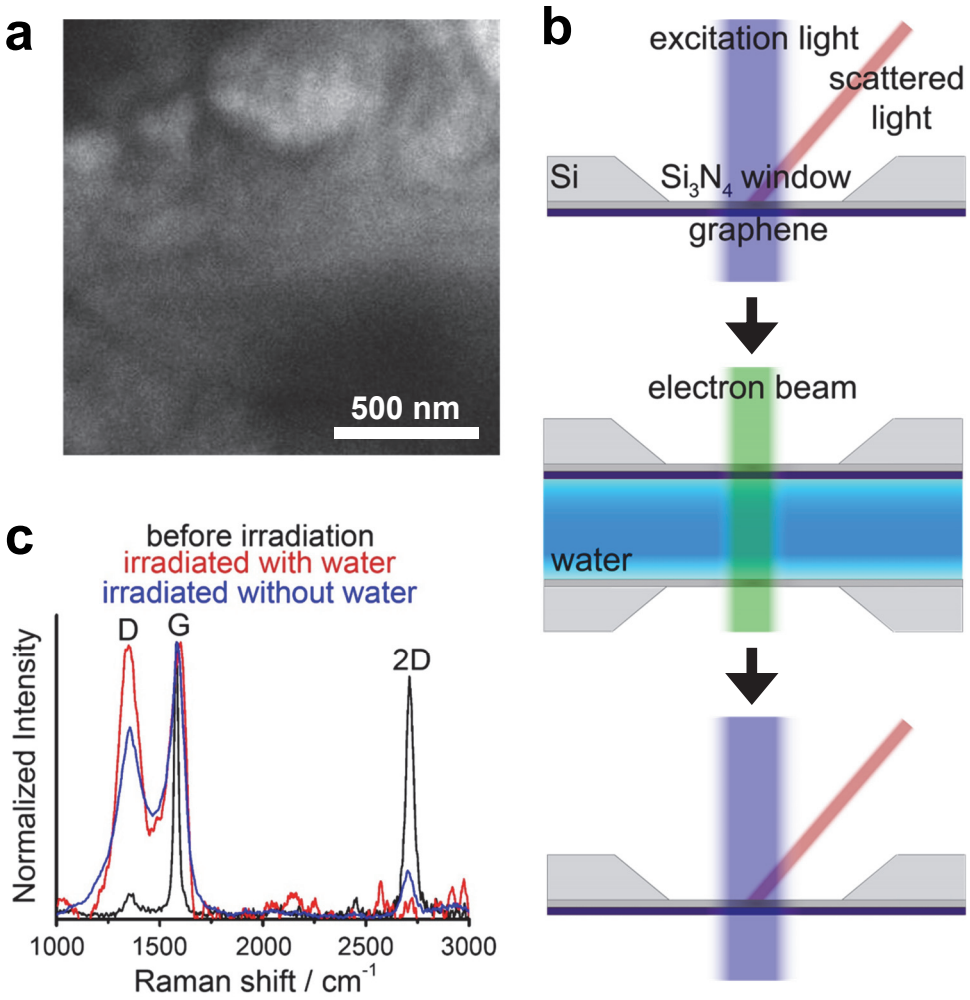

Figure 3.7 Correlative Raman spectroscopy and liquid phase TEM. (a) A typical snapshot of bubble formation at graphene/water interface under electron beam irradiation. (b) Schematic illustration of correlative Raman spectroscopy and liquid phase TEM. The same region of graphene was characterized with Raman spectroscopy before and after electron beam irradiation in water. (c) Effect of water radiolysis on graphene probed using Raman spectroscopy. Normalized Raman spectra (background-subtracted) for graphene before irradiation (black curve), graphene irradiated with water (red curve), and graphene irradiated without water (blue curve) are shown.

When using graphene-coated silicon nitride liquid cells, bubbles appeared to form at the liquid-window interface (Figure 3.7a) as inferred from the observation that bubbles and AuNPs were in the same focal plane. As in previous graphene liquid cell experiments, bubble formation resulted in disordering of DNA-AuNP superlattices, but disordered DNA-AuNP superlattices remained stable against dissociation, aggregation, and etching which suggests that disordering was caused by mechanical forces of bubble-induced convection rather than radiation damage. Observation of bubble formation was surprising in itself since at similar imaging conditions, it was not observed in silicon nitride liquid cells unless

the electron beam intensity was drastically increased. In silicon nitride liquid cell TEM experiments, bubble formation that is observed when an aqueous solution is exposed to a high dose rate has been attributed to the evolution of hydrogen gas as a byproduct of water radiolysis.[56] Based on these results, bubble formation that is often seen in graphene liquid cell experiments has been speculated to be of the same origin. Formation of bubbles that is observed only at the graphene surface, instead of occurring homogeneously in the solution, and at much lower doses than for silicon nitride liquid cell TEM experiments, strongly implies that graphene seems to be directly reacting with the products of water radiolysis. Contrary to the view held so far that graphene acts as a chemically inert window material,[44,104,165] our results suggest that this assumption is no longer valid.

To quantitatively assess the changes to graphene that occur during liquid phase TEM imaging, we carried out a correlative Raman spectroscopy and liquid phase TEM study of graphene before and after electron beam irradiation in water (Figure 3.7b). Raman spectroscopy is the most widely used technique for characterizing the graphene structure and a wealth of quantitative information can be extracted with high throughput from the analysis of peak shapes, positions, and intensities.[166] Graphene exhibits D, G, and 2D Raman peaks and by monitoring the spectral changes that occur during TEM imaging, we would be able to evaluate the influence of the electron beam on graphene in water. The D peak arises from the breathing modes of sp^2 carbon atoms in aromatic rings and is defect-activated.[167] The G peak originates from the bond stretching of all pairs of sp^2 carbon atoms.[167] The 2D peak is the D peak overtone, the second order of the D peak.[167] If graphene were to react with the water radiolysis products, we would expect to see an increase in the relative intensity of the D peak with respect to the G peak due to the formation of structural defects.[166] Additionally, the 2D peak is expected to broaden and decrease in intensity as graphene becomes more amorphous.[167]

An area of size 20 μm × 20 μm in the graphene-coated silicon nitride window was analyzed with Raman spectroscopy before and after exposure to a controlled electron dose in water. The beam intensity was set such that the electron dose rate was 2 $e^-/(Å^2 \cdot s)$ and 2.55 kx magnification was used throughout. At this beam intensity and magnification, the beam size was only slightly larger than the viewing area of the camera which has dimensions of 4.3 μm × 4.3 μm. Irradiation of graphene in water was carried out by encapsulating water using a graphene-coated top microchip paired with an uncoated bottom microchip. We chose to analyze only the top microchip as variations in the liquid thickness would influence the extent of electron beam intensity attenuation for the bottom microchip. The entire viewing window (20 μm × 20 μm in area) was irradiated by illuminating one spot for 3 min and then moving either horizontally or vertically by 4 μm using the goniometer. Hence, the total electron dose per area was around 360 $e^-/Å^2$. After TEM imaging, we analyzed the irradiated area of the graphene-coated top microchip with Raman spectroscopy. The area that was exposed to the electron beam was located using an optical microscope (part of the Raman instrumentation), with the knowledge that the viewing window lies at the center of the silicon nitride window that has dimensions of 550 μm × 20 μm. We carried out a control experiment by exposing graphene in another region of the same silicon nitride window to identical imaging conditions but in the dry state to assess the severity of knock-on damage in the absence of any water radiolysis products.[52] For this purpose, areas of 20 μm × 20 μm at the extreme left and right parts

of the silicon nitride window were selected for ease of identification and to rule out the possibility that products of water radiolysis from graphene irradiation in water could have reached the control regions by diffusion. Raman spectra in Figure 3.7c show that the changes in relative intensities of D, G, and 2D peaks are greater when graphene is irradiated in water, confirming that graphene is reacting with the products of water radiolysis. Delamination of graphene in regions that were irradiated in water was also observed with TEM and optical microscopy (Figure A4).

The leading hypothesis to explain graphene's ability to reduce radiation damage in liquid phase TEM has cited its excellent electrical and thermal properties.[104,136,137,139] But it has already been shown that electron beam-induced heating of the specimen is negligible in liquid cells where heat can be dissipated to the surrounding liquid,[45,56] so thermal conductivity does not appear to play a significant role. Electrostatic charging of the specimen and the windows by the ionizing electron beam[53] has been observed in previous silicon nitride liquid cell TEM studies.[59,168] Although it is plausible that electrically conducting graphene may help reduce electrostatic charging effects, it is unclear how electrical conductivity will counteract the detrimental effects of reactive radical species that are known to form in solution. Our correlative Raman spectroscopy and TEM study demonstrates that we can no longer regard graphene as a chemically inert material that simply imparts electrical conductivity to the silicon nitride window.

A more likely explanation is that graphene is acting as a radical scavenger. It has already been shown that radical scavengers, such as isopropanol and ascorbic acid, can be added to mitigate electron beam-induced galvanic replacement of AgNPs[101] and oxidative dissolution of gold nanorods,[169] respectively. Recent electron spin resonance spectroscopy and spectrophotometric studies have demonstrated that graphene, graphene oxide, and graphene quantum dots are all efficient hydroxyl radical scavengers.[170–173] It has been proposed that hydroxyl radicals react with graphene-based nanomaterials via electrophilic addition to conjugated C=C π-bonds or further oxidation of existing oxygen-containing functionalities.[170–172] Previous investigations of DNA stability against radiation damage in the presence of radical scavengers have shown that yields of DNA single-strand and double-strand breaks decreased as radical scavenger concentration was increased.[174–176] Thus, an alternative hypothesis for the observed stability of biological specimens in graphene and graphene-coated silicon nitride liquid cells is that the graphene surfaces are scavenging radicals from water radiolysis, thereby protecting adjacent DNA-AuNP superlattices. Bubble formation observed when graphene is imaged in water at low electron beam intensities is presumably due to evolution of gases that are the byproducts of graphene oxidation.

Integration of the graphene surface with the conventional silicon nitride liquid cell design yielded insights which were not attainable through a simple comparative study between graphene and silicon nitride liquid cells. Idealization of the graphene surface as a chemically inert imaging window for liquid phase TEM studies appears to have been a naive assumption. Instead, graphene undergoes a chemical reaction during liquid phase TEM imaging, probably with the reactive radical products of water radiolysis. Moreover, the observation that DNA-AuNP superlattices strongly attach to the graphene surface questions some of the interpretations of previous graphene liquid cell studies from the literature. Until now, it has been claimed that graphene, which was assumed to be an inert window material, should interact less strongly with the specimen than silicon nitride

windows. As a result, the concerted dynamics of small DNA-AuNP conjugate systems in graphene liquid cells has been described as free 3D motion rather than the quasi-2D motion seen in silicon nitride liquid cells while no credible explanation was given for the experimentally obtained diffusivities that were many orders of magnitude lower than the expected values.[104,137] Based on the results of our experiments, a more likely explanation appears to be that these nanoconjugate clusters were fixed at the graphene surface and their supposed motion was in fact the result of the graphene movement under irradiation.

3.7 Incorporation of graphene derivatives as radical scavengers

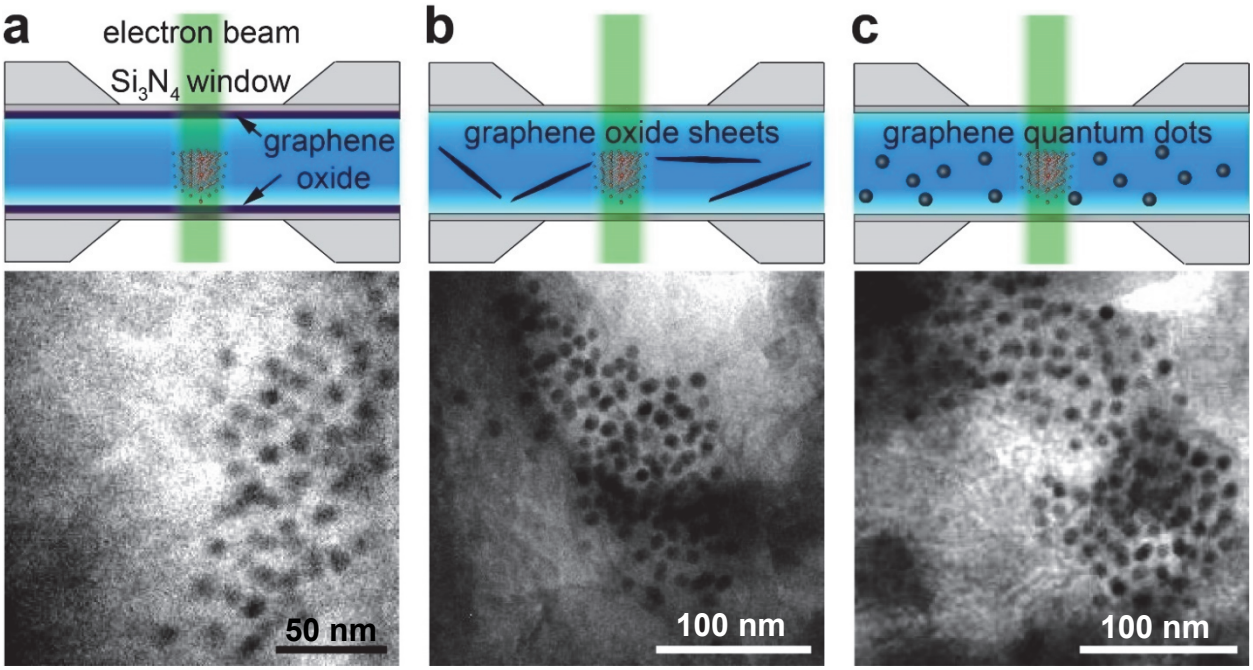

Figure 3.8 Imaging of DNA-AuNP superlattices using silicon nitride liquid cells with graphene derivatives added as radical scavengers. (a) Graphene oxide sheets drop-casted onto silicon nitride windows. (b) Graphene oxide sheets added to the solution. (c) Graphene quantum dots added to the solution.

If radical scavenging is the protection mechanism of graphene, then the protective effect should also be seen when radical scavenging graphene derivatives are present at the window or in the solution. Consequently, we set out to image DNA-AuNP superlattices using silicon nitride liquid cells with graphene oxide and graphene quantum dots, which are being explored for biosensing and biomedical applications,[161,177] as biocompatible radical scavengers. The three liquid cell configurations that we used were as follows: graphene oxide sheets drop-casted onto silicon nitride windows (Figure 3.8a), graphene oxide sheets added to the solution (Figure 3.8b), and graphene quantum dots added to the solution (Figure 3.8c). For graphene oxide-coated silicon nitride liquid cells, 2 µL of 1 mg mL^{-1} graphene oxide sheets in solution was pipetted onto the microchip window and allowed to dry in air. For silicon nitride liquid cell studies with graphene oxide sheets and graphene quantum dots added directly to the solution as hydroxyl radical scavengers,

concentrations of 2 and 1 mg mL^{-1} were used, respectively. Graphene oxide sheets and graphene quantum dots remained colloidally stable after being added to the DNA-AuNP superlattice solution. In all three cases, DNA-AuNP superlattices were stable against dissociation, aggregation, and etching. Since graphene oxide is an insulator,[178] we can now rule out the role of electrical conductivity in protecting the encapsulated specimen.

However, as noted previously with graphene and graphene-coated silicon nitride liquid cells, DNA-AuNP superlattices appear to be disordered by bubble formation. The greater amount of disordering observed in silicon nitride liquid cells with graphene-based radical scavengers compared to graphene liquid cells could be due to the greater volume of liquid being present, which would result in the creation of more hydroxyl radicals that can react and cause bubble formation. Although liquid thicknesses were not directly measured for graphene and silicon nitride liquid cells, we can make the following estimations. Since the DNA-AuNPs within a given pocket exhibited limited range of motion, the vertical dimensions of pockets in graphene liquid cells appeared to be similar to the heights of encapsulated DNA-AuNP superlattices that were imaged (typically around 100 nm based on the number of unit cells). For silicon nitride liquid cells, the lower bound is defined by the height of the 150 nm spacer used. However, bending of the window in high vacuum conditions can produce an actual height as large as 1 μm; any thicknesses greater than this would constrain the imaging capability of the TEM. It is also possible that the small dimensions of the liquid pockets present in graphene liquid cells could be exerting confinement effects on the DNA-AuNP superlattices, thereby restricting their movement and so minimizing the disordering. Use of multilayer rather than single/double layer graphene as the window material allowed encapsulation of more liquid,[139] but led to more vigorous bubble formation and thus faster disordering of DNA-AuNP superlattices. Regardless, we conclude that radical scavenging ability is the crucial parameter that explains the enhanced protection of the specimen against radiation damage in the graphene liquid cell compared to its silicon nitride counterpart.

3.8 Conclusions

We showed that stable DNA-AuNP superlattices can be imaged in their native saline environment when the liquid cell window material is graphene, but not when it is silicon nitride. In the latter case, initial dissociation of assembled AuNPs was followed by their random aggregation and etching. Using graphene-coated silicon nitride windows, we were able to replicate the observation of stable DNA-AuNP superlattices achieved with graphene liquid cells. We then carried out a correlative Raman spectroscopy and TEM study to quantitatively compare the effect of electron beam irradiation on graphene with and without the presence of water and found that graphene reacted with the products of water radiolysis. We attribute the protective effect of graphene to its ability to efficiently scavenge reactive radical species, especially hydroxyl radicals which are known to cause DNA strand breaks. We confirmed this by showing that stable DNA-AuNP superlattices can be imaged in silicon nitride liquid cells when graphene oxide and graphene quantum dots, which have also recently been reported as efficient radical scavengers, are added directly to the solution. We anticipate that our study will open up more opportunities for studying biological specimens using liquid phase TEM with the use of graphene and its derivatives as biocompatible radical scavengers to counteract the radiation damage.

Based on our study, we advocate the use of graphene liquid cells for studying radiation-sensitive biological specimens as they offer optimal image contrast and spatial resolution for a given electron dose, while the chemical properties of graphene provide protection against radiation damage. By adding water-soluble graphene derivatives directly to the solution, it may be possible to reduce the radiation damage even further, which could also lead to prolonged lifetime of the liquid pockets by retarding the formation of defects in the graphene windows. For graphene-coated silicon nitride liquid cells, the hydrophobicity of the window surfaces meant that microchips were often incompletely wetted, resulting in sealing problems. Thus, when using silicon nitride liquid cells, we recommend that hydrophilic graphene derivatives should be used both as additives to the solution and as coatings on the windows. The main benefit of using graphene and its derivatives is that they don't change the chemical environment that the specimen is placed in. Although they react with products of water radiolysis, they do not react with the specimen and don't influence parameters such as pH, ionic strength, solubility, etc. Even though the scope of this study has focused on the use of graphene and its derivatives, it is likely that alternative radical scavengers could produce a similar protective effect. Further investigation is needed to determine the most effective radical scavenger that should be used in future liquid phase TEM studies where minimal perturbation by the electron beam is desired. One possible way of doing this using liquid phase TEM would be to compare etching rates of nanoparticles undergoing oxidative dissolution by hydroxyl radicals generated from water radiolysis in the presence of different radical scavengers. The most effective radical scavenger would be the one that minimizes etching under identical imaging conditions. This could also be investigated in the wet lab by chemically generating hydroxyl radicals and tracking nanoparticle etching via spectroscopic methods such as UV-Vis spectroscopy, although it may be nontrivial to accurately reproduce the experimental conditions inside the liquid cell under electron beam irradiation. If damaging effects of highly reactive radical species generated from water radiolysis could be efficiently suppressed, it would enable liquid phase TEM to provide characterization capabilities that would complement X-ray crystallography, solution nuclear magnetic resonance spectroscopy, cryo-EM, and super-resolution fluorescence microscopy.

Ideally, unsupported one-atom thick graphene windows should be integrated with the existing microchip-based liquid cell platform to combine the high resolution imaging capability and protective ability of graphene liquid cells with technical capabilities that facilitate liquid flow, heating, and electrical biasing. Silicon nitride windows can't be made much thinner than several tens of nanometers without sacrificing their robustness, thus imposing limits on the attainable contrast and resolution. Despite the aforementioned advantages of using graphene windows, a major problem associated with them is that they are known to be damaged under electron beam irradiation. Since a silicon nitride liquid cell typically contains a volume of liquid which is several orders of magnitude greater than that contained in a typical graphene liquid cell, a rupture of the window could be fatal for highly sensitive detectors that may be present in the electron microscope. This would necessitate the imaging conditions to be set such that the electron beam-induced damage to graphene is minimized to prevent leakage through damaged regions of graphene. One possible solution could be to use multilayer graphene (around ten layers or more) that would be more stable than monolayer graphene while still being much thinner than silicon nitride windows.

3.9 Materials and methods

Materials

DL-dithiothreitol ($HSCH_2CH(OH)CH(OH)CH_2SH$, 99 %), sodium chloride (NaCl, 99.5 %), sodium phosphate monobasic (NaH_2PO_4, 99 %), sodium phosphate dibasic (Na_2HPO_4, 99 %), sodium dodecyl sulfate ($CH_3(CH_2)_{11}OSO_3Na$, 99 %), sodium persulfate ($Na_2S_2O_8$, 99 %), and isopropanol (99.5 %) were purchased from Sigma Aldrich. Acetone (99.5 %) and methanol (99.9 %) were purchased from Fisher Scientific. All oligonucleotides were purchased from Integrated DNA Technologies. PMMA (950 k, 4 % in anisole) was purchased from MicroChem. Graphene oxide sheets (10 mg mL^{-1} in water), graphene quantum dots (Green GQDs, 1 mg mL^{-1} in water), and multilayer graphene on copper foil (CVD 3-5 layer graphene on copper foil with one side etched) were purchased from ACS Material. Gold TEM grids (Quantifoil R1.2/1.3 100 × 400 mesh gold holey carbon) were purchased from SPI supplies. Single/double layer graphene on copper foil and graphene-coated copper mesh TEM grids (CVD graphene film deposited on ultrafine copper TEM grids, 2000 mesh) were purchased from Graphene Laboratories. Citrate-capped 10 nm spherical gold nanoparticles were purchased from BB International. Milli-Q water (18.2 MΩ·cm) was used in all the experiments.

SAXS characterization of BCC DNA-AuNP superlattices

SAXS data was collected using a Bruker Nanostar instrument (Bruker AXS). The X-ray source is a copper tube (λKα = 1.54 Å) chosen such that the scattering from gold is purely elastic. The beam was collimated by a pair of graded, cross-coupled Göbel mirrors which also serve as monochromators by Bragg interference through alternating layers of silicon and germanium. Further collimation by pinholes produces a spot size of 400 μm. Scattered photons were collected with a 2D gas-filled detector (Bruker HiStar) with a diameter of 11.5 cm. Inhomogeneities in the detector face were accounted for by performing flood field corrections with an Fe-55 isotope X-ray source. This source and a brass plate with a grid of pinholes were used to calculate spatial unwarping of the scattered photons projected on the relatively flat detector face. Finally, the sample-to-detector distance, beam center, and angular scale were calibrated by collecting scattering data from silver behenate. Dark current frames were subtracted from all data; scattering of the buffer, DNA, and capillary are considered negligible compared to the AuNP scattering in these data.

2D SAXS patterns were azimuthally averaged and relative scattering intensity is plotted as a function of scattering vector, q:

$$q = \frac{4\,\pi\,sin\theta}{\lambda}$$

where θ is the scattering angle and λ is the wavelength of X-ray radiation. Each scan is divided by the particle's form factor (the measured scattering pattern for particles that are completely dissociated) and compared against the modeled SAXS pattern (calculated using PowderCell) for an ideal BCC crystal structure. Interparticle spacing for BCC DNA-AuNP superlattices is calculated using the following equation:

$$d = \frac{\sqrt{6}\,\pi}{q_0}$$

Where q_0 is the position of the first scattering peak in 1/Å and d is the distance between the centroids of two nearest neighboring particles in nm.

TEM imaging

All TEM images and movies were obtained on a Tecnai G2 20 S-TWIN TEM equipped with a Gatan Orius SC200 CCD camera. The acceleration voltage was 200 kV and a LaB_6 filament was used. Electron dose rates used for imaging ranged from 10 to 250 $e^-/(Å^2 \cdot s)$, depending on the magnification (magnification values used were between 7 kx and 38 kx). Electron dose rate was calculated from the total pixel intensity using the conversion ratio of 10 counts in the CCD camera being equivalent to 1 electron. The frame rate used for video collection was 3.8 fps.

Chapter 4

Conclusions and Outlook

In Chapter 1, we introduced the fundamental concepts of self-assembly, the nature of nanoscale interactions between colloidal nanoparticles, DNA-mediated self-assembly, liquid phase TEM, and electron beam-induced effects. Sufficient detail was given to fully describe the relevant experimental setups and analytical methods that were used in our work. We also provided an assessment of the recent progress in the research field that allowed the novelty of our work included in this dissertation to be accurately evaluated within the context of previously reported studies in the literature.

In Chapter 2, we demonstrated a generalizable method for quantitative analysis of interparticle interactions at the nanoscale using trajectories of colloidal nanoparticles in solution. Through direct mapping of trajectories for a system of charged gold nanorods, we were able to apply statistical mechanics to construct a potential profile that describes their pairwise interaction. We confirmed the presence of the long-range electrostatic repulsion and showed that the assembly behavior of charged gold nanorods in solution was determined by the balance of long-range electrostatic repulsion and short-range van der Waals attraction. Equipped with this knowledge, we were able to tune the ionic strength to create conditions for non-assembly, selective tip-to-tip assembly, and non-specific assembly. Non-assembly was observed when the long-range electrostatic repulsion was strong enough such that the energetic barrier which must be overcome for rods to approach close enough to interact through van der Waals attraction was unsurmountable at the experimental timescale. Tip-selective assembly was observed when the ionic strength was such that the tip-to-tip approach of an incoming rod was allowed, leading to assembly through van der Waals attraction, while other configurations of approach were energetically prohibited. This was due to the inherent anisotropy in particle shape, which meant that the repulsion experienced by an incoming rod depended on the relative spatial configuration of the two interacting rods. Non-specific assembly occurred when the ionic strength was high enough to effectively screen the electrostatic repulsion between the nanorods, thus removing the orientational dependence of the interparticle interaction. We anticipate that our method of extracting nanoscale interactions by direct visualization of nanoparticle dynamics will be applicable to a wide range of systems with different particle shapes and interaction types.

In Chapter 3, we systematically investigated the role of graphene in mitigating the radiation-induced damage of the specimen through a set of carefully designed experiments involving different liquid cell configurations. Employing BCC DNA-AuNP superlattices as our model system, where the long-range ordered arrangement of AuNPs was an indicator for the structural stability of interparticle DNA linkages, we were able to carry out a direct comparative study of DNA stability under electron beam irradiation in both graphene and silicon nitride liquid cells. When exposed to similar electron dose rates, DNA-AuNP superlattices, which were stable when imaged using graphene liquid cells, underwent initial dissociation into individual AuNPs followed by their aggregation when imaged using silicon nitride liquid cells. Without any protection mechanisms in place, disruption of DNA-mediated ordering is expected since radiation damage in DNA causes DNA strand breaks. We then compared the extents of chemical and structural changes in

graphene when it was exposed to electron beam irradiation with and without the presence of water using correlative Raman spectroscopy and liquid phase TEM. We showed that graphene undergoes significantly greater changes when water is present at its surface, leading us to conclude that graphene is reacting with the products of water radiolysis. We deduced that the protective ability of graphene was due to its radical scavenging properties, rather than its thermal or electrical properties. Based on our findings, we demonstrated that the protective effect is still seen when graphene oxide sheets and graphene quantum dots, which can also act as radical scavengers, are incorporated into silicon nitride liquid cells. We illustrated the use of water-soluble graphene derivatives as biocompatible radical scavengers that could be utilized for imaging radiation-sensitive specimens with liquid phase TEM, which should open up future opportunities for studying the dynamics of biological specimens.

Our results presented in this dissertation exemplify our contribution to the ongoing endeavor to explore how the technique of liquid phase TEM may be used to study nanoscale systems where the observed dynamic processes are not dominated by the electron beam perturbation. Thus far, the majority of liquid phase TEM studies have focused on exploiting the known electron beam-induced effects to trigger dynamic processes that could be analyzed, but future studies that systematically investigate how we can predictably and controllably adjust the effects of the electron beam are warranted. For the conclusions drawn from liquid phase TEM experiments to be more impactful and relevant to researchers outside of the field, we must invest more effort into demonstrating that the experiments conducted inside the liquid cell under electron beam irradiation can be consistent with traditional wet lab experiments which are free from the influence of the electron beam.

References

(1) Whitesides, G. M.; Grzybowski, B. *Science* **2002**, *295*, 2418–2421.

(2) Boles, M. A.; Engel, M.; Talapin, D. V. *Chem. Rev.* **2016**, *116*, 11220–11289.

(3) Whitelam, S.; Feng, E. H.; Hagan, M. F.; Geissler, P. L. *Soft Matter* **2009**, *5*, 1251–1262.

(4) Whitelam, S. *Soft Matter* **2015**, *11*, 8225–8235.

(5) Whitelam, S.; Jack, R. L. *Annu. Rev. Phys. Chem.* **2015**, *66*, 143–163.

(6) Cademartiri, L.; Bishop, K. J. M. *Nat. Mater.* **2015**, *14*, 2–9.

(7) Bishop, K. J. M.; Wilmer, C. E.; Soh, S.; Grzybowski, B. A. *Small* **2009**, *5*, 1600–1630.

(8) Israelachvili, J. N. *Intermolecular and surface forces*, 3rd ed.; Academic Press: New York, 2011.

(9) Min, Y.; Akbulut, M.; Kristiansen, K.; Golan, Y.; Israelachvili, J. *Nat. Mater.* **2008**, *7*, 527–538.

(10) Walker, D. A.; Kowalczyk, B.; de la Cruz, M. O.; Grzybowski, B. A. *Nanoscale* **2011**, *3*, 1316–1344.

(11) French, R. H.; Parsegian, V. A.; Podgornik, R.; Rajter, R. F.; Jagota, A.; Luo, J.; Asthagiri, D.; Chaudhury, M. K.; Chiang, Y.; Granick, S.; Kalinin, S.; Kardar, M.; Kjellander, R.; Langreth, D. C.; Lewis, J.; Lustig, S.; Wesolowski, D.; Wettlaufer, J. S.; Ching, W.-Y.; Finnis, M.; Houlihan, F.; von Lilienfeld, O. A.; van Oss, C. J.; Zemb, T. *Rev. Mod. Phys.* **2010**, *82*, 1887–1944.

(12) Silvera Batista, C. A.; Larson, R. G.; Kotov, N. A. *Science* **2015**, *350*, 1242477.

(13) Vondermassen, K.; Bongers, J. J.; Mueller, A.; Versmold, H. *Langmuir* **1994**, *10*, 1351–1353.

(14) Crocker, J. C.; Grier, D. G. *Phys. Rev. Lett.* **1994**, *73*, 352–355.

(15) Royall, C. P.; Louis, A. A.; Tanaka, H. *J. Chem. Phys.* **2007**, *127*, 44507.

(16) Crocker, J. C.; Grier, D. G. *J. Colloid Interface Sci.* **1996**, *310*, 298–310.

(17) Grier, D. G. *Nature* **2003**, *424*, 810–816.

(18) Madivala, B.; Fransaer, J.; Vermant, J. *Langmuir* **2009**, *25*, 2718–2728.

(19) Zhao, K.; Bruinsma, R.; Mason, T. G. *Proc. Natl. Acad. Sci. U. S. A.* **2011**, *108*, 2684–2687.

(20) Glotzer, S. C.; Solomon, M. J.; Kotov, N. A. *AIChE J.* **2004**, *50*, 2978–2985.

(21) Seeman, N. C. *J. Theor. Biol.* **1982**, *99*, 237–247.

(22) Li, X.; Yang, X.; Qi, J.; Seeman, N. C. *J. Am. Chem. Soc.* **1996**, *118*, 6131–6140.

(23) Rothemund, P. W. K. *Nature* **2006**, *440*, 297–302.

(24) Ke, Y.; Ong, L. L.; Sun, W.; Song, J.; Dong, M.; Shih, W. M.; Yin, P. *Nat. Chem.* **2014**, *6*, 994–1002.

(25) Alivisatos, A. P.; Johnsson, K. P.; Peng, X.; Wilson, T. E.; Loweth, C. J.; Bruchez, M. P.; Schultz, P. G. *Nature* **1996**, *382*, 609–611.

(26) Mirkin, C. A.; Letsinger, R. L.; Mucic, R. C.; Storhoff, J. J. *Nature* **1996**, *382*, 607–609.

(27) Park, S. Y.; Lytton-Jean, A. K. R.; Lee, B.; Weigand, S.; Schatz, G. C.; Mirkin, C. A. *Nature* **2008**, *451*, 553–556.

(28) Nykypanchuk, D.; Maye, M. M.; van der Lelie, D.; Gang, O. *Nature* **2008**, *451*, 549–552.

(29) Macfarlane, R. J.; Lee, B.; Jones, M. R.; Harris, N.; Schatz, G. C.; Mirkin, C. A. *Science* **2011**, *334*, 204–208.

(30) Jones, M. R.; Seeman, N. C.; Mirkin, C. A. *Science* **2015**, *347*, 1260901.

(31) Macfarlane, R. J.; Jones, M. R.; Lee, B.; Auyeung, E.; Mirkin, C. A. *Science* **2013**, *341*, 1222–1225.

(32) Zhang, C.; Macfarlane, R. J.; Young, K. L.; Choi, C. H. J.; Hao, L.; Auyeung, E.; Liu, G.; Zhou, X.; Mirkin, C. A. *Nat. Mater.* **2013**, *12*, 741–746.

(33) Jones, M. R.; Macfarlane, R. J.; Lee, B.; Zhang, J.; Young, K. L.; Senesi, A. J.; Mirkin, C. A. *Nat. Mater.* **2010**, *9*, 913–917.

(34) O'Brien, M. N.; Girard, M.; Lin, H.-X.; Millan, J. A.; Olvera de la Cruz, M.; Lee, B.; Mirkin, C. A. *Proc. Natl. Acad. Sci. U. S. A.* **2016**, *113*, 10485–10490.

(35) Jones, M. R.; Kohlstedt, K. L.; O'Brien, M. N.; Wu, J.; Schatz, G. C.; Mirkin, C. A. *Nano Lett.* **2017**, *17*, 5830–5835.

(36) O'Brien, M. N.; Jones, M. R.; Lee, B.; Mirkin, C. A. *Nat. Mater.* **2015**, *14*, 833–839.

(37) Macfarlane, R. J.; Lee, B.; Hill, H. D.; Senesi, A. J.; Seifert, S.; Mirkin, C. A. *Proc. Natl. Acad. Sci. U. S. A.* **2009**, *106*, 10493–10498.

(38) Zhang, Y.; Pal, S.; Srinivasan, B.; Vo, T.; Kumar, S.; Gang, O. *Nat. Mater.* **2015**, *14*, 840–847.

(39) Kim, Y.; Macfarlane, R. J.; Jones, M. R.; Mirkin, C. A. *Science* **2016**, *351*, 579–582.

(40) Knoll, M.; Ruska, E. *Z. Phys.* **1932**, *78*, 318–339.

(41) Williamson, M. J.; Tromp, R. M.; Vereecken, P. M.; Hull, R.; Ross, F. M. *Nat. Mater.* **2003**, *2*, 532–536.

(42) Ross, F. M. *Science* **2015**, *350*, aaa9886.

(43) Fu, X.; Chen, B.; Tang, J.; Hassan, M. T.; Zewail, A. H. *Science* **2017**, *355*, 494–498.

(44) Yuk, J. M.; Park, J.; Ercius, P.; Kim, K.; Hellebusch, D. J.; Crommie, M. F.; Lee, J. Y.; Zettl, A.; Alivisatos, A. P. *Science* **2012**, *336*, 61–64.

(45) Zheng, H.; Claridge, S. A.; Minor, A. M.; Alivisatos, A. P.; Dahmen, U. *Nano Lett.* **2009**, *9*, 2460–2465.

(46) Verch, A.; Pfaff, M.; de Jonge, N. *Langmuir* **2015**, *31*, 6956–6964.

(47) Woehl, T. J.; Prozorov, T. *J. Phys. Chem. C* **2015**, *119*, 21261–21269.

(48) Chee, S. W.; Baraissov, Z.; Loh, N. D.; Matsudaira, P. T.; Mirsaidov, U. *J. Phys. Chem. C* **2016**, *120*, 20462–20470.

(49) Girit, C. O.; Meyer, J. C.; Erni, R.; Rossell, M. D.; Kisielowski, C.; Yang, L.; Park, C.-H.; Crommie, M. F.; Cohen, M. L.; Louie, S. G.; Zettl, A. *Science* **2009**, *323*, 1705–1708.

(50) Warner, J. H.; Rümmeli, M. H.; Ge, L.; Gemming, T.; Montanari, B.; Harrison, N. M.; Büchner, B.; Briggs, G. A. D. *Nat. Nanotechnol.* **2009**, *4*, 500–504.

(51) Yuk, J. M.; Jeong, M.; Kim, S. Y.; Seo, H. K.; Kim, J.; Lee, J. Y. *Chem. Commun.* **2013**, *49*, 11479.

(52) Egerton, R. F.; Li, P.; Malac, M. *Micron* **2004**, *35*, 399–409.

(53) Cazaux, J. *Ultramicroscopy* **1995**, *60*, 411–425.

(54) Garrett, B. C.; Dixon, D. A.; Camaioni, D. M.; Chipman, D. M.; Johnson, M. A.; Jonah, C. D.; Kimmel, G. A.; Miller, J. H.; Rescigno, T. N.; Rossky, P. J.; Xantheas, S. S.; Colson, S. D.; Laufer, A. H.; Ray, D.; Barbara, P. F.; Bartels, D. M.; Becker, K. H.; Bowen, K. H.; Bradforth, S. E.; Carmichael, I.; Coe, J. V; Corrales, L. R.; Cowin, J. P.; Dupuis, M.; Eisenthal, K. B.; Franz, J. A.; Gutowski, M. S.; Jordan, K. D.; Kay, B. D.; LaVerne, J. A.; Lymar, S. V; Madey, T. E.; McCurdy, C. W.; Meisel, D.; Mukamel, S.; Nilsson, A. R.; Orlando, T. M.; Petrik, N. G.; Pimblott, S. M.; Rustad, J. R.; Schenter, G. K.; Singer, S. J.; Tokmakoff, A.; Wang, L.-S.; Zwier, T. S. *Chem. Rev.* **2005**, *105*, 355–390.

(55) Le Caër, S. *Water* **2011**, *3*, 235–253.

(56) Schneider, N. M.; Norton, M. M.; Mendel, B. J.; Grogan, J. M.; Ross, F. M.; Bau, H. H. *J. Phys. Chem. C* **2014**, *118*, 22373–22382.

(57) Grogan, J. M.; Schneider, N. M.; Ross, F. M.; Bau, H. H. *Nano Lett.* **2014**, *14*, 359–364.

(58) de Jonge, N.; Ross, F. M. *Nat. Nanotechnol.* **2011**, *6*, 695–704.

(59) White, E. R.; Mecklenburg, M.; Shevitski, B.; Singer, S. B.; Regan, B. C. *Langmuir* **2012**, *28*, 3695–3698.

(60) Grogan, J. M.; Rotkina, L.; Bau, H. H. *Phys. Rev. E* **2011**, *83*, 61405.

(61) Liu, Y.; Lin, X.-M.; Sun, Y.; Rajh, T. *J. Am. Chem. Soc.* **2013**, *135*, 3764–3767.

(62) Zhu, G.; Jiang, Y.; Huang, W.; Zhang, H.; Lin, F.; Jin, C. *Chem. Commun.* **2013**, *49*, 10944–10946.

(63) de Jonge, N.; Peckys, D. B.; Kremers, G. J.; Piston, D. W. *Proc. Natl. Acad. Sci. U. S. A.* **2009**, *106*, 2159–2164.

(64) Kraus, T.; de Jonge, N. *Langmuir* **2013**, *29*, 8427–8432.

(65) Sun, M.; Liao, H.-G.; Niu, K.; Zheng, H. *Sci. Rep.* **2013**, *3*, 3227.

(66) Zheng, H.; Smith, R. K.; Jun, Y.-W.; Kisielowski, C.; Dahmen, U.; Alivisatos, A. P. *Science* **2009**, *324*, 1309–1312.

(67) Woehl, T. J.; Evans, J. E.; Arslan, I.; Ristenpart, W. D.; Browning, N. D. *ACS Nano* **2012**, *6*, 8599–8610.

(68) Nielsen, M. H.; Aloni, S.; De Yoreo, J. J. *Science* **2014**, *345*, 1158–1162.

(69) Liao, H.-G.; Zherebetskyy, D.; Xin, H.; Czarnik, C.; Ercius, P.; Elmlund, H.; Pan, M.; Wang, L.-W.; Zheng, H. *Science* **2014**, *345*, 916–919.

(70) Park, J. H.; Schneider, N. M.; Grogan, J. M.; Reuter, M. C.; Bau, H. H.; Kodambaka, S.; Ross, F. M. *Nano Lett.* **2015**, *15*, 5314–5320.

(71) Ahmad, N.; Wang, G.; Nelayah, J.; Ricolleau, C.; Alloyeau, D. *Nano Lett.* **2017**, *17*, 4194–4201.

(72) Woehl, T. J.; Abellan, P. *J. Microsc.* **2017**, *265*, 135–147.

(73) Milligan, J. R.; Aguilera, J. A.; Wu, C. C.; Paglinawan, R. A.; Nguyen, T.-T. D.; Wu, D.; Ward, J. F. *Radiat. Res.* **1997**, *148*, 325–329.

(74) Slivka, A.; Cohen, G. *J. Biol. Chem.* **1985**, *260*, 15466–15472.

(75) Yen, G.-C.; Hsieh, C.-L. *Biosci., Biotechnol., Biochem.* **1997**, *61*, 1646–1649.

(76) Liu, X.; Cao, J.; Li, H.; Li, J.; Jin, Q.; Ren, K.; Ji, J. *ACS Nano* **2013**, *7*, 9384–9395.

(77) Ye, X.; Jones, M. R.; Frechette, L. B.; Chen, Q.; Powers, A. S.; Ercius, P.; Dunn, G.; Rotskoff, G. M.; Nguyen, S. C.; Adiga, V. P.; Zettl, A.; Rabani, E.; Geissler, P. L.; Alivisatos, A. P. *Science* **2016**, *354*, 874–877.

(78) Knowles, T. P. J.; Vendruscolo, M.; Dobson, C. M. *Nat. Rev. Mol. Cell Biol.* **2014**, *15*, 384–396.

(79) Adamcik, J.; Jung, J.-M.; Flakowski, J.; De Los Rios, P.; Dietler, G.; Mezzenga, R. *Nat. Nanotechnol.* **2010**, *5*, 423–428.

(80) Prasad, B. V. V. *Science* **1999**, *286*, 287–290.

(81) van den Berg, B.; Clemons, W. M.; Collinson, I.; Modis, Y.; Hartmann, E.; Harrison, S. C.; Rapoport, T. A. *Nature* **2004**, *427*, 36–44.

(82) Sönnichsen, C.; Reinhard, B. M.; Liphardt, J.; Alivisatos, A. P. *Nat. Biotechnol.* **2005**, *23*, 741–745.

(83) Tao, A.; Sinsermsuksakul, P.; Yang, P. *Nat. Nanotechnol.* **2007**, *2*, 435–440.

(84) Fan, J. A.; Wu, C.; Bao, K.; Bao, J.; Bardhan, R.; Halas, N. J.; Manoharan, V. N.; Nordlander, P.; Shvets, G.; Capasso, F. *Science* **2010**, *328*, 1135–1138.

(85) Ye, X.; Chen, J.; Diroll, B. T.; Murray, C. B. *Nano Lett.* **2013**, *13*, 1291–1297.

(86) Young, K. L.; Ross, M. B.; Blaber, M. G.; Rycenga, M.; Jones, M. R.; Zhang, C.; Senesi, A. J.; Lee, B.; Schatz, G. C.; Mirkin, C. A. *Adv. Mater.* **2014**, *26*, 653–659.

(87) Hentschel, M.; Saliba, M.; Vogelgesang, R.; Giessen, H.; Alivisatos, A. P.; Liu, N. *Nano Lett.* **2010**, *10*, 2721–2726.

(88) Huynh, W. U. *Science* **2002**, *295*, 2425–2427.

(89) Talapin, D. V. *Science* **2005**, *310*, 86–89.

(90) Talapin, D. V; Lee, J.-S.; Kovalenko, M. V; Shevchenko, E. V. *Chem. Rev.* **2010**, *110*, 389–458.

(91) Yamada, Y.; Tsung, C.-K.; Huang, W.; Huo, Z.; Habas, S. E.; Soejima, T.; Aliaga, C. E.; Somorjai, G. A.; Yang, P. *Nat. Chem.* **2011**, *3*, 372–376.

(92) Zhang, Q.; Shu, X. Z.; Lucas, J. M.; Toste, F. D.; Somorjai, G. A.; Alivisatos, A. P. *Nano Lett.* **2014**, *14*, 379–383.

(93) Karplus, M.; McCammon, J. A. *Nat. Struct. Biol.* **2002**, *9*, 646–652.

(94) Baker, N. A.; Sept, D.; Joseph, S.; Holst, M. J.; McCammon, J. A. *Proc. Natl. Acad. Sci. U. S. A.* **2001**, *98*, 10037–10041.

(95) Elber, R. *Curr. Opin. Struct. Biol.* **2005**, *15*, 151–156.

(96) Agarwal, U.; Escobedo, F. A. *Nat. Mater.* **2011**, *10*, 230–235.

(97) Henzie, J.; Grünwald, M.; Widmer-Cooper, A.; Geissler, P. L.; Yang, P. *Nat. Mater.* **2011**, *11*, 131–137.

(98) Ye, X.; Chen, J.; Engel, M.; Millan, J. A.; Li, W.; Qi, L.; Xing, G.; Collins, J. E.; Kagan, C. R.; Li, J.; Glotzer, S. C.; Murray, C. B. *Nat. Chem.* **2013**, *5*, 466–473.

(99) Damasceno, P. F.; Engel, M.; Glotzer, S. C. *Science* **2012**, *337*, 453–457.

(100) Jiang, Y.; Zhu, G.; Lin, F.; Zhang, H.; Jin, C.; Yuan, J.; Yang, D.; Zhang, Z. *Nano Lett.* **2014**, *14*, 3761–3765.

(101) Sutter, E.; Jungjohann, K.; Bliznakov, S.; Courty, A.; Maisonhaute, E.; Tenney, S.; Sutter, P. *Nat. Commun.* **2014**, *5*, 4946.

(102) Park, J.; Zheng, H.; Lee, W. C.; Geissler, P. L.; Rabani, E.; Alivisatos, A. P. *ACS Nano* **2012**, *6*, 2078–2085.

(103) Liao, H.-G.; Cui, L.; Whitelam, S.; Zheng, H. *Science* **2012**, *336*, 1011–1014.

(104) Chen, Q.; Smith, J. M.; Park, J.; Kim, K.; Ho, D.; Rasool, H. I.; Zettl, A.; Alivisatos, A. P. *Nano Lett.* **2013**, *13*, 4556–4561.

(105) Nie, Z.; Fava, D.; Kumacheva, E.; Zou, S.; Walker, G. C.; Rubinstein, M. *Nat. Mater.* **2007**, *6*, 609–614.

(106) Thomas, K. G.; Barazzouk, S.; Ipe, B. I.; Joseph, S. T. S.; Kamat, P. V. *J. Phys. Chem. B* **2004**, *108*, 13066–13068.

(107) Sönnichsen, C.; Alivisatos, A. P. *Nano Lett.* **2005**, *5*, 301–304.

(108) Huang, X.; El-Sayed, I. H.; Qian, W.; El-Sayed, M. A. *J. Am. Chem. Soc.* **2006**, *128*, 2115–2120.

(109) Liu, N.; Hentschel, M.; Weiss, T.; Alivisatos, A. P.; Giessen, H. *Science* **2011**, *332*, 1407–1410.

(110) Biswas, S.; Duan, J.; Nepal, D.; Pachter, R.; Vaia, R. *Nano Lett.* **2013**, *13*, 2220–2225.

(111) Nikoobakht, B.; El-Sayed, M. *Chem. Mater.* **2003**, *15*, 1957–1962.

(112) Ye, X.; Gao, Y.; Chen, J.; Reifsnyder, D. C.; Zheng, C.; Murray, C. B. *Nano Lett.* **2013**, *13*, 2163–2171.

(113) Meakin, P. *Phys. Rev. Lett.* **1983**, *51*, 1119–1122.

(114) Vigderman, L.; Khanal, B. P.; Zubarev, E. R. *Adv. Mater.* **2012**, *24*, 4811–4841.

(115) Nikoobakht, B.; El-Sayed, M. A. *Langmuir* **2001**, *17*, 6368–6374.

(116) Murphy, C. J.; Sau, T. K.; Gole, A. M.; Orendorff, C. J.; Gao, J.; Gou, L.; Hunyadi, S. E.; Li, T. *J. Phys. Chem. B* **2005**, *109*, 13857–13870.

(117) Burrows, N. D.; Lin, W.; Hinman, J. G.; Dennison, J. M.; Vartanian, A. M.; Abadeer, N. S.; Grzincic, E. M.; Jacob, L. M.; Li, J.; Murphy, C. J. *Langmuir* **2016**, *32*, 9905–9921.

(118) Derjaguin, B.; Landau, L. *Prog. Surf. Sci.* **1993**, *43*, 30–59.

(119) Onsager, L. *Ann. N. Y. Acad. Sci.* **1949**, *51*, 627–659.

(120) Bates, M. A.; Frenkel, D. *J. Chem. Phys.* **2000**, *112*, 10034–10041.

(121) Donev, A.; Burton, J.; Stillinger, F. H.; Torquato, S. *Phys. Rev. B: Condens. Matter Mater. Phys.* **2006**, *73*, 1–11.

(122) Zheng, H.; Zhu, Y. *Ultramicroscopy* **2017**, *180*, 188–196.

(123) Peckys, D. B.; de Jonge, N. *Nano Lett.* **2011**, *11*, 1733–1738.

(124) Pohlmann, E. S.; Patel, K.; Guo, S.; Dukes, M. J.; Sheng, Z.; Kelly, D. F. *Nano Lett.* **2015**, *15*, 2329–2335.

(125) Hermannsdörfer, J.; Tinnemann, V.; Peckys, D. B.; de Jonge, N. *Microsc. Microanal.* **2016**, *22*, 656–665.

(126) Mirsaidov, U. M.; Zheng, H.; Casana, Y.; Matsudaira, P. *Biophys. J.* **2012**, *102*, L15-7.

(127) Peckys, D. B.; de Jonge, N. *Microsc. Microanal.* **2014**, *20*, 1–20.

(128) Woehl, T. J.; Kashyap, S.; Firlar, E.; Perez-Gonzalez, T.; Faivre, D.; Trubitsyn, D.; Bazylinski, D. A.; Prozorov, T. *Sci. Rep.* **2014**, *4*, 6854.

(129) von Sonntag, C. *Free-Radical-Induced DNA Damage and Its Repair*; Springer: Berlin, 2006.

(130) Hutchinson, F. *Prog. Nucleic Acid Res. Mol. Biol.* **1985**, *32*, 115–154.

(131) Breen, A. P.; Murphy, J. A. *Free Radical Biol. Med.* **1995**, *18*, 1033–1077.

(132) Balasubramanian, B.; Pogozelski, W. K.; Tullius, T. D. *Proc. Natl. Acad. Sci. U. S. A.* **1998**, *95*, 9738–9743.

(133) Burrows, C. J.; Muller, J. G. *Chem. Rev.* **1998**, *98*, 1109–1152.

(134) Ward, J. F. *Prog. Nucleic Acid Res. Mol. Biol.* **1988**, *35*, 95–125.

(135) Pogozelski, W. K.; Tullius, T. D. *Chem. Rev.* **1998**, *98*, 1089–1108.

(136) Mohanty, N.; Fahrenholtz, M.; Nagaraja, A.; Boyle, D.; Berry, V. *Nano Lett.* **2011**, *11*, 1270–1275.

(137) Chen, Q.; Smith, J. M.; Rasool, H. I.; Zettl, A.; Alivisatos, A. P. *Faraday Discuss.* **2014**, *175*, 203–214.

(138) Wang, C.; Qiao, Q.; Shokuhfar, T.; Klie, R. F. *Adv. Mater.* **2014**, *26*, 3410–3414.

(139) Park, J.; Park, H.; Ercius, P.; Pegoraro, A. F.; Xu, C.; Kim, J. W.; Han, S. H.; Weitz, D. A. *Nano Lett.* **2015**, *15*, 4737–4744.

(140) Nair, R. R.; Blake, P.; Blake, J. R.; Zan, R.; Anissimova, S.; Bangert, U.; Golovanov, A. P.; Morozov, S. V.; Geim, A. K.; Novoselov, K. S.; Latychevskaia, T. *Appl. Phys. Lett.* **2010**, *97*, 153102.

(141) Zan, R.; Ramasse, Q. M.; Jalil, R.; Georgiou, T.; Bangert, U.; Novoselov, K. S. *ACS Nano* **2013**, *7*, 10167–10174.

(142) Algara-Siller, G.; Kurasch, S.; Sedighi, M.; Lehtinen, O.; Kaiser, U. *Appl. Phys. Lett.* **2013**, *103*, 7–12.

(143) Cutler, J. I.; Auyeung, E.; Mirkin, C. A. *J. Am. Chem. Soc.* **2012**, *134*, 1376–1391.

(144) Kewalramani, S.; Guerrero-García, G. I.; Moreau, L. M.; Zwanikken, J. W.; Mirkin, C. A.; de la Cruz, M. O.; Bedzyk, M. J. *ACS Cent. Sci.* **2016**, *2*, 219–224.

(145) Jones, M. R.; Macfarlane, R. J.; Prigodich, A. E.; Patel, P. C.; Mirkin, C. A. *J. Am. Chem. Soc.* **2011**, *133*, 18865–18869.

(146) Senesi, A. J.; Eichelsdoerfer, D. J.; Brown, K. A.; Lee, B.; Auyeung, E.; Choi, C. H. J.; Macfarlane, R. J.; Young, K. L.; Mirkin, C. A. *Adv. Mater.* **2014**, *26*, 7235–7240.

(147) Auyeung, E.; Li, T. I. N. G.; Senesi, A. J.; Schmucker, A. L.; Pals, B. C.; de la Cruz, M. O.; Mirkin, C. A. *Nature* **2014**, *505*, 73–77.

(148) Fultz, B.; Howe, J. M. *Transmission Electron Microscopy and Diffractometry of Materials*, 3rd ed.; Springer: Berlin, 2007.

(149) Radha, B.; Senesi, A. J.; O'Brien, M. N.; Wang, M. X.; Auyeung, E.; Lee, B.; Mirkin, C. A. *Nano Lett.* **2014**, *14*, 2162–2167.

(150) Auyeung, E.; MacFarlane, R. J.; Choi, C. H. J.; Cutler, J. I.; Mirkin, C. A. *Adv. Mater.* **2012**, *24*, 5181–5186.

(151) Liu, W.; Tagawa, M.; Xin, H. L.; Wang, T.; Emamy, H.; Li, H.; Yager, K. G.; Starr, F. W.; Tkachenko, A. V.; Gang, O. *Science* **2016**, *351*, 582–586.

(152) Noll, D. M.; Mason, T. M.; Miller, P. S. *Chem. Rev.* **2006**, *106*, 277–301.

(153) Deans, A. J.; West, S. C. *Nat. Rev. Cancer* **2011**, *11*, 467–480.

(154) Dukes, M. J.; Jacobs, B. W.; Morgan, D. G.; Hegde, H.; Kelly, D. F. *Chem. Commun.* **2013**, *49*, 3007–3009.

(155) Zhang, H.; Wang, D. *Angew. Chem., Int. Ed.* **2008**, *47*, 3984–3987.

(156) Reina, A.; Son, H.; Jiao, L.; Fan, B.; Dresselhaus, M. S.; Liu, Z.; Kong, J. *J. Phys. Chem. C* **2008**, *112*, 17741–17744.

(157) Li, X.; Cai, W.; An, J.; Kim, S.; Nah, J.; Yang, D.; Piner, R.; Velamakanni, A.; Jung, I.; Tutuc, E.; Banerjee, S. K.; Colombo, L.; Ruoff, R. S. *Science* **2009**, *324*, 1312–1314.

(158) Liang, X.; Sperling, B. A.; Calizo, I.; Cheng, G.; Hacker, C. A.; Zhang, Q.; Obeng, Y.; Yan, K.; Peng, H.; Li, Q.; Zhu, X.; Yuan, H.; Walker, A. R. H.; Liu, Z.; Peng, L. M.; Richter, C. A. *ACS Nano* **2011**, *5*, 9144–9153.

(159) Barin, G. B.; Song, Y.; Gimenez, I. D.; Souza Filho, A. G.; Barreto, L. S.; Kong, J. *Carbon* **2015**, *84*, 82–90.

(160) Ferrari, A. C.; Meyer, J. C.; Scardaci, V.; Casiraghi, C.; Lazzeri, M.; Mauri, F.; Piscanec, S.; Jiang, D.; Novoselov, K. S.; Roth, S.; Geim, A. K. *Phys. Rev. Lett.* **2006**, *97*, 187401.

(161) Tang, L.; Wang, Y.; Li, J. *Chem. Soc. Rev.* **2015**, *44*, 6954–6980.

(162) Regan, W.; Alem, N.; Alemán, B.; Geng, B.; Girit, Ç.; Maserati, L.; Wang, F.; Crommie, M.; Zettl, A. *Appl. Phys. Lett.* **2010**, *96*, 113102.

(163) Lin, W.-H.; Chen, T.-H.; Chang, J.-K.; Taur, J.-I.; Lo, Y.-Y.; Lee, W.-L.; Chang, C.-S.; Su, W.-B.; Wu, C.-I. *ACS Nano* **2014**, *8*, 1784–1791.

(164) Wang, D.-Y.; Huang, I.-S.; Ho, P.-H.; Li, S.-S.; Yeh, Y.-C.; Wang, D.-W.; Chen, W.-L.; Lee, Y.-Y.; Chang, Y.-M.; Chen, C.-C.; Liang, C.-T.; Chen, C.-W. *Adv. Mater.* **2013**, *25*, 4521–4526.

(165) Yuk, J. M.; Zhou, Q.; Chang, J.; Ercius, P.; Alivisatos, A. P.; Zettl, A. *ACS Nano* **2016**, *10*, 88–92.

(166) Ferrari, A. C.; Basko, D. M. *Nat. Nanotechnol.* **2013**, *8*, 235–246.

(167) Ferrari, A. C. *Solid State Commun.* **2007**, *143*, 47–57.

(168) Woehl, T. J.; Jungjohann, K. L.; Evans, J. E.; Arslan, I.; Ristenpart, W. D.; Browning, N. D. *Ultramicroscopy* **2013**, *127*, 53–63.

(169) Chen, Q.; Cho, H.; Manthiram, K.; Yoshida, M.; Ye, X.; Alivisatos, A. P. *ACS Cent. Sci.* **2015**, *1*, 33–39.

(170) Qiu, Y.; Wang, Z.; Owens, A. C. E.; Kulaots, I.; Chen, Y.; Kane, A. B.; Hurt, R. H. *Nanoscale* **2014**, *6*, 11744–11755.

(171) Radich, J. G.; Kamat, P. V. *ACS Nano* **2013**, *7*, 5546–5557.

(172) Yu, C.; Zhang, B.; Yan, F.; Zhao, J.; Li, J.; Li, L.; Li, J. *Carbon* **2016**, *105*, 291–296.

(173) Chong, Y.; Ge, C.; Fang, G.; Tian, X.; Ma, X.; Wen, T.; Wamer, W. G.; Chen, C.; Chai, Z.; Yin, J. J. *ACS Nano* **2016**, *10*, 8690–8699.

(174) Ward, J. F.; Blakely, W. F.; Joner, E. I. *Radiat. Res.* **1985**, *103*, 383–392.

(175) Siddiqi, M. A.; Bothe, E. *Radiat. Res.* **1987**, *112*, 449–463.

(176) Krisch, R. E.; Flick, M. B.; Trumbore, C. N. *Radiat. Res.* **1991**, *126*, 251–259.

(177) Lim, S. Y.; Shen, W.; Gao, Z. *Chem. Soc. Rev.* **2015**, *44*, 362–381.

(178) Loh, K. P.; Bao, Q.; Eda, G.; Chhowalla, M. *Nat. Chem.* **2010**, *2*, 1015–1024.

Appendix

A1. Tip-selectivity of charged gold rod assembly

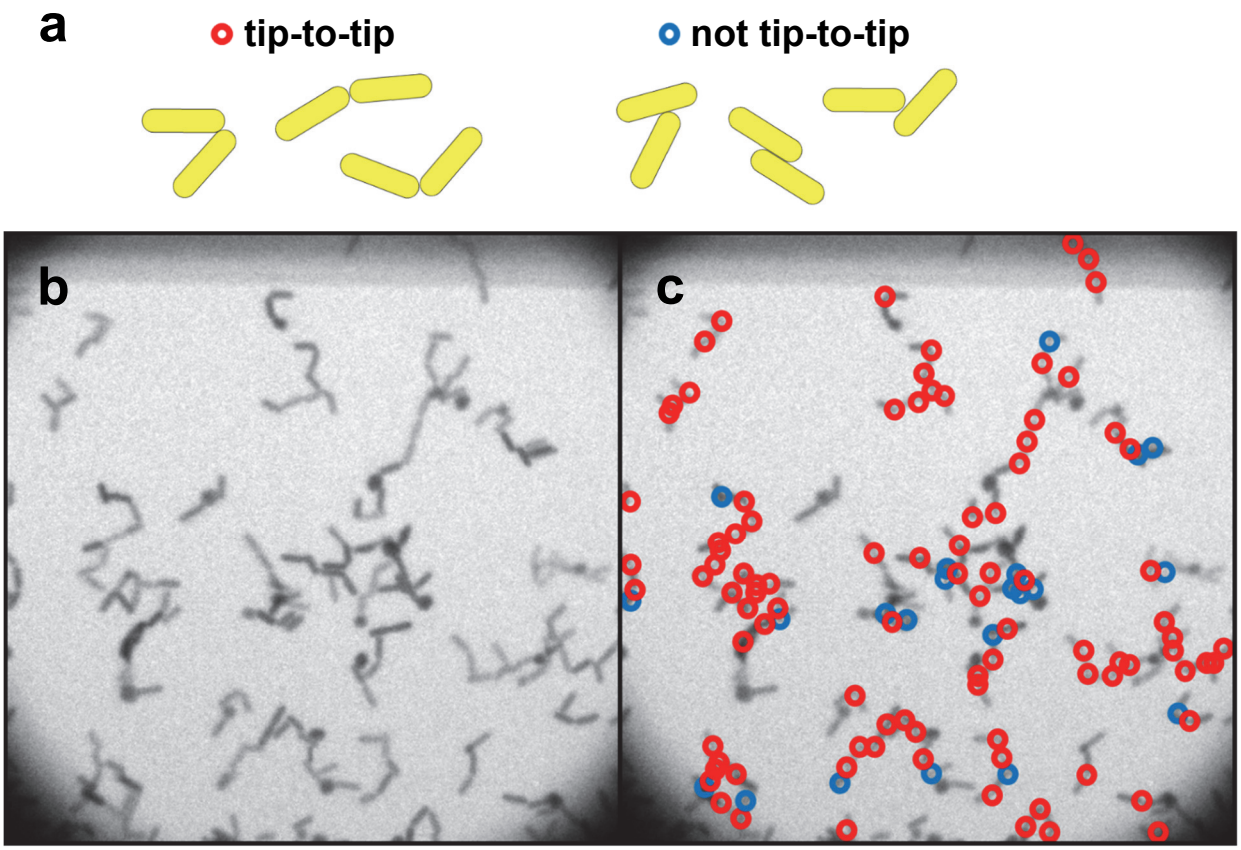

Figure A1 Fraction of tip-to-tip assembled gold nanorods. (a) Schematic illustration of how tip-to-tip attachment was defined. In this study, it was defined as attachment between regions of curvature at rod tips and anything else was defined as not tip-to-tip. (b) TEM image showing a large scale view of assembled rods. (c) TEM image in (b) overlaid with red (tip-to-tip) and blue (not tip-to-tip) circles to indicate the fraction of tip-to-tip attachments. In this particular image shown, 94 are tip-to-tip (81 %) and 22 are not tip-to-tip (19 %). When this analysis was extended for 610 rod-to-rod attachments, 80 % were tip-to-tip. Note that attachments to spheres have been ignored.

A2. Modeling nanoparticle arrangements in different BCC lattice planes

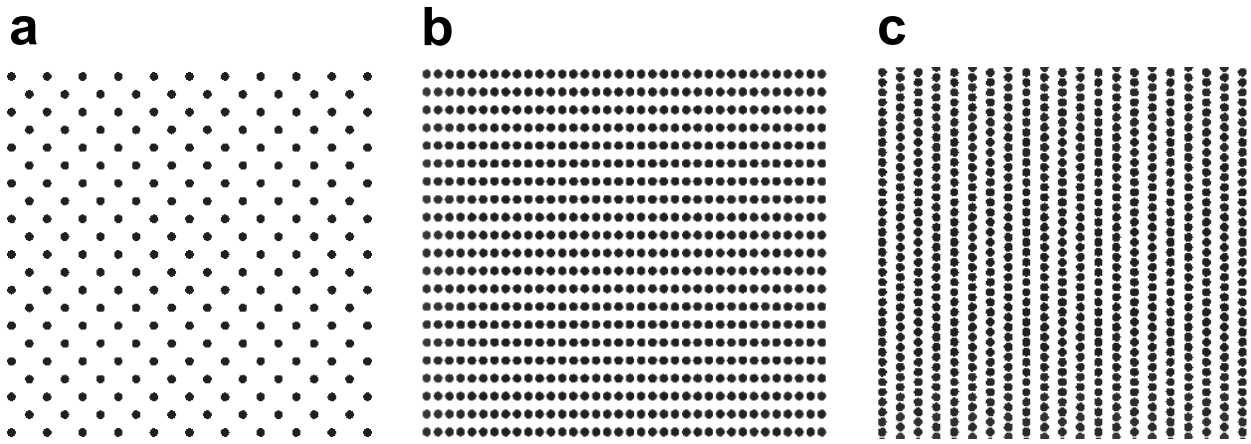

Figure A2 Different arrangements of nanoparticles in a BCC structure when viewed along different directions. (a) Viewed along [001]. (b) Viewed along [0-13]. (c) Viewed along [320]. Qualitative comparison with the experimentally observed BCC arrangement of nanoparticles shown in Figures 3.2b and 3.2c confirmed that the zone axis is either [0-13] or [320].

A3. Simulated FFT images of nanoparticles in different BCC lattice planes

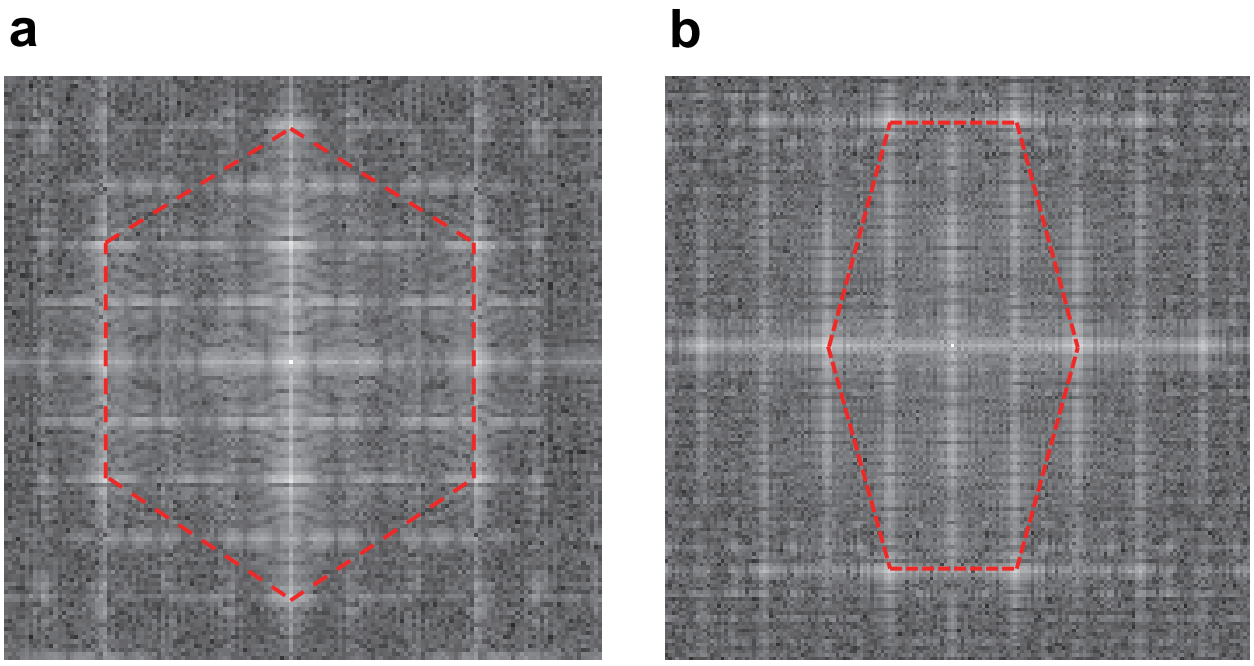

Figure A3 FFT images generated for a BCC arrangement of nanoparticles viewed along different directions. (a) FFT image generated for vectors (200) and (131) viewed along [0-13]. Overlaid with red dotted lines that indicate the regular hexagonal arrangement of diffraction peaks. (b) FFT image generated for vectors (200) and (123) viewed along [320]. Overlaid with red dotted lines that indicate the elongated hexagonal arrangement of diffraction peaks. Qualitative comparison with the experimentally obtained FFT image shown in the inset of Figure 3.2b confirmed that the diffraction pattern corresponds to that of a BCC crystal with the [320] zone axis

A4. Optical microscopy of delaminated multilayer graphene

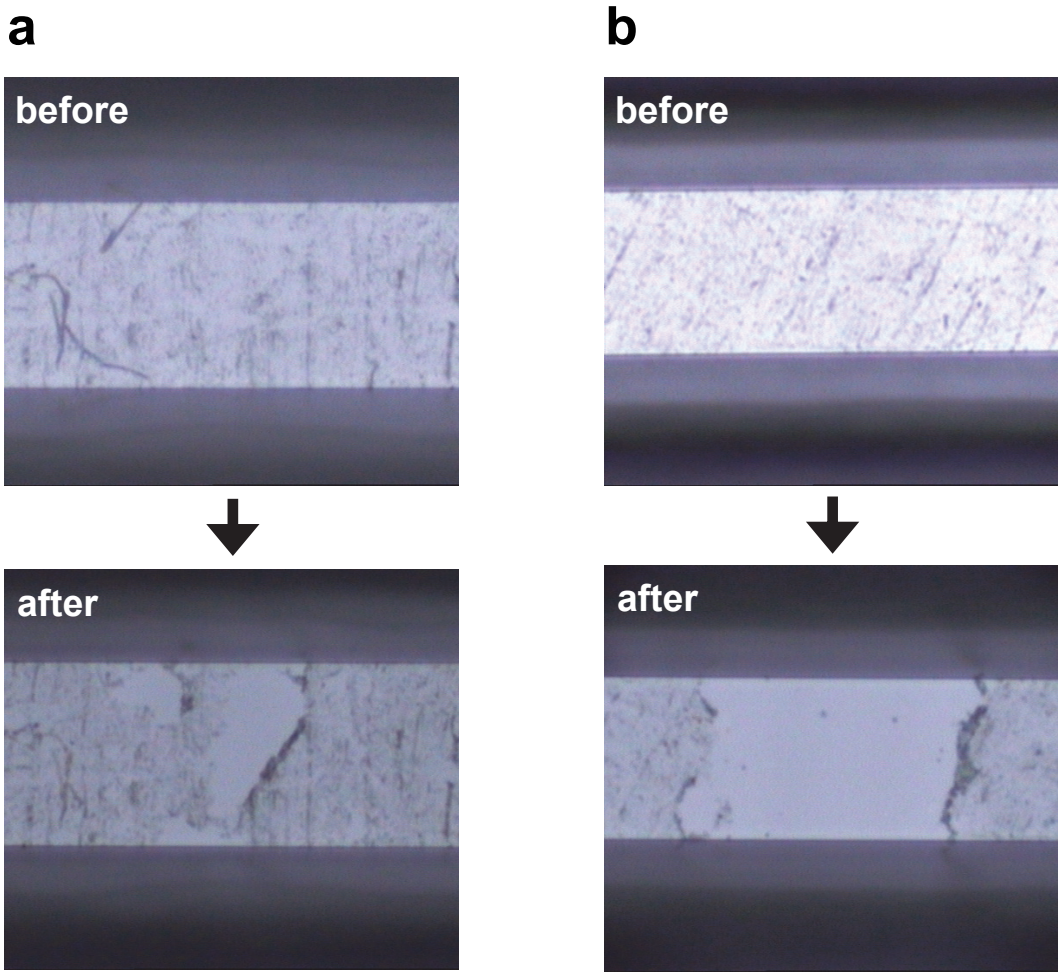

Figure A4 Delamination of multilayered graphene as a result of electron beam irradiation in water. (a) Before and after TEM imaging in water at a lower electron dose rate. Significant delamination was seen in the exposed area. (b) Before and after TEM imaging in water at a higher electron dose rate. The exposed area has almost fully delaminated. Note that delamination of graphene was not observed when it was irradiated without the presence of water at the dose rates used.